Turbulence and Transport of Passive Scalar in Magnetohydrodynamic Channel Flow

by

Prasanta Kumar Dey

A dissertation submitted in partial fulfillment
of the requirements for the degree of
Doctor of Philosophy
(Automotive Systems Engineering)
in the University of Michigan-Dearborn
2018

Doctoral Committee:

Professor Oleg Zikanov, Chair
Associate Professor Dewey Dohoy Jung
Professor Ghassan Kridli
Professor Ben Q. Li

ACKNOWLEDGEMENTS

I would like to express my sincere gratitude to my advisor Prof. Oleg Zikanov for his invaluable guidance and support in my doctoral research and scientific education. I would like to thank him for his patience, encouragements and mentorship over the years in pursuing and completing the dissertation.

I would also like to thank the doctoral committee for their feedback and support in completing the dissertation.

My sincere thanks also for my lab mates Xuan Zhang, Zhao Yurong and others for their endless supports and encouragements.

I am indebted to my wife Rongita Roy for her continued mental support, patience and encouragements in completing my doctoral research. Special thanks to my son Pramit Dey for his encouragements.

Thanks for the financial supports from US NSF (Grant CBET 096557).

TABLE OF CONTENTS

LIST OF FIGURES

Figure

LIST OF TABLES

Table

ABSTRACT

An imposed magnetic field influences the flow structure and transport characteristics of a moving electrically conducting fluid. Such magnetohydrodynamic (MHD) flows are ubiquitous in nature and technological applications, for example in casting of steel and aluminum and growth of semiconductor crystals. In many situations, the effect of the magnetic field is combined with that of mean shear and occurs in the presence of transport of heat and admixtures. In the performed doctoral research, extensive Direct Numerical Simulations (DNS) are conducted for the flows of an electrically conducting fluid in a channel with imposed magnetic field. The cases of wall-normal, spanwise and streamwise orientations of the magnetic field are considered. The strength of the magnetic field varies in such a way that the flow transitions from fully turbulent state to slightly below the laminarization threshold. The main goal of the investigation is to understand the flow transformation and the effect of the magnetic field on the characteristics of the transport of a passive scalar (e.g. temperature or admixture). It is found how the magnetic field affects the scalar distribution and the rate the turbulent transport across the channel. In the range of the magnetic field strengths considered, the effect is strong in the cases of the wall-normal and spanwise magnetic field, but weaker in the case of the streamwise field. A major outcome of the study is the establishment of a nearly linear dependency of the turbulent scalar flux of the magnetic interaction parameter (the Stuart number). One-dimensional models, of flow field and scalar distribution with approximations of eddy diffusivity and eddy viscosity are developed on the basis of the computational results. Scalar transport and perturbation dynamics are also investigated for the channel flow with spanwise magnetic field for the flow regime characterized by the large-scale intermittency characterized by long periods of nearly laminar, nearly two-dimensional behavior interrupted by brief turbulent bursts.

Keywords Magnetohydrodynamics, Turbulent Transport, Passive Scalar

CHAPTER I

INTRODUCTION

1.1 Influence of magnetic field on electrically conducting fluid

Magnetohydrodynamics (MHD) is the theory of the macroscopic interaction between magnetic fields and the flow of electrically conducting non-magnetic fluids, which can be observed in nature as well as in industrial processes [1]. MHD is relevant for a wide range of physical disciplines, which include astro- and geo-physical fluid dynamics, laboratory and industrial applications, as well as the plasma confinement. The broad spectrum of MHD applications is based on the coupling between flow field and magnetic field which can be more or less strong. For the case of weak coupling, one of the two fields acts upon the other without being significantly affecting itself. One such example is industrial or laboratory scale flows, where magnetic field is only weakly affected by the flow of conducting fluid, while seriously modifying the structure and transport characteristics of the flow. In the case of strong coupling between the two fields, both field differs sharply from what they would be, either in electromagnetism or in fluid mechanics [2]. One such example is the dynamo effect or the expulsion of the magnetic field in geophysical and astrophysical context which explains the mechanism of magnetic field generation by a celestial body such as earth or star.

In MHD, the basic principles of the interaction combine the principles of the classical fluid mechanics and electrodynamics. The interactions of a magnetic field, **B** and a velocity field **u** can be explained in three steps as follow [1]:

a. The relative movement of conducting fluid and a magnetic field causes an e.m.f. (of the order of ($|\mathbf{u}\times\mathbf{B}|$) to develop as per Faraday's law of induction. In general, the electrical currents will ensue, the current density being of order $\sigma(\mathbf{u}\times\mathbf{B})$, where σ is

the electrical conductivity. The induced currents produce a second, induced magnetic field, **b**, following the Ampere's law. The total magnetic field is thus includes the original magnetic field plus the induced magnetic field. The change in flow structure is usually such that the fluid appears to 'drag' the magnetic field lines along with it.

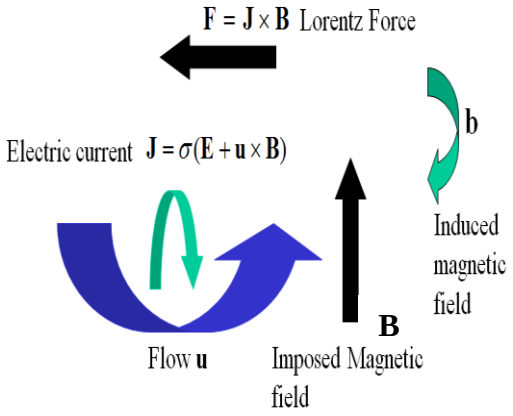

Figure 1.1: Influence of magnetic field on electrically conducting non-magnetic fluid

b. The total magnetic field interacts with the induced current density **j** which give rise to a Lorentz force per unit volume **j** × **B**. This acts to inhibit the relative movement of the magnetic field and the fluid.

Each unit volume of liquid having **j** and **B** experiences Lorentz Force which may lead to pressure drop, turbulence modifications and change in heat and mass transfer and other important MHD phenomena.

The interaction results in influencing the relative movement of fluid and field. The magnetic field affects the flow in two different ways. First, the additional suppression of turbulence is caused by the induced currents via Joule dissipation. Second, the flow acquires anisotropy of gradients.

The magnetic fields behave according to the conductivity of the medium. In resemblance with the hydrodynamic Reynolds number (Re) the magnetic Reynolds number is one of the key important dimensionless parameters in MHD which is a measure of relative strength of the induced magnetic field (**b**) in comparison with the imposed or original magnetic field (**B**). It is defined as follow:

$$R_m = \frac{UL}{\lambda} \quad , \tag{1.1}$$

where U and L are the characteristic velocity and length scales in the flow and λ is the magnetic diffusivity of the fluid given by $\lambda = (\mu_0 \sigma)^{-1}$, μ_0 and σ being the magnetic permeability of free space and the electrical conductivity of the fluid respectively.

For low-Rm (R_m<<1) case, the medium is generally a poor conductor, the induced magnetic field in fluid motion is negligible by comparison with the imposed field. The interaction is dissipative in nature rather than elastic and the damping of mechanical motion is caused by converting the kinetic energy into heat via Joule dissipation. The current study focuses on low-Rm flow of MHD which involves the industrial and laboratory scale flows (e.g. liquid metal) rather than on high-Rm flow (R_m) which covers geophysical or astrophysical MHD.

The advection is relatively unimportant for low-R_m case and so the magnetic field will tend to relax towards a purely diffusive state which is determined by the boundary conditions rather than flow. The distinctive feature of low-Rm flow (R_m<<1) is the nearly one-way coupling between magnetic field and the flow. The diffusive cut-off length-scale of the magnetic field is sufficiently large in such cases, so that the magnetic field can be resolved in numerical simulations. The task of modeling turbulence and scalar transport at smaller scales reduces to the problem of low-R_m turbulent transport which is addressed in this dissertation.

1.2 MHD applications

As explained in section 1.2, the MHD application areas can be classified in terms of the range of Magnetic Reynolds Number (R_m). Figure 1.2 shows some application areas of MHD in terms of R_m range.

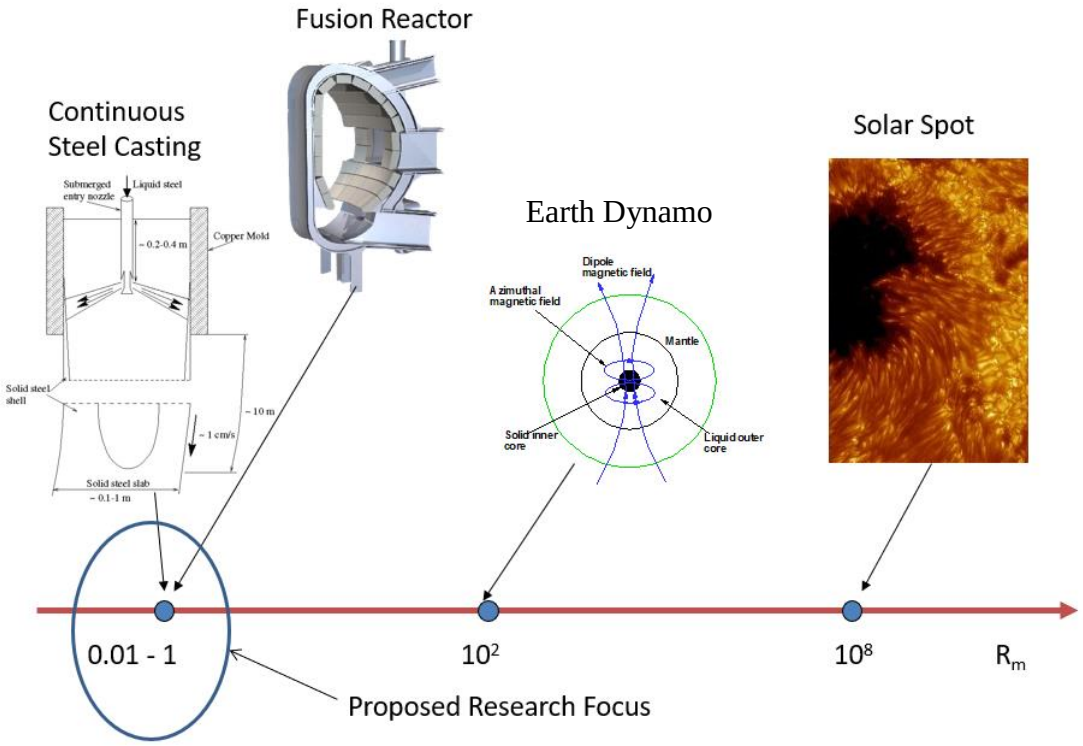

Figure 1.2: MHD application in terms of Magnetic Reynolds Number, R_m scale

The fact that magnetic field can be successfully utilized to heat, stir or levitate fluid, or to control transport characteristics, produces a range of technological applications. In general, MHD applications can be subdivided into two areas. In one area, there are technical devices whose working principal is based on MHD effects, e.g. MHD pumps, MHD generator, plasma confinement in fusion reactors [3]. The second area involves industrial production processes which may be optimized or controlled using MHD effects, e.g. transport control

by MHD in fusion blankets, continuous steel casting, crystal growth devices, levitation melting etc.

Industrial or engineering applications of MHD began late by around the 1960s. It started due to the need to pump liquid Sodium that was used as a coolant in fast breeder reactors and to enable confining plasma which was necessary to perform controlled thermonuclear fusion for power generation. Subsequently, in 1970s, many traditional processes related to metal casting were revisited and were modified/replaced in ways that involved utilizing magnetic fields to improve process efficiency and product quality [4]. Continuous casting of steel also started during the same time. As a result, pumping of liquid metal using electromagnetic pumps, stirring of molten metal using rotating magnetic fields during the casting process to obtain better and homogenous ingots, damping of molten metal flow using static magnetic fields to prevent surface contamination occurring due to entrainment, and magnetic levitation to melt highly reactive metals like Titanium, have become some of the common processes in the metallurgical industry that take advantage of magnetohydrodynamic phenomena. Controlled silicon crystal growth using magnetic fields [5] and non-intrusive flow measurement techniques are a few more applications of recent interest. Currently, the engineering applications of MHD are myriad and it is possible to mention only a few important ones here for reasons of brevity.

1.2.1 Electromagnetic Braking in Continuous Steel Casting

A process of particular interest relevant to the scopes of the current study is the continuous casting of steel. Steel is widely used engineering material with strong prevalence in automotive industries in automotive body structure. Steelmaking is a sophisticated high tech process in which technological advancement plays a crucial role. Several challenges are encountered in production of high quality steel due to the flow fluctuations in molten steel as follow:

- Porosity: Oxidation process introduces entrapment of hot gases in liquid steel which must be released during cooling process to avoid the problem of porosity in steel. Effective mixing is required to encounter the problem.
- Grain Structure: Flow fluctuation in liquid steel prevents it become desired fine-grained structure due to the formation of separate crystals with boundaries.
- Slag: Slag forms as a layer of oxidized impurities on top of liquid steel which can reduce material properties if remains in metal. It must be kept separate from metal.

The above-mentioned challenges during casting process significantly affect the quality of the product. In the process of steel casting, liquid steel is continuously supplied to a water cooled copper mold through a submerged inlet pipe. Recirculation is created in the mold due to the strong momentum of injected liquid steel which induces entrapment of particles and impurities. Another potentially drawback feature of the process is the impingement of feeding jets into the solidifying shell, which can produce a 'hot spot', shell erosion or even breakdown. Both problems can be alleviated by actively controlling the flow of the molten steel using the so-called EMBR (Electro-Magnetic BRaking) device [2]. An intense (0.1 to 0.5 T) static magnetic field is imposed to suppress the turbulent feeding jet and to damp turbulent eddies. The primary effect of the magnetic field is to brake the mean flow; the motion of the fluid through the magnetic field induces Lorentz forces, which tend to counteract the motion perpendicular to the magnetic field. Another effect is magnetic dissipation of turbulence, or joule dissipation, which reduces the turbulent transport of heat and momentum. Figure 1.3 shows the effect of a localized magnetic field on the mean flow in the mold [6]. The momentum of inlet jet is reduced and redirected. The penetration depth of the jet is thus considerably reduced, as is the entrapment of oxide particles and gas bubbles. The meniscus, i.e. the near-wall interface between liquid steel and the slag layer, will be calmer and the surface temperature higher. Because of the increased stability, the process often leads to a substantial reduction of cracks in the surface of the product.

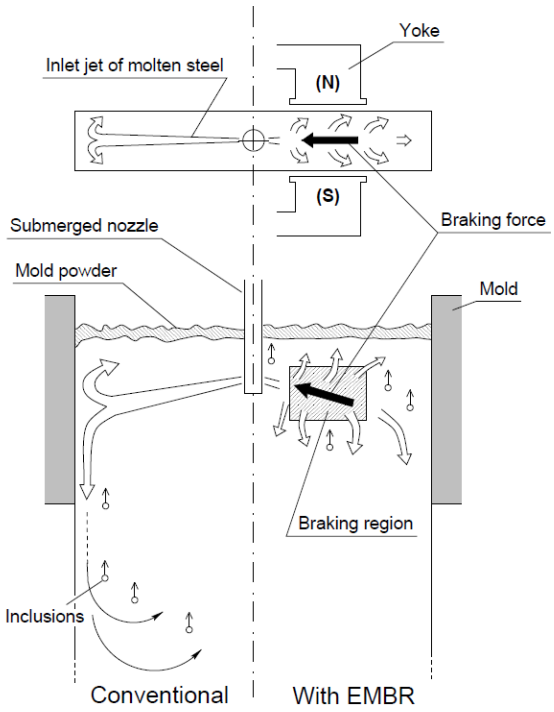

Figure 1.3: Outline of flow field and transport of inclusions in continuous slab casting. Left side of the figure is showing conventional casting without magnetic braking and right side is showing an electromagnetic brake (EMBR) has been applied to brake the momentum of the inlet jet [6]

Experimental investigations on continuous steel casting and EMBR are difficult to perform due to the existence of harsh operating conditions and shear limitations in measurement techniques. Numerical flow simulation is used by the manufacturer of the magnetic brake for casting process optimization in regard to the performance specifications [7, 8, 9]. In simulating turbulent flows, the main approach used as to solve equations for mean velocities, mean temperatures etc. The effects of the turbulent fluctuations on the mean flow are accounted by considering model equations for statistical quantities. Common quantities used in turbulence models are the kinetic energy of the turbulence and quantities related to length scale and time scales or time scales of the largest turbulent eddies which are main features for most of the turbulent transport. Commercial numerical flow solvers can be extended to include the effect of the magnetic field on the mean flow but the effect of the magnetic field on turbulence is very difficult to incorporate [6]. In general,

conventional turbulence model cannot capture the turbulence structures elongated in the direction of the magnetic field which are very important for a correct description of Joule dissipation of turbulence.

1.2.2 Crystal growth by Czochralsky Method

Another example of low-Rm MHD application is the growth of large silicon crystals by Czochralsky method, where magnetic fields are used to achieve better quality of the crystal growth through suppression of undesired fluctuations of temperature and admixture concentration and establishing favorable temperature gradient near the solidification surface. The electromagnetic control is considered critical for the current industry transition to larger (d~300-400 mm) crystals [10].

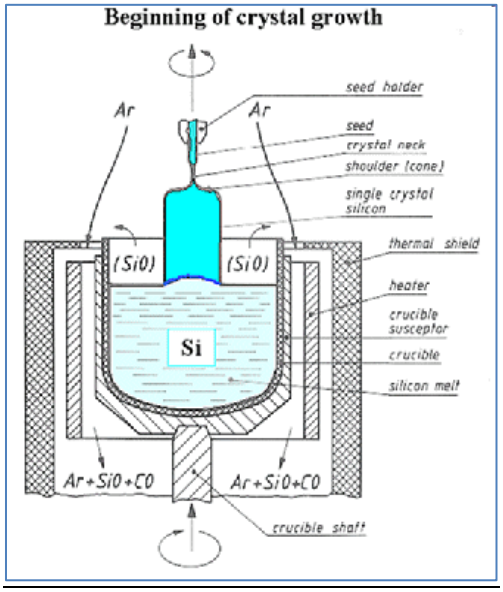

Figure 1.4: Crystal growth [10]

1.2.3 Fusion enabling technology

Liquid metal (Li or Li, Pb) cooling and breeding blankets for future nuclear fusion reactors have applications for the principle of low-Rm MHD flow.

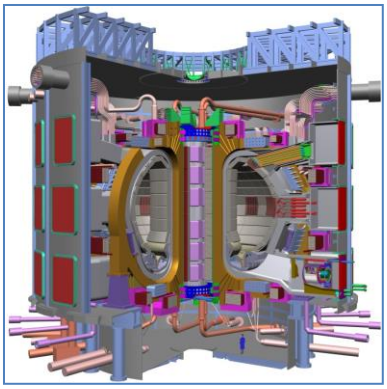

Figure 1.5: Fusion reactor (www.iter.org)

Strong magnetic fields generated in the reactor penetrates blanket and dramatically change the flow structure creating yet unsolved problems of sharp increase of the flow resistance, suppression of turbulence and associated reduction of heat and admixture transport.

1.3 Importance of fundamental understandings of low-Rm MHD

In all technological applications, magnetic field directly affect the rate of energy consumption and environmental impact. Considering the production volume and the rate played by these technologies in the economy, the ultimate effect of even small technological improvements is difficult to overestimate. For example, in steel casting, the magnetic field control leads to more reliable quality of the product and consequently, reduce the impact on environmental and energy consumptions through by avoiding extra grinding, oxidizing or treating operations. In the Aluminum production, better understanding and accurate modeling of the melt flows and interface instability have been identified as a high priority task face by the industry [11]. The potential benefits achievable through redesigning existing cell lines and optimizing new designs include nationwide annual energy savings up to 20TWh and strong reduction or even complete elimination of emission of PFC (perfluorocarbon) gases, currently at the level of 10Tg Eq (teragram equivalent) per year. As a result, solving the problem of reducing flow resistance and enhancing heat and admixture transport in breeding blankets is recognized as the key to the energy efficiency of the future fusion reactors.

Some of the discussed technologies in section 1.2, for example, EMBR or Hall-Heroult electrolysis are well established. The others, such as the use of magnetic fields in crystal growth, are in the stage of development and early applications, while yet others such as the fusion reactor blankets are currently non-existent. The role of magnetic field and the resultant flow field interactions in all the technological applications are far from being fully understood. A case of example is EMBR which has been in mass production for more than two decades. EMBR devices are prone to undesirable effects upon installation. Sometimes, the imposed magnetic field increases the heat transfer toward the mold wall and enhances the hot spot effect instead of suppressing it.

1.4 Background and Motivation for the doctoral work

Since the inception in 1930, the liquid metal MHD has been studied in different aspects and perspectives. However, understanding of MHD flows is far from complete and generally, lays significantly behind the understanding achieved in classical non-magnetic hydrodynamics. The scarcity of reliable experimental data attributed to the non-transparent liquids such as liquid metal or oxide melts in which practical flow field observation is impossible to achieve. Recent advancement in measurement techniques, such as ultrasound velocimetry, inductive tomography etc. made some improvement in experimental findings. However, significant challenges remain to comprehend the understanding of flow physics, transport phenomena and application specific ambiguities on how an imposed magnetic field influences the flow of an electrically conducting fluid.

The broad topic of the current study is the effects of the magnetic field on turbulence and passive scalar transport in channel. Such wall-bounded flows are nearly ubiquitous in technological MHD, and therefore, are of practical importance. Technological MHD flows are found in a transitional laminar-to-turbulent case or magnetic field suppresses turbulence and instabilities. Even though the Reynolds number is typically large, a magnetic field can lead to laminarization or to transformation into a weakly turbulent state. The effect of the magnetic field on transport of scalars (admixture concentrations or heat) is critical for many technological applications. In some of them, such as continuous casting or crystal growth,

the magnetic field is applied intentionally to control the transport, while in others, most prominently in blankets for fusion reactors, the suppressive effect of the magnetic field is undesirable and must be rectified. The configuration of a channel flow in a uniform transverse magnetic field chosen for the present study represents the quintessence of MHD flows. At the same time, the configuration is sufficiently simple and well-defined to be appropriate for a study of the fundamental features of the flow-field interactions.

1.4.1 Basic features of wall-bounded MHD flows

The basic principles of interaction between the imposed magnetic field and the flow are relatively well understood in wall-bounded flow [1-3, 12-14]. Far from walls, the main effect is two-fold. In first instance, the induced electric currents result in Joule dissipation, which serves as an additional mechanism of conversation of kinetic energy of the flow into heat; i.e. of flow suppression. Secondly, the flow becomes anisotropic. The magnetic field tends to eliminate velocity gradients and elongate flow structures in the direction of the magnetic field lines. In the limit of strong field, the flow approaches two-dimensional form with all variables uniform in the direction of the magnetic field. The anisotropy leads to suppression of nonlinear energy transfer to small length scales. A sufficiently strong magnetic field can laminerize the flow. It can be stressed out that only anisotropy of gradients is directly created by the magnetic field. Non-uniformity of amplitudes of velocity components (anisotropy of the Reynold stress tensor) is often generated in MHD flows, but indirectly and in the form that strongly depends on the nature of the flow.

1.4.2 Large Scale Intermittency

The intermittency phenomena is a unique flow regime in MHD which was discovered for forced homogenous turbulence in [13] and later found in an ideal flow within tri-axial ellipsoid [14] and a channel flow in a spanwise magnetic field [15]. In a range of intermediate values of magnetic interaction parameter which is a measure of magnetic field strength, the flows develop global intermittency, in which periods of slow nearly two-dimensional and nearly laminar evolution of alternate with three-dimensional turbulent

bursts. The mechanism which leads to intermittency is explained in detail in the literature review section (section 5.1) of Chapter 5. The intermittency is universal in nature in realistic MHD flow, for example in a steel casting mold or as a small-scale feature of turbulent dynamo. In the current study, the intermittency is explored in broad scopes of energy spectrum and integral transport characteristics since such intermittent flow can affect the homogeneity of the end product of engineering scale flow greatly as it alters between different energy states and structures. The results of the current study on intermittency are presented in Chapter 5.

1.4.3 Duct flow as an archetypal MHD flow

A rectangular duct in the presence of a transverse magnetic field is an archetypal case of liquid metal MHD. In this role, the place occupied by the duct flow in MHD is much more prominent than the place of its non-magnetic counterpart in hydrodynamics. In fact, the pioneering study of the duct flow [16] is considered by many a starting point of the discipline. Importance of the MHD duct flow stems from the fact that, albeit simple, the configuration incorporates the main features of technological liquid metal flows: magnetic suppression and anisotropy, strong mean shear and characteristics MHD boundary layers. At a sufficiently strong magnetic field, the flow develops flat core. The mean shear and thus, potential for instability and turbulence are limited to the boundary layers. They develop as a result of interaction between the driving force (pressure gradient), viscous or turbulent momentum transfer, and the Lorentz force. The latter is defined by the distribution of electric currents, which, in turn, is determined by the flow and electric properties of the walls and the liquid.

Two types of MHD boundary layers are recognized [3, 17]. The Hartmann layers appears at the walls perpendicular to the magnetic field and have thickness $\delta \sim L/Ha$, where L is the duct width along the magnetic field. This has profound consequences for flows with high values of magnetic field strength, for example, in fusion reactor blankets. Strong shear within the Hartmann layers results in drag resistance and renders the designs concepts with large lithium flow rate highly problematic. The sidewall layers develop at the walls parallel

to the magnetic field. Their thickness is $\sim L/Ha^{1/2}$. The flow structure within the sidewall layers varies with wall conductance. In many cases, for example when all four walls are perfectly conducting and perfectly insulating, the profile follows usual boundary layer pattern, with velocity monotonously decreasing from the value of the core flow to zero. There are special cases, in particular, a duct with conducting Hartmann walls and insulating sidewalls, in which the sidewall layers are characterized by jet-like behavior and carry a large part of the flow rate [3, 17].

1.4.4 Numerical Simulation of MHD Flows in channel

In the current work, influence of imposed magnetic field on channel geometry is studied with respect to turbulence and passive scalar transport. A comprehensive literature review is done with regards to the scope of the current work. In Chapter 3, 4, 5 and 6, the reviews are presented in detail. In this section, a brief overview of the prior works is highlighted.

The first paper which is written by Hartmann [18] about the influence of imposed magnetic field in wall-normal direction of a channel, presents analytical solution of laminar flow. It is shown for the first time that a sufficiently strong magnetic field profoundly changes the velocity field [19]. DNS of flow in a channel to study the effect of magnetic field orientation on the pressure drop is conducted by Lee and Choi [20]. Magnetic field orientations of sreamwise, wall-normal and span-wise directions are considered in the study. Increased drag in wall-normal direction of magnetic field is found due to the Hartmann effect. Large Eddy Simulation (LES) in a channel flow under a wall normal magnetic field is performed by Kobayashi [21]. Results with a Coherent Structure Smagorinsky Model (CSM) are compared with those using the Smagorinsky Model (SM) and Dynamic Smagorinsky Model (DSM). Satake, Kunugi, Kazuyuki and Yasuo [22] presents Direct Numerical Simulation (DNS) results of the effect of magnetic field on wall bounded turbulence in a channel at a high Reynolds Number of 45818 and Hartmann numbers (Dimensionless Number presenting strength of the magnetic field defined in Chapter 2) of 32.5 and 65. A uniform magnetic field is applied normal to the wall and various turbulence quantities were analyzed. Large scale structures are found to decrease

in the core of the channel. Therefore, the difference between production and dissipation in the turbulent kinetic energy are found to decrease upon increase of Hartmann number in the central region of the channel. Boeck et al [23] performs DNS studies of the effect of the wall normal magnetic field on a turbulent flow in a channel at different Reynolds and Hartmann numbers. The three-layer near wall structure consisting of viscous region, logarithmic layer and plateau are reported at higher Hartmann numbers. These structures are reported signifying the importance of viscous, turbulent and electromagnetic stresses on the streamwise momentum equation. The turbulent stresses were found decaying more rapidly away from the wall than predicted by mixing-length models. Noguchi and Kasagi [24] also conducts the DNS in MHD channel flow under transverse magnetic field at Re_τ =150 and Ha=6.

Krasnov et al. [25] performs DNS and LES in a channel flow under span-wise magnetic field at two Reynolds numbers (10,000 and 20,000) and Hartmann numbers varying over a wide range. The main effect of the magnetic field is observed in turbulence suppression and reduction in the momentum transfer in the wall normal direction. The centerline velocity increases while the mean velocity gradient close to wall reduces and thus reducing the drag. The coherent structures are found to be enlarged in the horizontal direction upon increasing the Hartmann number. From comparison of LES with the DNS, the dynamic Smagorinsky model is found to reproduce the changes in the flow more accurately.

Yamamoto et al. [26] performs DNS on fully developed turbulent channel flow with imposed magnetic field on wall-normal direction. High and low Prandtl number conditions (Pr = 5.25 and 0.025, respectively) are evaluated. MHD effect on heat transfer degradation is found to be larger for high magnetic interaction parameter ranges. A new correlation is suggested for the MHD heat transfer in case of high Prandtl number fluid (Pr =5.25).

1.5 Objectives

The focus of the current doctoral research is on transport of a passive scalar (temperature or concentration of an admixture) in low magnetic Reynolds number (R_m) flow in channels. Since low-R_m and low-Pr_m (Prandtl Number) magnetohydrodynamic flow forms

the basis of important industrial technological applications (e.g. continuous steel casting, crystal growth), fundamental understandings of transport characteristics are of great importance to produce successful application.

Different orientations of an imposed magnetic field with varying magnetic field strength configurations are considered for the flow of an electrically conducting fluid and resultant scalar transport which have never been analyzed before. Through the analysis with high-resolution numerical simulations, following pressing questions are attempted to be addressed:

- *What is the effect of imposed magnetic field on turbulent scalar-transport in Channel flow?*

  -The question includes multiple questions related to the specific effect produced by the magnetic field, namely suppression or enhancement of transport, development of coherent structure, combined effect of magnetic field and mean shear, etc. In addressing the questions, the scalar field introduced via imposed mean gradients at various orientations of magnetic field is considered. The objective is to identify and understand the main features of the MHD flow transformation affecting the scalar transport.

- *How does the large-scale intermittency between 2D laminar and 3D turbulent regime affect the passive scalar transport?*

- Large scale intermittency is a regime observed in flows of electrically conducting fluids (i.e. liquid metal) in the presence of the imposed magnetic field. It is characterized by flow experiencing long periods of nearly laminar, nearly two-dimensional flow interrupted by violent three-dimensional bursts [15]. The proposed doctoral study aims to investigate the intermittency phenomena in the case of a channel flow with span-wise magnetic field. The study also focuses on transport

properties of the flow, distribution of the perturbation energy between mean flow and fluctuations and the effect of the strength of the magnetic field.

- *1D modeling of Eddy viscosity and diffusivity for Magnetohydrodynamic Channel flow*.

  -For a fully developed 1D MHD flow with an imposed magnetic field in wall-normal direction, the current study develops correlation for eddy viscosity and diffusivity based on the direct numerical simulation (DNS) results.

1.6 Outline of the Thesis

In the next chapter, formulation of the problem and numerical models representing the doctoral study have been discussed. The MHD equations in non-dimensional forms with non-relativistic MHD approximation and scalar transport equation have been presented for different orientations of the magnetic field. The boundary conditions, numerical scheme and solver methodologies are discussed.

In Chapters III and IV, the results for the turbulent flow structure and scalar transport with different orientation of the magnetic fields are presented. In Chapter V, the intermittency phenomenon for the case of a channel flow with span-wise magnetic field and the related scalar transport characteristics are discussed. Finally, in Chapter VI, approximate 1D models for eddy viscosity and eddy diffusivity for fully developed flow are presented.

CHAPTER II

GOVERNING EQUATIONS AND MODELS

2.1 Physical Models

2.1.1 Basic Laws

The mathematical equations describing Magnetohydrodynamic (MHD) flows combine conventional hydrodynamic equations with electrodynamic equations. The system of equation is comprised of conservation of mass, conservation of linear momentum i.e. Navier-Stokes equations with additional Lorentz force term and Maxwell's equations describing the electro-magnetic effects.

The flow of an incompressible electrically conducting fluid (e.g. liquid metal) subjected to an imposed uniform constant magnetic field $\boldsymbol{B}$ in a channel is considered. The conservation of mass is represented by (2.1), where $\boldsymbol{u}$ is the velocity field. In the conservation of momentum (2.2), $\boldsymbol{P}$ is the pressure field, $\boldsymbol{F_L}$ is the Lorentz force, ρ and υ are the density and kinematic viscosity of the liquid metal respectively.

$$\text{Conservation of mass} \qquad \nabla.\boldsymbol{u} = \boldsymbol{0} \tag{2.1}$$

$$\text{Conservation of Momentum} \quad \frac{\partial \boldsymbol{u}}{\partial t} + (\boldsymbol{u}.\nabla)\boldsymbol{u} = -\frac{\boldsymbol{1}}{\boldsymbol{\rho}}\nabla \boldsymbol{P} + \upsilon \nabla^{\boldsymbol{2}}\boldsymbol{u} + \boldsymbol{F_L} \tag{2.2}$$

The transport of a passive (not affecting the flow) scalar (temperature or concentration of an admixture) is also considered. The transport equation of passive scalar is expressed by (2.3) where θ is the passive scalar, χ is diffusivity of scalar, which is υ/Pr for temperature and υ/Sc (Pr is Prandtl number of the fluid, υ kinematic viscosity and Sc is Schmidt Number) for mass transport.

Passive scalar transport equation $$\frac{\partial \theta}{\partial t} + \boldsymbol{u}.\nabla\theta = \chi\nabla^2\theta \quad (2.3)$$

The Maxwell's equations describing the electromagnetic effects are:

Gauss's Law $$\nabla.\boldsymbol{E} = \frac{\rho_e}{\epsilon_0} \quad (2.4)$$

Solenoidal nature of magnetic field $$\nabla.\boldsymbol{B} = 0 \quad (2.5)$$

Faraday's law in differential form $$\nabla \times \boldsymbol{E} = -\frac{\partial B}{\partial t} \quad (2.6)$$

Ampere-Maxwell equation $$\nabla \times \boldsymbol{B} = \mu_0 \boldsymbol{J} + \mu_0\epsilon_0\frac{\partial E}{\partial t} \quad (2.7)$$

In the above-mentioned equations, ϵ_0 is the electric constant (also called the permittivity of free space), μ_0 is the magnetic constant (also called the permeability of free space), σ is the electrical conductivity, treated here as a constant, ρ_e is the charge density, $\boldsymbol{J}$ is the electric current density, $\boldsymbol{E}$ and $\boldsymbol{B}$ are the electric and magnetic fields. The MHD electrodynamic equations are simplified from the Maxwell's equations (2.4)-(2.7), charge conservation (2.8), Ohm's law (2.9) and Lorentz force (2.10)

Charge conservation $$\nabla.\boldsymbol{J} = -\frac{\partial \rho_e}{\partial t} \quad (2.8)$$

Ohm's law $$\boldsymbol{J} = \sigma(\boldsymbol{E} + u \times \boldsymbol{B}) \quad (2.9)$$

Lorentz Force $$\boldsymbol{F_L} = \boldsymbol{J} \times \boldsymbol{B} \quad (2.10)$$

In MHD, the charge density ρ_e is considered immaterial. It is assumed that the positive and negative charges are equilibrated on the time scale relative to the speed of light, i.e. practically immediately in comparison to the typical time scale of the flow. As such, Gauss's law is dropped and the charge conservation equation (2.8) is reduced to equation (2.11). Also, in MHD, the displacement currents are negligible compared to the current density $\boldsymbol{J}$, therefore, Ampere-Maxwell equation (2.7) reduces to equation (2.12). The MHD equations become (2.11) to (2.16). Detailed derivations can be found in many textbooks including [1] and [27].

$$\nabla . \boldsymbol{J} = 0 \tag{2.11}$$

$$\nabla \times \boldsymbol{B} = \mu_0 J \tag{2.12}$$

$$\nabla \times \boldsymbol{E} = -\frac{\partial B}{\partial t} \tag{2.13}$$

$$\nabla . \boldsymbol{B} = 0 \tag{2.14}$$

$$\boldsymbol{J} = \sigma(\boldsymbol{E} + u \times \boldsymbol{B}) \tag{2.15}$$

$$\boldsymbol{F_L} = \boldsymbol{J} \times \boldsymbol{B} \tag{2.16}$$

2.1.2 MHD Quasi-Static approximation

An imposed steady magnetic field $\boldsymbol{B_0}$ applied to the flow of an electrically conducting fluid in a channel is considered in the current study. The electric current induced in the flow $\boldsymbol{J_0} \sim \sigma \boldsymbol{u} \times \boldsymbol{B_0}$ generates additional magnetic field $\boldsymbol{b}$. The total field, $\boldsymbol{B} = \boldsymbol{B_0} + \boldsymbol{b}$ satisfies the MHD equations in section 2.1.1. The can be simplified using the Quasi-Static approximation for the case of laboratory and industrial flow of liquid metals. The approximation has been derived theoretically [1] and verified experimentally.

In explaining the Quasi-Static approximation, two dimensionless parameters are defined in MHD. The first parameter is the magnetic Reynolds number, which is expressed as,

$$R_m = ul/\lambda = \mu\sigma ul \tag{2.17}$$

The magnetic Reynolds number defines the ratio of advection to diffusion in a magnetic field. U and L are the typical velocity and length scale of the flow. The magnetic Prandtl number is defined as

$$Pr_m = \upsilon/\lambda \tag{2.18}$$

Where ν is the kinematic viscosity of the fluid and $\lambda = 1/(\sigma\mu_0)$ is the magnetic diffusivity. σ and μ_0 are the electric conductivity of the fluid and the magnetic permittivity of vacuum. For almost all technological and laboratory flows of liquid metal including the flows in the

continuous steel casting and liquid metal blankets of the fusion reactors, the magnetic Reynolds number and magnetic Prandtl number are both significantly small

$$R_m \ll 1 , \tag{2.19}$$

$$Pr_m \ll 1 . \tag{2.20}$$

In such cases, the magnetic field $\boldsymbol{b}$ associated with induced currents, $\boldsymbol{J_0} \sim \sigma \boldsymbol{u} \times \boldsymbol{B_0}$, is negligible compared to the imposed magnetic field $\boldsymbol{B_0}$. In another way, it can be approximated that $\boldsymbol{b}$ adjusts instantaneously to changes of the flow velocity. As such, diffusion of the magnetic field dominates its advection, and the two-way coupling between the fluid motion and the magnetic field is reduced to the one-way effect of the magnetic field on the flow. The Lorentz force and Ohm's law are reduced as:

$$\boldsymbol{F_L} = \boldsymbol{J} \times (\boldsymbol{B_0} + \boldsymbol{b}) \approx \boldsymbol{J} \times \boldsymbol{B_0} \tag{2.21}$$

$$\boldsymbol{J} \approx \sigma(\boldsymbol{E_0} + \boldsymbol{u} \times \boldsymbol{B_0}) \tag{2.22}$$

The imposed steady magnetic field is represented by $\boldsymbol{B_0}$ and as the induced magnetic field $\boldsymbol{b}$ is ignored, $\boldsymbol{B_0}$ is replaced with $\boldsymbol{B}$. The electric field $\boldsymbol{E}$ is irrotational (see (2.13)) and can be represented by $-\nabla\varphi$, where φ is the electric potential. Combining with conservation of current equation $\nabla . \boldsymbol{J} = 0$, the current $\boldsymbol{J}$ can be uniquely determined as

$$\boldsymbol{J} \approx \sigma(-\nabla\varphi + \boldsymbol{u} \times \boldsymbol{B}) \tag{2.23}$$

with the potential φ being the solution of the Poisson equation

$$\nabla^2\varphi = \nabla . (\boldsymbol{u} \times \boldsymbol{B}) . \tag{2.24}$$

2.1.3 Flow configuration and governing equations

A fully developed turbulent flow of an incompressible electrically conducting fluid in a plane channel with electrically perfectly insulating walls is considered in the current study. The flow is driven by an imposed streamwise pressure gradient. A uniform constant magnetic field $\boldsymbol{B}$ is imposed in the wall-normal (z), spanwise (y) or streamwise (x) direction as depicted in figure (2.1).

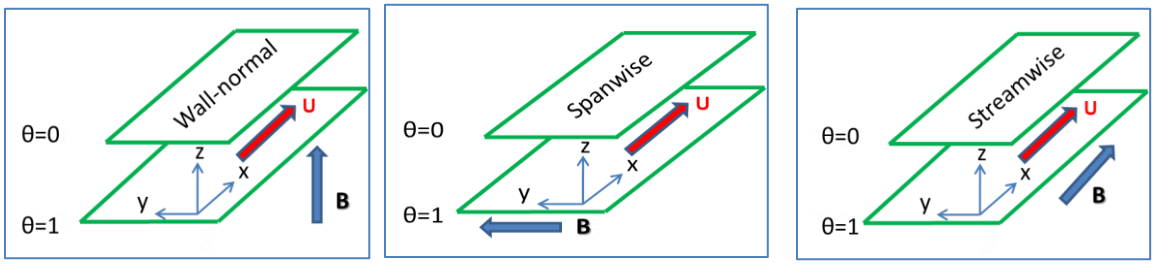

Figure 2.1: Channel flow configuration with different orientations of magnetic field

The quasi-static MHD approximation introduced in section 2.1.2 is assumed to be valid for the electromagnetic part of the model. The system of governing equation reduces to the Navier-Stokes equation with the additional Lorentz force term expressed in equation (2.2) and (2.16), the incompressibility condition (2.1), the Ohm's law for the induced electric current (2.23), the equation for the electric potential expressing the constrain of charge conservation (2.24) and the equation for the transport of passive scalar (2.3). The system of equations is summarized below.

$$\frac{\partial \boldsymbol{u}}{\partial t} + (\boldsymbol{u}.\nabla)\boldsymbol{u} = -\frac{\mathbf{1}}{\boldsymbol{\rho}}\nabla \boldsymbol{P} + \upsilon\nabla^{\mathbf{2}}\boldsymbol{u} + \boldsymbol{J} \times \boldsymbol{B} \tag{2.25}$$

$$\nabla.\boldsymbol{u} = \mathbf{0} \tag{2.26}$$

$$\boldsymbol{J} = \sigma(-\nabla\varphi + \boldsymbol{u} \times \boldsymbol{B}) \tag{2.27}$$

$$\nabla^2\varphi = \nabla.(\boldsymbol{u} \times \boldsymbol{B}) \tag{2.28}$$

$$\frac{\partial\theta}{\partial t} + \boldsymbol{u}.\nabla\theta = \lambda\nabla^2\theta \tag{2.29}$$

In order to non-dimensionalize the equations (2.25) to (2.29), the channel half-width of the duct L as the typical length scale, mean velocity U as the velocity scale, ρU^2 as the pressure scale, the imposed magnetic field strength B as the magnetic field scale, the combination parameter U, LB as the electric potential, σUB as the scale for current density and the scalar difference between the walls as the scale for the scalar field are used. The equations in non-dimensional form are:

$$\frac{\partial \boldsymbol{u}}{\partial t} + (\boldsymbol{u}.\nabla)\boldsymbol{u} = -\nabla \boldsymbol{p} + \frac{1}{Re}\nabla^2\boldsymbol{u} + \boldsymbol{N}(\boldsymbol{j} \times \boldsymbol{e_B}) \tag{2.30}$$

$$\nabla.\boldsymbol{u} = \boldsymbol{0} \tag{2.31}$$

$$\boldsymbol{J} = \sigma(-\boldsymbol{\nabla}\varphi + \boldsymbol{u} \times \boldsymbol{B}) \tag{2.32}$$

$$\nabla^2\varphi = \nabla.(\boldsymbol{u} \times \boldsymbol{e_B}) \tag{2.33}$$

$$\frac{\partial\theta}{\partial t} + \boldsymbol{u}.\nabla\theta = \frac{1}{PrRe}\nabla^2\theta \tag{2.34}$$

Where $\boldsymbol{u}$ = (u,v,w), p, θ, j and φ are, velocity, pressure, passive scalar, current density and electric potential fields respectively. The unit vector $\boldsymbol{e_B}$ indicates the direction of the magnetic field.

The non-dimensional parameters are the Reynolds number

$$Re \equiv \frac{UL}{\upsilon} \tag{2.35}$$

The Prandtl number

$$Pr \equiv \frac{\upsilon}{\chi} \tag{2.36}$$

Where χ is the scalar diffusivity

and either the Hartmann number

$$Ha \equiv BL\left(\frac{\sigma}{\rho\upsilon}\right)^{1/2} \tag{2.37}$$

Or the magnetic interaction parameter

$$N \equiv \frac{Ha^2}{Re} = \frac{\sigma B^2 L}{\rho U} \tag{2.38}$$

which represents the relative importance of the Lorentz and inertial forces and can be viewed as a measure of the strength of the effect of the magnetic field on the flow. Large Stuart number means that the effect of the Lorentz force is strong and rapid. In most of the cases presented in the dissertation, the Stuart number is not small, thus the velocity field can be assumed transformed by the Lorentz force substantially.

2.2 Boundary conditions

The boundary condition in the streamwise and spanwise directions involve periodicity of the electric potential φ, velocity u, scalar fluctuations θ and pressure p at x = 0, L (L is the length of the channel). The channel walls are assumed to be perfectly electrically insulating, impermeable and allowing no slip of velocity, and maintained at constant values of the scalar. The non-dimensional form of the boundary conditions is:

$$u = 0 \; at \; z = \pm 1 \tag{2.39}$$

$$\frac{\partial \varphi}{\partial n} = 0 \; at \; z = \pm 1 \tag{2.40}$$

$$\theta = 1 \; at \; z = -1, \theta = 0 \; at \; z = 1 \tag{2.41}$$

The flow is driven by an imposed uniform streamwise gradient of mean pressure (not shown in equation (2.25) which is adjusted after time step to maintain the non-dimensional mean streamwise velocity equal to 1. Another integral requirement imposed in the solution is that of zero total electric current in the computational domain:

$$\int \boldsymbol{j} \, dx = 0 \tag{2.42}$$

2.3 Numerical method and discretization Scheme

Numerical methods used in the current study are described here. The discussion concerns the time and space discretization scheme as well as parameters and grids used in the simulations.

2.3.1 General Features

The works presented in Chapter III-V have been carried out conducting Direct Numerical Simulation (DNS) using the updated version of the numerical method described as the scheme B in Krasnov et al. [28]. The pressure field is computed using the standard projection method, so that the velocity field satisfies the incompressibility condition. The time integration scheme is of the second order and based on the backward differentiation-Adam-Bashfort discretization scheme. Two Poisson equations: the projection method equation for pressure (2.47) and electric potential equation (2.43) are solved at every time

step using FFT in the stream-wise direction and the cyclic reduction solver in the y-z plane. Each time step includes the following substeps: from time t^n to $t^{n+1} = t^n + \Delta t$

1. The electric potential equation is solved as:

$$\nabla^2 \varphi^n = \nabla . (\boldsymbol{u}^n \times \boldsymbol{e}) \tag{2.43}$$

2. The electric current is computed as:

$$\boldsymbol{j}^n = -\nabla \varphi^n + (\boldsymbol{u}^n \times \boldsymbol{e}) \tag{2.44}$$

3. The right-hand side of the Navier-Stokes equation is computed explicitly as:

$$\boldsymbol{F}^n = -(\boldsymbol{u}^n . \nabla)\boldsymbol{u}^n + \frac{1}{Re}\nabla^2 \boldsymbol{u}^n + N(\boldsymbol{j}^n \times \boldsymbol{e}) \tag{2.45}$$

4. The intermediate velocity $\boldsymbol{u}^*$ is calculated as:

$$\frac{3\boldsymbol{u}^* - 4\boldsymbol{u}^n + \boldsymbol{u}^{n-1}}{2\Delta t} = 2\boldsymbol{F}^n - \boldsymbol{F}^{n-1} \tag{2.46}$$

5. The pressure equation is solved as:

$$\nabla . (\nabla p^{n+1}) = \nabla^2 p^{n+1} = \frac{3}{2\Delta t}\nabla . \boldsymbol{u}^* \tag{2.47}$$

6. The pressure correction is added to restore the solenoidality of the velocity field as:

$$\boldsymbol{u}^{n+1} = \boldsymbol{u}^* - \frac{2}{3}\Delta t \nabla p^{n+1} \tag{2.48}$$

7. Solving the scalar transport equation for scalar:

$$\frac{3\theta^{n+1}-4\theta^{n}+\theta^{n-1}}{2\Delta t}=\frac{1}{PrRe}\nabla^{2}\theta^{n+1}+2P^{n}-2P^{n-1} \tag{2.49}$$

Where $P^{n}=-\nabla\theta^{n}\boldsymbol{u}^{n}$.

2.3.2 Computational grid and spatial discretization

The spatial discretization is based on the finite-difference scheme of the second-order. The scheme is fully conservative in regard to mass, momentum, energy, scalar and electric charge conservation. The only deviation from the local conservation principle is for kinetic energy for which the error is of the third order and dissipative and such does not affect the accuracy and stability of the scheme [29]. The discretized computational grid is clustered in the wall-normal direction to provide adequate numerical resolution of the MHD boundary layer. The discretization is conducted on a non-uniform grid clustered toward the walls of the channel according to:

$$y=\frac{tan\,h(A_y\eta)}{tan\,h(A_y)},\;\; z=\frac{tan\,h(A_z\xi)}{tan\,h(A_z)}, \tag{2.50}$$

or

$$y=\;C_y\,sin(\pi\xi/2)+\left(1-C_y\right)\xi,\;z=\;C_z\,sin(\pi\eta/2)+(1-C_z)\eta. \tag{2.51}$$

where $-1\leq\xi\leq\;1$ and $-1\leq\eta\;\leq\;1$ are the transformed coordinates, in which the grid is uniform. The stretching coefficients A_y, A_z determine the degrees of near-wall clustering in (2.50). In (2.51), C_y and C_z are the blending coefficients of the Chebyshev and identity transformations. The values $C_y=C_z=0.96$ are typically used.

2.3.3 Solution treatment of Poisson equations

Periodicity in streamwise direction for the channel flow is considered as an approximation for flow homogeneity. As such, the Poisson equations (Pressure and electric potential) are solved using the method described in [28] which uses the FFT transform in the periodic coordinate. The two-dimensional Poisson equations for the Fourier coefficient are written in terms of the transformed coefficient as general separable elliptic PDEs. Central difference of second order has been used to discretize the equations and solved by the cyclic reduction direct solver in the y-z plane which is a part of software package Fishpack [30].

2.3.4 Space discretization

The discretization has been conducted directly on the non-uniform grid in the physical coordinates. The collocated grid arrangement is used for the solution variables $\boldsymbol{u}$, $\boldsymbol{p}$, $\boldsymbol{j}$ and φ, which are all stored at the same grid points. The equations (2.43)-(2.49) are also approximated at these points. In collocated grid arrangement, the intermediate velocity (2.46) and current fluxes (2.44) are all computed at half-integer grid points located midway between the regular grid points in a staggered arrangement shown in figure 2.2 below. The collocated grid arrangement for the proposed scheme is considered as finite difference to advance the solution.

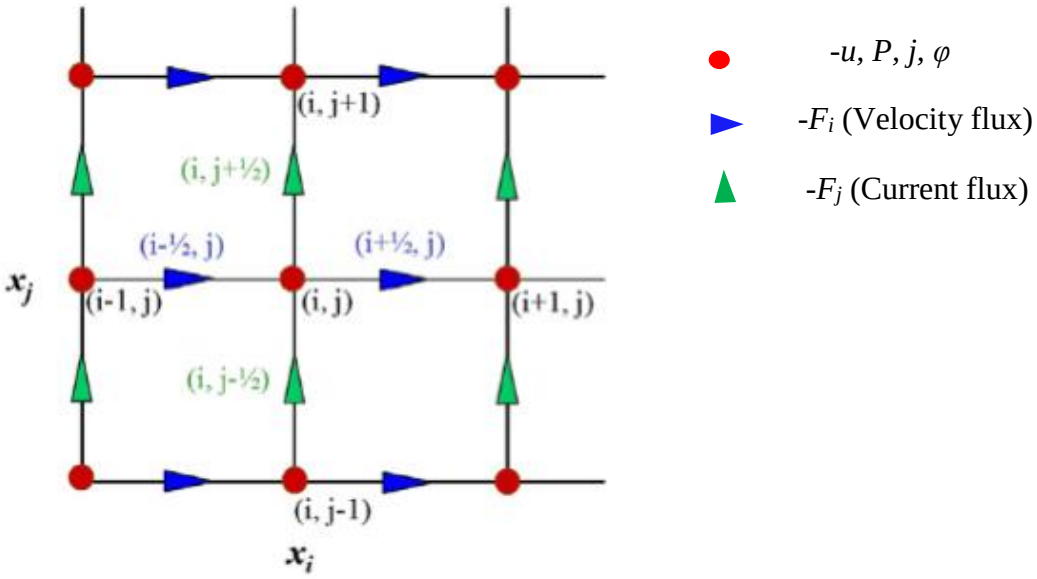

Figure 2.2: Collocated grid arrangement for discretized solution variables (source: [28])

The first order derivatives are approximated by the following discretization formula:

At regular grid points: $$\left.\frac{\delta_2 f}{\Delta\delta_2 x}\right|_{x_i} \equiv \frac{1}{2}\frac{f_i - f_{i-1}}{x_i - x_{i-1}} + \frac{1}{2}\frac{f_{i+1} - f_i}{x_{i+1} - x_i} \tag{2.52}$$

At staggered grid points: $$\left.\frac{\delta_1 f}{\delta_1 x}\right|_{x_i} \equiv \frac{f_{i+1/2} - f_{i-1/2}}{x_{i+1/2} - x_{i-1/2}} \tag{2.53}$$

For staggered grid points: $$\left.\frac{\delta_1 f}{\delta_1 x}\right|_{x_{i+1/2}} = \frac{f_{i+1} - f_i}{x_{i+1} - x_i} \tag{2.54}$$

Linear interpolations between regular and staggered grids have been used as:

$$f_{i+1/2} = \frac{f_i + f_{i+1}}{2} \tag{2.55}$$

$$f_i \equiv f_{i+1/2} - (f_{i+1/2} - f_{i-1/2})\frac{x_{i+1/2} - x_i}{x_{i+1/2} - x_{i-1/2}} \tag{2.56}$$

The velocity fluxes at half-integer points are calculated at the velocity collection substep (equation 2.48) using the Rhie and Chow interpolation formula [31]:

$$F_i^{n+1} = u_i^{xi} - \frac{2\Delta t}{3}\frac{\delta_1 p^{n+1}}{\delta_1 x_i} \tag{2.57}$$

$$F_i^{n+1} = u_i^{xi} - \frac{2\Delta t}{3}\frac{\delta_1 p^{n+1}}{\delta_1 x_i} \tag{2.58}$$

The incompressibility is imposed in velocity fluxes as:

$$\frac{\delta_1 F_i}{\delta_1 x_i} = 0 \tag{2.59}$$

The electric current fluxes at half-integer points are based on conservative approach outlined in [32]:

$$G_i^n = -\frac{\delta_1 \varphi^n}{\delta_1 x_i} + (\boldsymbol{u}^n \times e)_i^{x_i} \tag{2.60}$$

Current conservation condition is approximated as

$$\frac{\delta_1 G_i^m}{\delta_1 x_i} = 0 \tag{2.61}$$

The Poisson equation for the electric potential is obtained by substitution of (2.60) into (2.61):

$$\frac{\delta_1}{\delta_1 x_i}\left(\frac{\delta_1 \varphi^n}{\delta_1 x_i}\right) = \frac{\delta_1}{\delta_1 x_i}(\boldsymbol{u}^n \times \boldsymbol{e})_i^{x_i} \tag{2.62}$$

In summary, the electromagnetic part of the problem solution scheme is implemented as follows:

(i) Solution of Poisson equation (equation 2.62)

(ii) Calculation of current fluxes (equation 2.60)

(iii) Interpolation of the current fluxes onto the integer grid points

$$j_i^n = G_i^{nx_i}$$

(iv) Calculation of the Lorentz Forces $N\ (j^n \times e)$ at the integer grid points

There are other aspects of the discretization scheme, namely the treatment of the the boundary conditions at the discretized collocated grid points and the implementation of the Poisson equation solutions through software package Fishpack and Mudpack which have been adopted from [28].

2.4 Parameters and Computational Domain

The problems described in Chapter 3 and 4 in the current study are solved at the Reynolds number Re = 6000 and Prandtl number Pr = 1. The Hartmann number and Stuart Numbers are varied for all configurations of the magnetic field so that the maximum value of Ha and N are sufficiently large to generate substantial MHD effect but still significantly smaller than the laminarization thresholds. Detailed discussion on the rationales behind variations of Ha and N is outlined in Chapter 3. The computational domain has the dimensions $2\pi \times 2\pi \times 2$ in the streamwise, spanwise and wall-normal directions respectively. The computational grid consists of 256^3 points. The wall clustering parameter is chosen as A=1.5 for all configurations. The minimum grid step Δz near the wall is 2.34×10^{-3} while the maximum Δz at the center of the channel is 1.29×10^{-2} as a result of the clustering. The results of DNS of channel flows with spanwise [25] and wall-normal [23] magnetic fields conducted at closed values of Re and Ha confirm that the size of the domain and the grid resolution used in the study are sufficient for an accurate DNS.

The numerical model has been verified by running test cases and comparing the results with MHD flow computations [20, 23, 25] and DNS of scalar transfer in turbulent channel flows without and with magnetic field [33, 34].

In Chapter 5, the simulations are conducted at the Reynolds number of 5333. The explored range of the Hartmann number is $30 \leq Ha \leq 160$. The Prandtl number $Pr = 1$ is chosen for all the computations. The computational domain has the dimensions of $2\pi \times 4\pi \times 2$ in the streamwise, spanwise, and wall-normal directions, respectively. The computational grid consists of $64 \times 64 \times 80$ points. The points are distributed uniformly in the streamwise and spanwise directions and clustered toward the walls using the coordinate transformation per equation (2.50) and (2.51) with $A = 1.5$.

CHAPTER III

FLOW FIELD IN MHD CHANNEL FLOW WITH DIFFERENT ORIENTATIONS OF MAGNETIC FIELD

3.1 Background

The key focus of the proposed doctoral study is to obtain understanding of transport of a passive scalar (temperature or concentration of an admixture) in magnetohydrodynamic (MHD) turbulent flows. The magnetic field influences the transport indirectly, via transformation of the velocity field. As such, the effects of the magnetic field of various orientations on the flow itself are analyzed prior to the scalar transport analysis. In this chapter, the transformation of flow field and turbulent transport characteristics are discussed. The resultant effects on passive scalar transport due to the transformation of flow field have been discussed in Chapter 4. Outcomes of proposed doctoral research investigations which are described in Chapter 3 and 4 have been published in [35].

3.2 Review on earlier works

As discussed in Chapter 2, for the case of low-R_m MHD flow, magnetic Reynolds number (R_m) and the magnetic Prandtl number (Pr_m) are assumed to be much smaller than 1. Such flow is typical for industrial and laboratory flows of liquid metals and other electrically conducting fluids. In many such flows, for example in continuous steel casting or growth of large semiconductor crystals, transport of heat and admixtures is technologically important. The magnetic fields are, in fact, often imposed with the explicit goal of controlling the transport (see, e.g. [1]). Usually, the effect of the magnetic field occurs in the presence of electrically insulating walls and strong mean shear of the flow. This forms

the motivation of the proposed doctoral research. It has been analyzed in the current study that how an imposed constant and uniform magnetic field affects scalar transport in the archetypical turbulent flow with walls and mean shear channel flow. In this section, a brief review of earlier works addressing this question has been made. The magnetic field influences the transport indirectly, via the transformation of the velocity field. Therefore, the review starts with the effect on the flow in this chapter. A review on earlier work on scalar transport is made in Chapter 4.

The basic features of an imposed constant magnetic field on a turbulent flow of an electrically conducting fluid are relatively well understood. The main defining parameter is the magnetic interaction parameter (the Stuart number-defined in Chapter 2, 2.38). The parameter can be viewed as the ratio of the eddy turnover time $\tau_{eddy} \equiv L/U$ to the Joule damping time $\tau_J \equiv \rho/\sigma B^2$ where σ and ρ are the electric conductivity and density of the fluid, $\boldsymbol{B}$ is the imposed magnetic field, and L and U are the typical length and velocity scales. For homogeneous turbulence without mean shear, the main feature of the transformation is the structure anisotropy of velocity and pressure fluctuations, which appears as elongation of flow structures in the direction of the magnetic field (see, e.g., [13, 36]). The anisotropy results from the action of the Joule dissipation that damps velocity gradients along the magnetic field lines. Interestingly, the structure anisotropy of approximately equal strength develops in a wide range of length scales, from the largest energy containing scales to the beginning of the dissipation range [37]. Anisotropy of another kind, namely the inequality of the average velocity components (the anisotropy of the Reynolds tensor of turbulent stresses), is not generated directly by the magnetic field, but develops as a part of the flow transformation. The form and degree of this anisotropy depend on the boundary conditions and the stage of the flow evolution (e.g., the study of decaying turbulence [38] as an example).

The mechanisms leading to the anisotropy of Reynolds stress tensor are nonlinear and complex. They are not fully understood, except in the case of large magnetic interaction parameter N, when the flow evolution is dominated by the Joule dissipation (e.g., [12, 39]).

In the presence of mean shear, the effect of the magnetic field is modified. For the case of homogeneous turbulence, this is analyzed in [40]. It is found that the flow transformation is largely determined by the ratio of the typical time scale associated with the mean shear $\tau_{shear} \equiv 1/S$, where S is the shear rate, and the Joule damping time τ_J . The effects of the shear or of the magnetic field are dominating if τ_{shear}/τ_J is, respectively, larger or smaller than one.

Among the possible configurations of the channel flow with imposed uniform magnetic field, the most extensively studied is that of the classical Hartmann flow, in which the magnetic field is in the wall-normal direction, and the walls are electrically insulating (see figure 2.1 in Ch 2 with configurations) (e.g., [16, 18, 20, 21, 23, 41]). At a sufficiently strong magnetic field, the flow acquires a structure with two regions: the core with suppressed turbulence and nearly flat mean velocity profile, and the Hartmann boundary layers with strong mean shear and turbulence. The friction drag increases with the strength of the magnetic field in high-*Ha* high-*Re* flows because of stronger mean shear near the walls, except in a small range of weak fields. At small *Ha*, such as those considered in the present study, the effect is offset by suppression of turbulent momentum transfer and the friction drag decreases slightly.

The case of a spanwise (parallel to the walls and perpendicular to the flow) magnetic field is considered in [20] and [25]. Differently from the wall-normal magnetic field, the spanwise field does not interact directly with the mean flow. The mean flow is affected indirectly, via suppression of turbulent fluctuations leading to reduction of wall-normal momentum transport. The cumulative effect is that of reduction of friction drag and modification of the mean flow profile characterized by increased centerline velocity and absence of log-layer behavior. The typical size of the coherent structures of the flow increases in the spanwise and streamwise directions [25].

Based on the literature review, the only work that considers the effect of a streamwise magnetic field on a turbulent channel flow was [20]. The streamwise magnetic field does not interact directly with the mean flow, but has an indirect effect via modification of turbulent fluctuations. The fluctuations of the spanwise and wall-normal velocity components are suppressed, while the fluctuations of the streamwise velocity component become stronger, as a result of stabilization of streamwise streaks. There is some drag reduction, although weaker than in the spanwise field case. In general, a noticeable modification of the flow requires considerably higher values of N in the case of the streamwise magnetic field than in the other two cases.

3.3 Results and Discussion

In the light of the literature review in the preceding section, the current study explores the classic wall-normal magnetic orientation initially to reproduce the results obtained with the given problem and grid resolution. Afterwards, the spanwise and streamwise magnetic field orientations have been investigated in great details. The new features from the current DNS study which are presented in this section involve exploring the effects of streamwise magnetic field extensively which has not been reviewed previously, estimation of flow statistics and eddy viscosity, detail explanations of flow transformation and structure anisotropy in light of the scalar transport mechanism.

The flows at the same at the same value of $Re = 6000$ and various values of Ha are computed per Table 3.1. For each magnetic field orientations, the Ha numbers are varied keeping in mind turbulent to laminar transition under the effect of imposed magnetic field. For all the configurations of the magnetic field, the maximum values of Ha and N are selected sufficiently large to generate substantial MHD effect, but still significantly smaller than the laminarization thresholds. The second condition is necessary to avoid uncertainties and possible inaccuracies related to the behavior of numerical solutions near the threshold [28, 41]. The laminarization threshold in the case of the wall-normal magnetic field is determined on the basis of the numerical and experimental studies of transition in

Hartmann layers [42, 43] as *Re/Ha* ≈ 380. For $Re = 6000$ which is considered in the current study, the laminarization threshold yields at $Ha \approx 15.8$. In the case of the spanwise field, [25] have found that, at *Re* = 6667, the laminarization occurs at *Ha* between 30 and 40. The only result available for the streamwise magnetic field is that of [20], where it has been found that, at *Re* = 4000, the flow is laminar at *Ha* = 49 and possibly becomes laminar at *Ha* = 35. The threshold should be higher in the current study to higher *Re*. It is found in the current study that the flow remains turbulent at *Ha* = 40, but limited the results presented in the thesis to $Ha \leq 30$ because of the uncertainty introduced by structures of large streamwise scales developing in the streamwise magnetic field at larger *Ha*.

All the flow properties discussed in this section are obtained for fully developed turbulent flows. For each case, the solution is calculated until the friction coefficient and the Nusselt number (Discussed in detail in Chapter IV) become statistically steady. After that, the flow is computed for not less than 1000 time units, which should be compared with the non-dimensional convective time scale *L/U* = 1. The data are collected at this stage.

The mean flow characteristics, such as the mean streamwise velocity *U*(*z*), mean-square fluctuations of velocity, Reynolds stress components are obtained using averaging over time and wall-parallel (*x*-*y*) planes. This operation is denoted in the following text as $\langle \dots \rangle$. For example, the mean velocity is:

$$U\langle z \rangle = \langle u(x, y, z, t) \rangle \tag{3.1}$$

The turbulent fluctuation of velocity is defined as differences between the instantaneous and mean fields:

$$\boldsymbol{u'} = \boldsymbol{u} - \boldsymbol{U e_x} \tag{3.2}$$

As integral characteristics of the flow, the friction coefficient has been used.

$$c_f \equiv \frac{1}{Re}\left.\frac{dU}{dz}\right|_{wall} = \frac{dP}{dx} \tag{3.3}$$

Where dP(x)/dx is the imposed pressure gradient driving the flow. The wall-friction velocity u_τ and the corresponding Reynolds number

$$u_\tau \equiv \sqrt{c_f}\,,\ Re_\tau \equiv\ u_\tau Re \tag{3.4}$$

The analyzed flow regimes are listed in Table 3.1. The table shows the values of the integral characteristics just defined as well as some other properties that will be defined later.

Table 3.1:

Ha, N	U_{cl}	Re_τ	$c_f \times 10^3$	$[\nu_t] \times\ 10^3$
0, 0	1.151	341.6	3.254	3.719
Wall-normal				
5, 0.00417	1.165	343.6	3.279	3.341
10, 0.0167	1.125	343.5	3.218	2.403
13.3, 0.0295	1.099	338.4	3.180	1.389
Spanwise				
10, 0.0167	1.164	335.0	3.121	3.208
20, 0.0667	1.206	311.4	2.678	2.091
30, 0.150	1.280	261.1	1.895	1.005
Streamwise				
10, 0.00417	1.162	340.8	3.234	3.731
20, 0.0667	1.163	338.4	3.180	3.393
30, 0.150	1.160	332.2	3.064	3.551

Table 3.1: Computed Integral Characteristics. U_{cl}-mean velocity at the centerline, Re_τ-Reynolds number based on wall-friction velocity u_τ, c_f friction coefficient, ν_t – volume-averaged turbulent viscosity

3.3.1 Mean Flow

The effect of the magnetic field on the mean flow is illustrated in figure 3.1. In the case of the wall-normal magnetic field, the well-known formation of a flattened core and Hartmann boundary layers of thickness ~L/Ha (see, e.g., [20, 21, 23]) are observed.

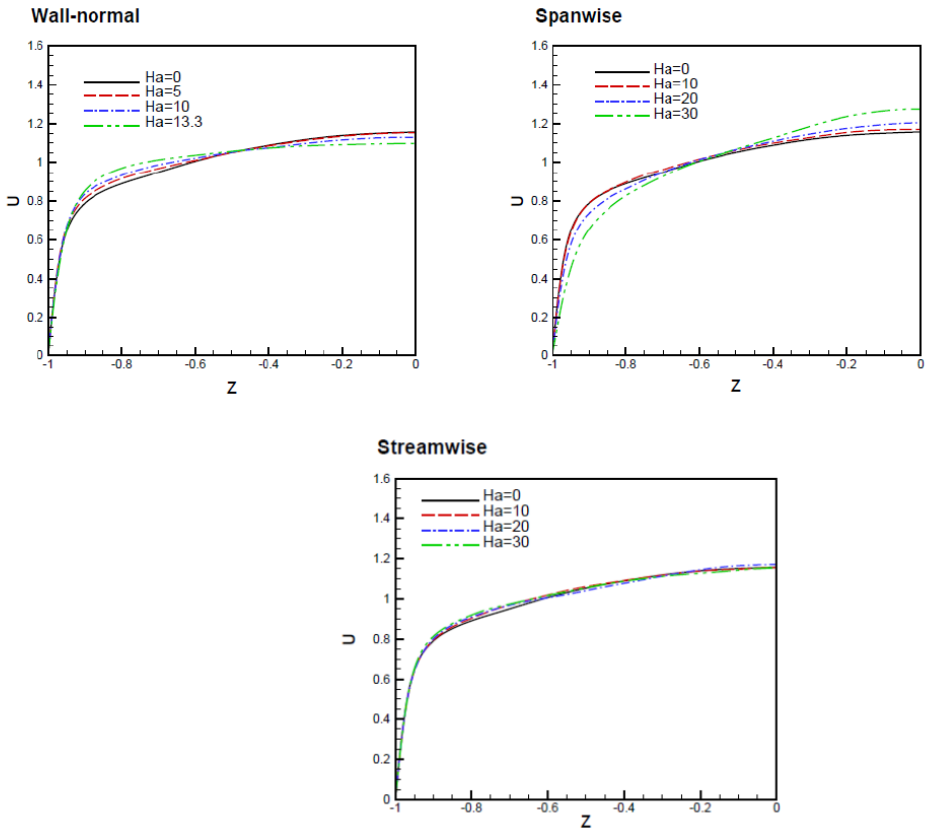

Figure 3.1: Mean velocity profile for different orientations of magnetic field (the orientations are indicated above the plots).

For the case of the spanwise magnetic field, figure 3.1 shows increase of the centerline velocity and widening of the boundary layers. This effect is observed in Krasnov et al. [25] and explained by suppression of wall-normal turbulent momentum transfer. Changes in the center line velocity are also shown by Table 3.1.

Considering the results shown in figure 3.1 for the case of the stream wise magnetic field, the effect is observed at the same values of Ha, as significantly weaker than in the other two cases (this was also observed in [20]). The mean velocity profile barely changes with Ha numbers. It is noted as in the spanwise case, there is no direct interaction between the mean flow and the magnetic field. As it will be discussed in next section, the indirect effect via the suppression of turbulent fluctuations is also not strong.

3.3.2 Log-Layer behavior of the mean flow

In turbulent channel flow, the mean velocity at a point is proportional to the logarithm of the distance from that point to the wall according to the log-layer profile of the wall.

The effect of the magnetic field on the log-layer behavior of the mean flow velocity has been analyzed by computing the coefficient γ which is expressed as:

$$\gamma = z^+ \frac{dU^+}{dz^+} \tag{3.5}$$

where $U^+ = U/u_\tau$ and $z^+ = (z+1)Re_\tau$ are the velocity and distance in wall units. The coefficient should be constant and equal to the reciprocal von Karman constant in the area where U(z) follows the log-law. The data obtained for the flow with Ha = 0 and for flows with the highest Ha for each orientation of the magnetic field are shown in figure 3.2. For the flow without magnetic field, we see results typical of moderate-Re turbulence. Approximate log-law behavior starts at z + about 40. The results obtained for the wall-normal and spanwise magnetic fields are in agreement with the results of, correspondingly, [23] and [25]. In the wall-normal case, the log-layer behavior is approximately as well-defined as in the hydrodynamic case. The reciprocal von Karman constant γ is somewhat smaller. If the magnetic field is spanwise, the log-layer behavior disappears altogether. For the case of the streamwise magnetic field, the log-layer behavior is similar to that of the hydrodynamic case.

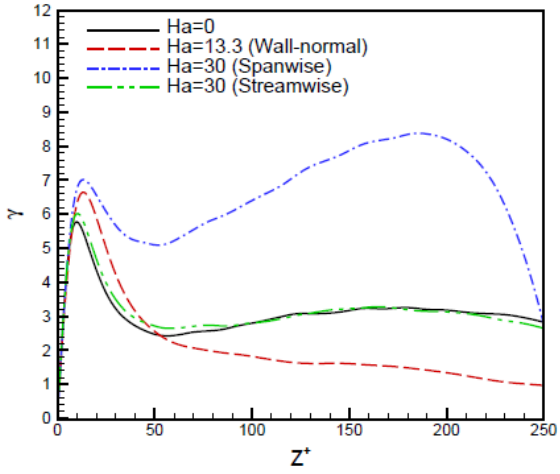

Figure 3.2: Coefficient γ for flow without magnetic field and flows with strongest magnetic fields for each orientation of magnetic field

3.3.3 Profile of mean square velocity fluctuations

The flow transformation under the action of the magnetic field becomes clearer if the profiles of mean square velocity fluctuations shown in figures 3.3 and 3.4 are considered. Figure 3.4 also shows the profiles of the Reynolds stress component $\tau_{13} = \langle u'w' \rangle$ representing turbulent transport of momentum in the wall-normal direction. It is observed that the wall-normal and spanwise magnetic fields result in noticeable reduction of perturbations of all three velocity components. Suppression of $\langle v'^2 \rangle$ and $\langle w'^2 \rangle$ is particularly strong. The streamwise magnetic field suppresses $\langle v'^2 \rangle$ and $\langle w'^2 \rangle$, although to a significantly smaller degree. There is practically no influence of the streamwise magnetic field on the fluctuations of the streamwise velocity component (figure 3.3). Moreover, one can detect slight increase of $\langle u'^2 \rangle$ with *Ha*. An evident explanation is that the streamwise velocity fluctuations appear primarily in the form of streaks, which have very weak gradients in the streamwise direction and, thus, are the structures least suppressed and, possibly, enhanced via stabilization by the streamwise magnetic field.

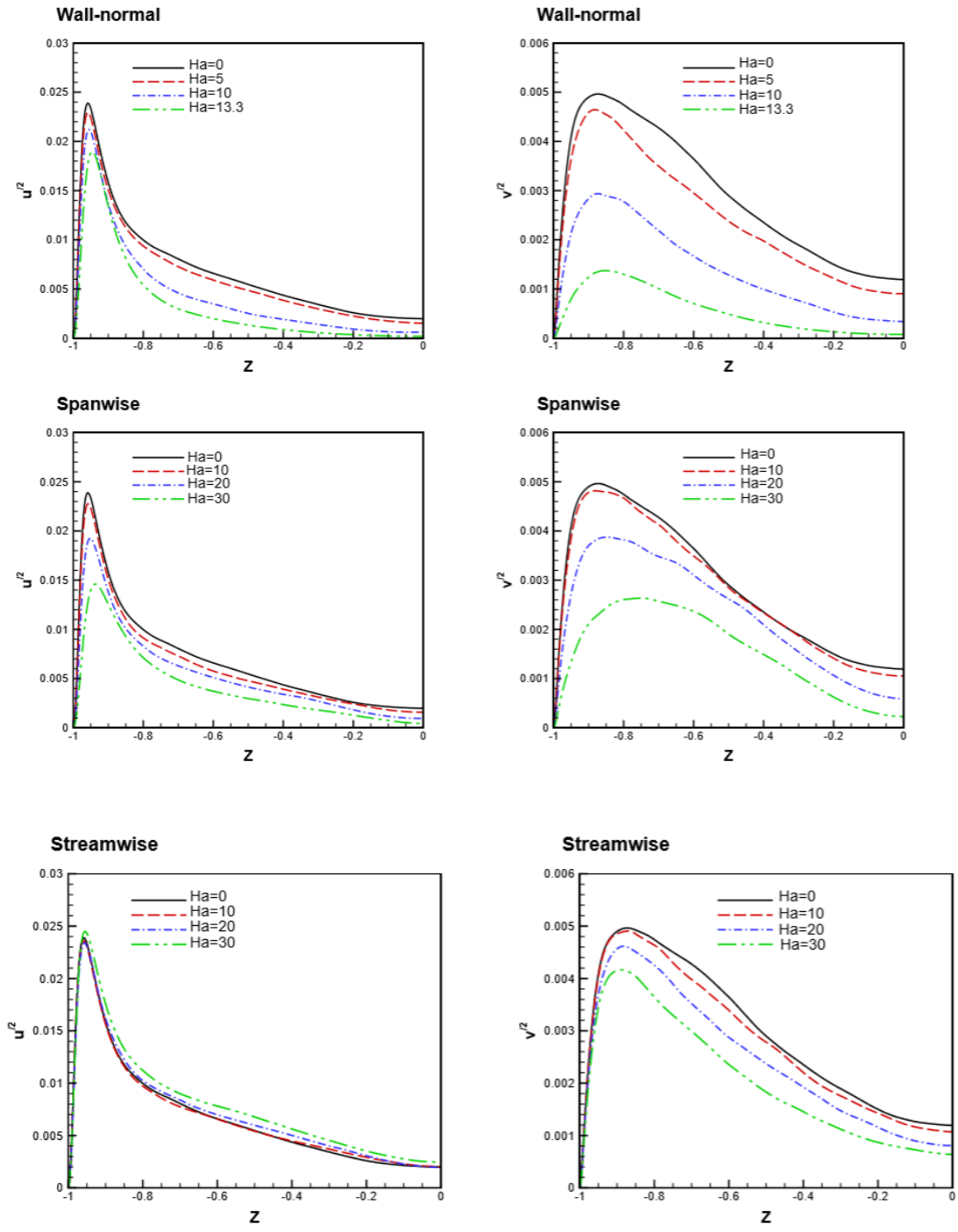

Figure 3.3: Profiles of mean-square fluctuations of streamwise (left) and spanwise (right) velocity components.

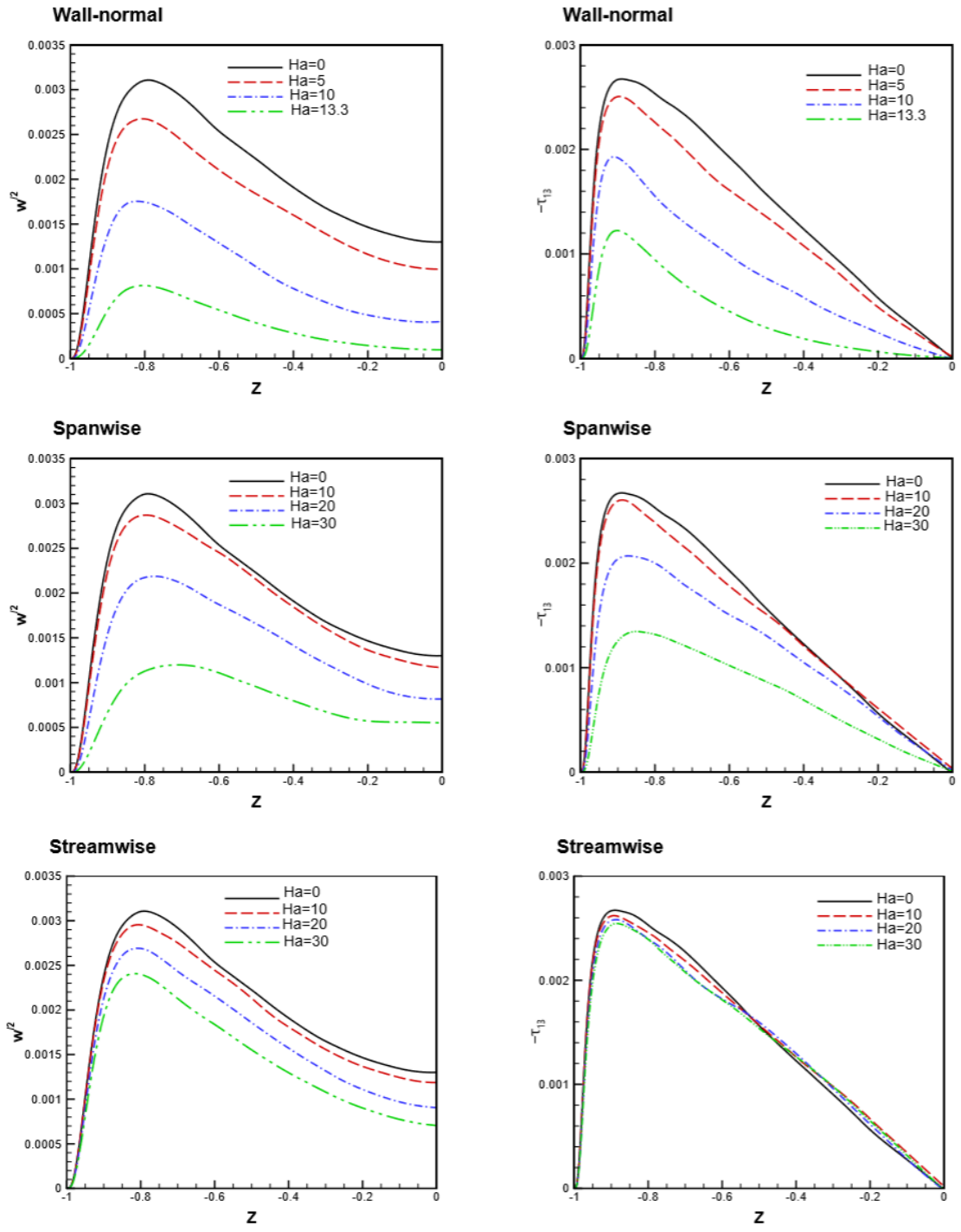

Figure 3.4: Profiles of mean-square fluctuations of wall-normal velocity component (left) and wall-normal turbulent stress (right).

The suppression of the velocity fluctuations leads to reduction of the turbulent stress τ_{13} . As one can see in figure 3.4, the reduction is significant in the cases of wall-normal and spanwise magnetic fields and much less so in the case of the streamwise field. This results in lower wall friction (see the values of c_f and Re_τ in table 3.1).

3.3.4 Turbulent eddy viscosity

The turbulent eddy viscosity has been computed as:

$$\upsilon_t(z) = -\frac{\tau_{13}}{dU/dz} \tag{3.6}$$

The results are presented in figure 3.5. The figure also shows the eddy viscosity volume-integrated over the interior of the channel per the expression in (3.7).

$$[\upsilon_t(z)] = -\frac{1}{1.8}\int_{-0.9}^{0.9} \upsilon_t(z)dz \tag{3.7}$$

The integration limits are z = ±0.9 are chosen so as to exclude the boundary layer behavior (see figures 3.1-3.4). Values of $[\nu_t]$ are listed in table 3.1. One can see that the suppression of turbulent fluctuations by the magnetic fields results in reduction of the eddy viscosity, which is strong in the cases of wall-normal and spanwise field and, at the same Ha, much weaker in the case of the streamwise field. For the case of the streamwise field, the effect of the magnetic field in suppressing the wall-normal component of turbulent fluctuations is weak which results in less reduction of momentum transfer. As a result, the magnitude of eddy viscosity does not decrease with the increase of magnetic field strength.

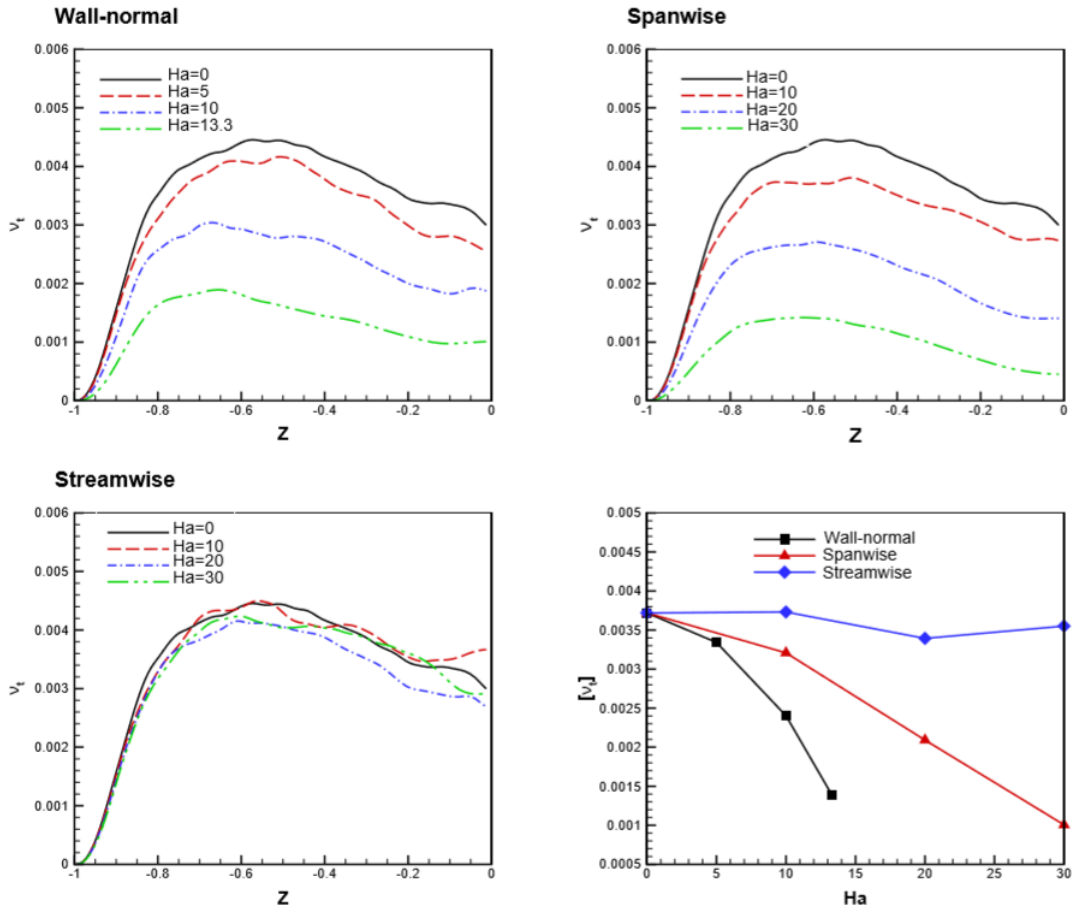

Figure 3.5: Top row and the left figure in the bottom row: Turbulent eddy viscosity (21) as a function of wall-normal coordinate. The orientations of the magnetic field are as indicated above each plot. The right figure in the bottom row shows eddy viscosity integrated over z from $z = -0{:}9$ to $z = 0{:}9$.

3.3.5 Transformation of the spatial structure of the flow

The transformation of the spatial structure of the flow caused by the magnetic fields has been analyzed using instantaneous velocity distributions in the planes z =const, x = const, and y=const . The results mostly confirm the conclusions made in earlier studies, such as [20, 23, 25]. This includes the effect of the magnetic field on the streamwise streaks near the channel walls. For the case of wall-normal magnetic field orientation, no significant change is observed in the case of wall-normal magnetic field at Ha = 5 and 10.

At Ha = 13.3, which is close to the laminarization threshold, the streaks become larger in all three directions. Figure 3.6 shows the streamwise velocity spatial structure for different strength of magnetic field in wall-normal direction.

The spanwise field results in the streaks, which are much weaker and have larger wall-normal and spanwise length scales than in the hydrodynamic case. As shown in figure 3.7, the streamwise streak has become noticeable for Ha= 30.0. The main effect of the streamwise orientation of magnetic field is the stabilization of the streaks, which become visibly more coherent and increase their typical streamwise length scale. This effect, however, only becomes significant at Ha above 30.

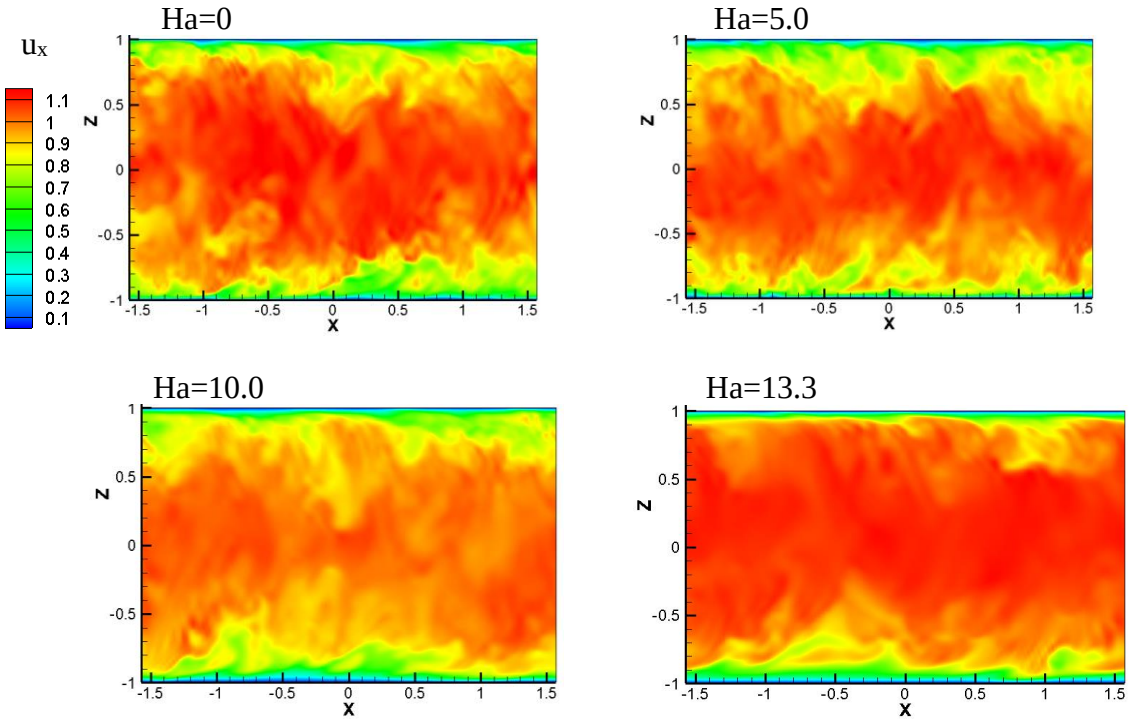

Figure 3.6: Spatial structure of streamwise velocity with wall-normal magnetic field. Instantaneous distributions in the x-z (wall-normal) cross-sections are shown

Analyzing the effect of the magnetic field on the wall-normal and spanwise velocity components, it is found that, in addition to reduction of amplitude, the flow structures acquire larger typical length scales. In agreement with [25], the increase of the typical length scale of turbulent fluctuations is particularly strong in the case of the spanwise magnetic field.

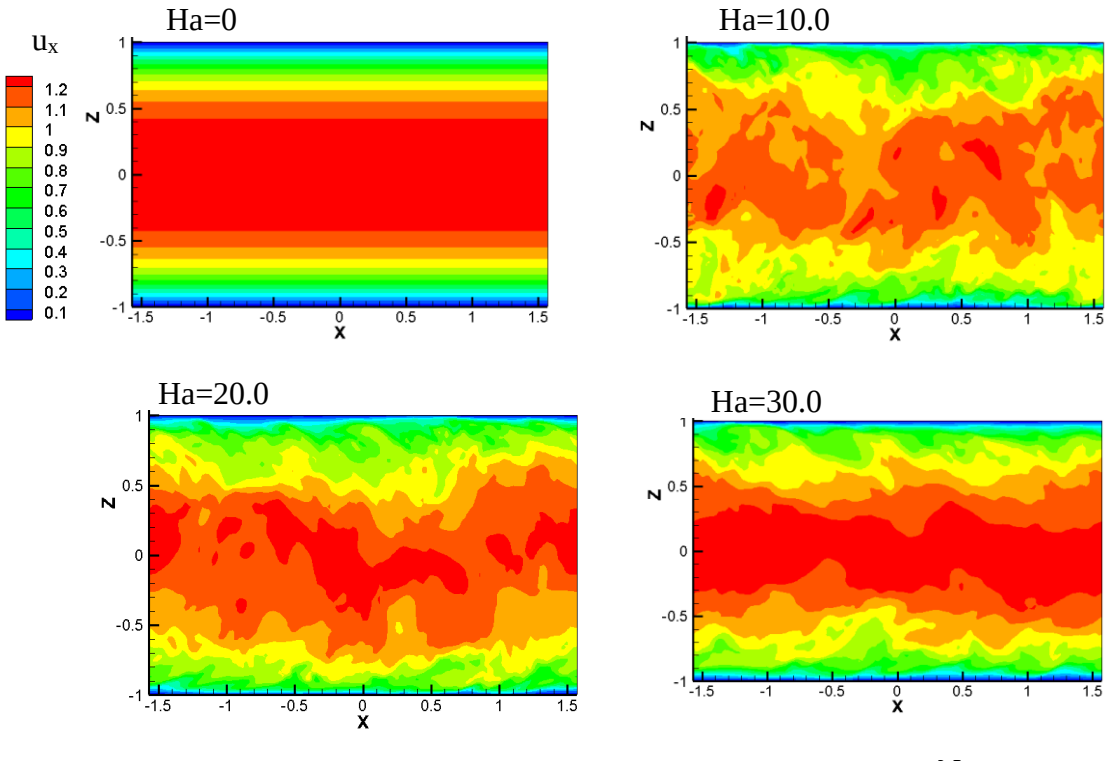

Figure 3.7: Spatial structure of streamwise velocity with span-wise magnetic field. Instantaneous distributions in the x-z (Spanwise) cross-sections are shown.

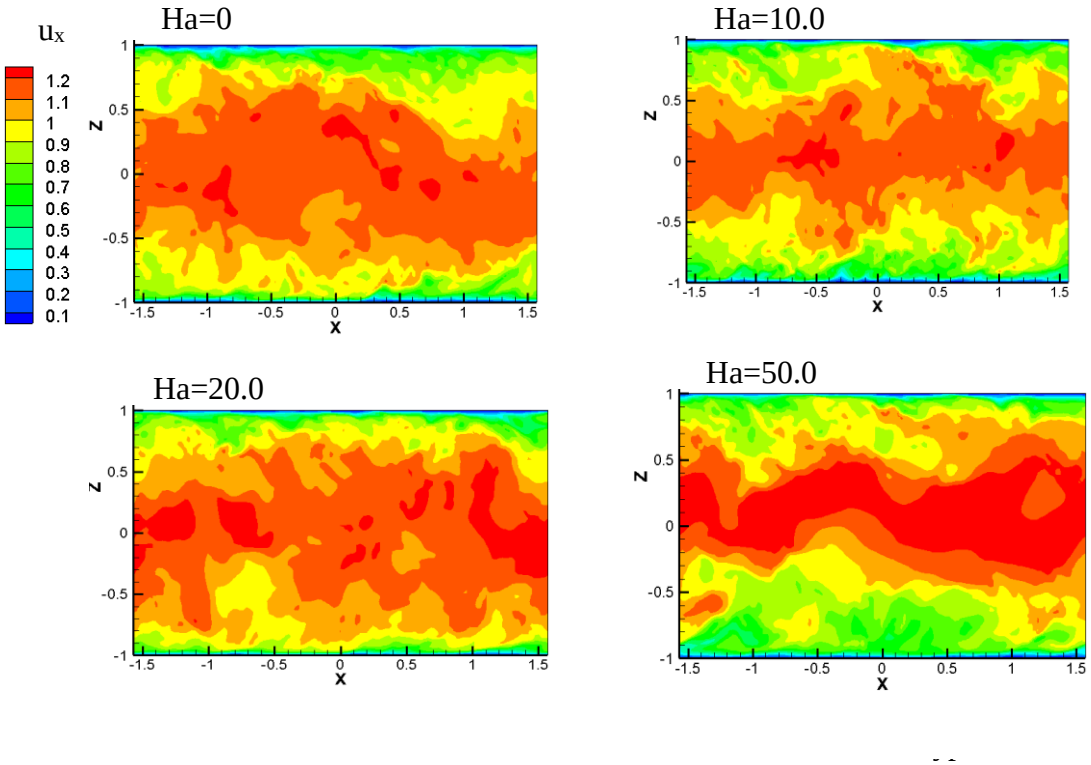

Figure 3.8: Spatial structure of streamwise velocity with streamwise magnetic field. Instantaneous distributions in the x-z (Streamwise) cross-sections are shown.

3.3.6 Structure anisotropy

The transformation of the velocity field can be also analyzed in the framework of the concept of structure anisotropy [44], which is a quantitative assessment of the tendency of a turbulent flow to have structures of different typical sizes in different directions. In the case of the MHD channel flow, the structure anisotropy is created by the magnetic field, which transforms flow structures so that they are elongated along the magnetic field lines, and by the mean shear, which stretches the structures in the streamwise direction. One can use different measures of the structure anisotropy, such as two-point correlations [25], conditional averaging of coherent structures [45], or one-point structure tensors [40, 46]. We follow the version of the last approach that uses the anisotropy coefficients.

$$G_{ij}^{k} \equiv \frac{\langle(\partial u_k/\partial x_i)^2\rangle(1+\delta_{ki})}{\langle(\partial u_k/\partial x_j)^2\rangle(1+\delta_{kj})},\ i \neq j \tag{3.8}$$

Such coefficients have been applied in studies of MHD turbulence [13, 25, 47]. G_{ij}^{k} is equal to one in a flow with perfectly statistically isotropic field and zero in a flow, in which the distribution of u_k is two-dimensional, independent of the coordinate x_i. The results are presented in figure 3.9. The coefficients computed for the stream wise and wall-normal velocity components are shown for the hydrodynamic case and for the cases corresponding to the maximum of Ha for each orientation of the magnetic field. The coefficients G_{13}^{1} and G_{13}^{3} can be interpreted as the typical ratios of wall-normal to streamwise length scales, while the coefficients G_{23}^{1} and G_{23}^{3} show the similar ratios of wall-normal to spanwise scales. It can be observed that the structure anisotropy properties are about the same for the two velocity components. Close to the walls, the wall-normal velocity derivative is much larger than the spanwise and streamwise derivatives in the typical boundary layer behavior. Outside the viscous boundary layer, where the coefficients are more representative of the length scales of coherent flow structures, G_{23}^{1} and G_{23}^{3} approach one in the hydrodynamic case and the cases of wall-normal and streamwise magnetic field. The velocity structures have approximately equal spanwise and wall-normal sizes. In the case of the spanwise velocity field, the coefficients are significantly smaller indicating, in agreement with the results of [25] that the spanwise scale of velocity structures is increased by the spanwise magnetic field.

Considering the coefficients G_{13}^{1} and G_{13}^{3} , the streamwise elongation of flow structures generated by the mean shear should be taken into account. The coefficients are much smaller than one, except in the middle of the channel. The decrease in the case of the spanwise magnetic field was reported in [25] and explained by the increase of the typical streamwise scale. The reduction of the coefficients seen in figure 3.9 for the case of the streamwise magnetic field is evidently also related to the elongation of the flow structure

in the streamwise direction, this time caused by direct action of the anisotropic Joule dissipation.

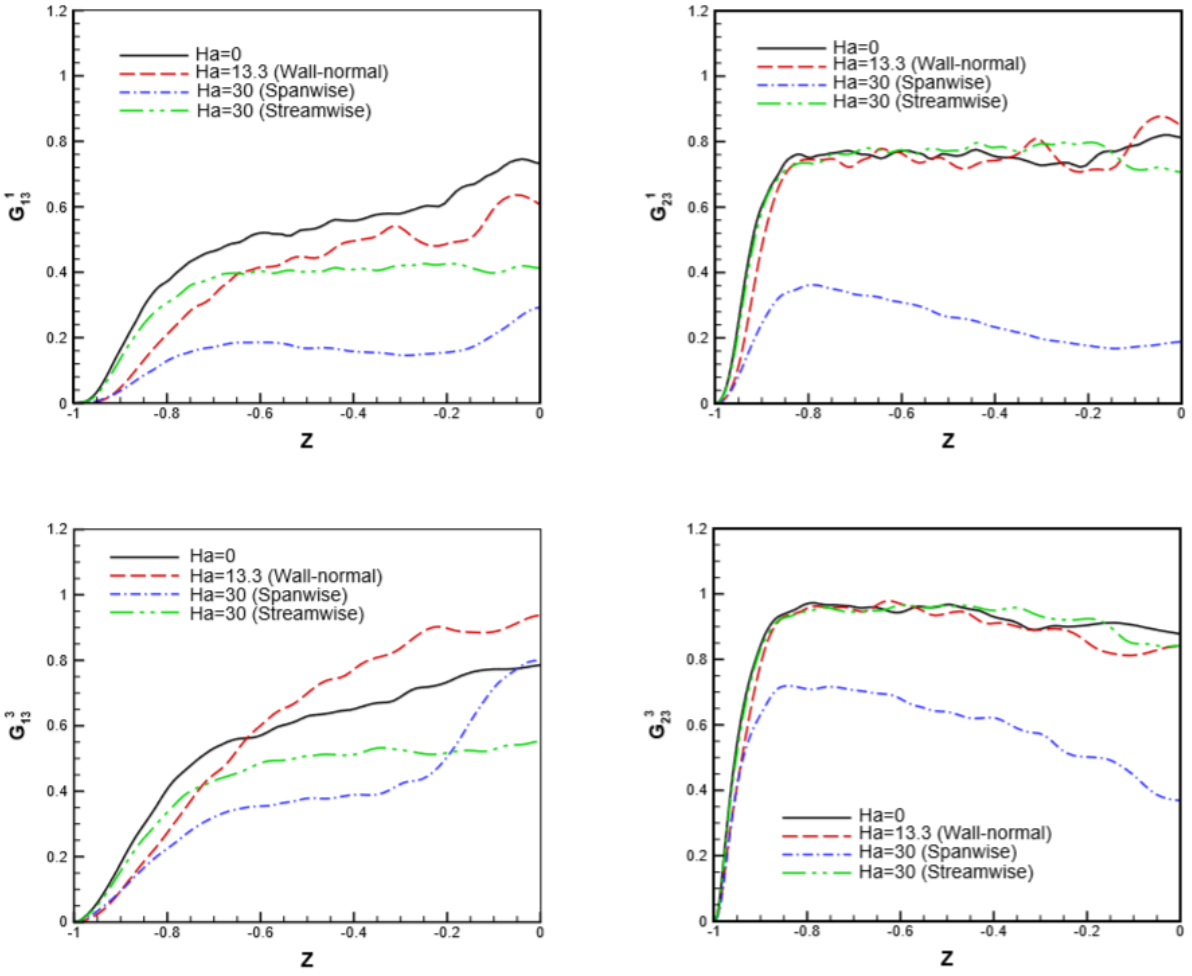

Figure 3.9: Anisotropy coefficients (see (23)) computed for the streamwise (top) and wall-normal (bottom) velocity components. Curves for the flow with zero *Ha* and for flows with the maximum *Ha* at each orientation of the magnetic field are shown.

3.4 Conclusion

The DNS results of the flow field of the MHD turbulent flow in a channel with an imposed uniform magnetic field at different orientations have been discussed in this chapter. The

results concerning the transformation of the flow field is discussed in detail which affects the scalar transport described in Chapter 4. Some of the results discussed regarding the flow field in current study confirm the conclusions made in earlier studies, such as [20, 21, 23, 25, 41] on the basis of DNS and LES conducted at similar *Re* and *Ha*.

CHAPTER IV

PASSIVE SCALAR TRANSPORT IN MHD CHANNEL FLOW

4.1 Background

In this chapter, the results pertaining to passive scalar transport with the effect of the magnetic field has been discussed. There is lack of experimental and numerical studies which focuses on the effect of the imposed magnetic field on turbulent scalar transport, especially in what concerns the role of magnetic field orientation on scalar transport is almost non-existent. As such the current study involves extensive efforts towards understanding the passive scalar transport mechanism under the influence of imposed magnetic field. The chapter begins with the review of earlier works. Comprehensive discussions on mean scalar transport, turbulent flux contributions, role of eddy diffusivity and scalar anisotropy development follows after that. Through the extensive DNS conducted for flow field and scalar transport, the proposed doctoral study yields correlation for scalar transport in the form of Nusselt number with the effect of different orientation and strength of magnetic fields which is highlighted and discussed in this chapter.

4.2 Review on earlier works

A comprehensive literature review has been made as a part of the proposed doctoral research. In this section, a summary of the literature containing passive scalar transport under the influence of an imposed magnetic field is presented.

Yamamoto et al [34] carried out DNS to investigate the magnetohydrodynamic (MHD) pressure loss and heat-transfer characteristics of the low-magnetic Reynolds number and higher Prandtl number (Pr) fluid such as the FLiBe and evaluated the MHD turbulence

model in higher Reynolds number (Re) condition. Non-slip and periodic conditions were imposed for boundary conditions of velocity and the constant temperature at top and bottom boundaries ($T_{top}>T_{bottom}$) and the periodic conditions were imposed for a passive scalar field. The flow found to be laminar at Ha=16.0 and the wall shear stress showed to have temporal intermittency at Ha=13.0 with Ha=13.2 produced laminar result. As a result, the maximum Ha maintaining turbulence was found to be at Ha=13.0. With higher Ha number the suppression of the Reynolds shear stress was increased with the Reynolds shear stress became zero in the whole channel at Ha=16.0. Although the flow found to be laminar at Ha=16.0, the temperature field showed linear profile after long computational time compared to velocity field. The friction drag coefficient and Nusselt number which were obtained from the simulation are mentioned in the table below:

Table 4.1:

Re_τ	Ha	Pr	Friction drag coefficient (C_f)	Nusselt number (Nu)
150	0	5.7	6.33E-6	15.73
150	8	5.7	6.20E-6	14.00
150	12	5.7	5.70E-6	10.53
150	16	5.7	5.55E-6	1.00

Table 4.1: Computational results of DNS by Yamamoto et al [34]

It was observed from the study that the similarity-law between the velocity and temperature profiles was not satisfied with increase of Hartman number (Ha) and was noticeable at the near critical Ha condition to maintain turbulent flow. It was inferred that in higher Re condition, MHD turbulence models coupled with k-ε model of turbulence can reproduce the MHD pressure loss trend with increase of Ha.

DNS of turbulent heat transfer under a uniform magnetic field at high Reynolds number for low Pr number fluid was carried out by the Satake et al. [48]. Spectral finite difference methods were used for the simulation in the DNS code. The Reynolds number based on the bulk velocity, viscosity and channel width was set to be constant as 45,818. A uniform magnetic field perpendicular to the wall of the channel was employed. The Hartmann number was taken as 0 and 65, with the Prandtl number as 0.06. The computational grid was taken to be as 1024×1024×768. With DNS, the turbulent quantities such as the mean temperature, turbulent heat flux and temperature variant were obtained. The velocity fluctuations were found to decrease at the channel center whereas temperature variance increased except in the near-wall region, which showed up laminar profile. It was attributed that the heat transfer enhancement at turbulent flow for low Pr fluid cannot be acceptable where the flow state happens to be turbulent flow at high Reynolds number. It was concluded the thermal mixing augmentation is necessary for low Pr number fluid flow in fusion reactor design.

Piller et al [49] performed DNS of the velocity and temperature fields for turbulent flow in a channel to examine the influence of Prandtl number Pr on turbulent transport. The Reynolds number, based on the half-height of the channel and the friction velocity was Re_τ = 150. Prandtl numbers of 1.0, 0.3, 0.1, 0.05, 0.025 were studied. The influence of Pr on Reynolds transport, on the turbulent diffusivity and on the spectral density function of the temperature fluctuations was studied. The spectral density functions of the fluctuating temperature was applied to provide an interpretation of the observed influence of Prandtl number on the eddy diffusivity and on statistical properties of the fluctuating temperature field. A monotonic decrease in turbulent diffusivity was observed with decreasing Pr at all wall coordinate points. It was inferred that the molecular diffusivity acts as a filter by decreasing the effectiveness of large-frequency velocity fluctuations in creating temperature fluctuations which in turn causes the observed decrease in turbulent diffusivity.

Dritsells et al. [45] conducted a numerical study of the effects of magnetic field on the coherent structures and the associated heat transfer in a turbulent channel flow with constant temperature at the bottom (cold) and top (hot) walls. Two fluids with Prandtl numbers of 0.01 and 0.71 were studied with a Reynolds number of 5600 based on the bulk velocity and wall distance. The study aimed to investigate the statistically significant effects of the magnetic field on the coherent structures near the non-conducting walls of a low Reynolds turbulent channel flow with heat transfer. It was found that the conditionally averaged quasi-streamwise vortices were modified by the magnetic field with their size being increased and their strength decreased. The underlying organized fluid motions were found to be damped by the Lorentz force and turbulent heat transfer was decreased by the magnetic field. In case of higher Prandtl number fluid, a similarity between the coherent temperature and the coherent streamwise velocity fluctuations was observed for both types of flow. This was diminished for the lower Prandtl number fluid, especially in the magnetohydrodynamic flow, inhibiting the intrusion of cold (hot) fluid from the cold (hot) wall towards the central region.

Kassinos et al. [46] examined the transport of a passive scalar in homogenous MHD turbulence that underwent shear in a rotating frame. The frame rotation and imposed magnetic field were aligned with the spanwise direction while the mean scalar gradient was in the transverse direction within the plane of the mean shear. It was found that the applied magnetic field has a strong effect on the transport of the passive scalar. Magnetic effects were found to be more pronounced when the time scale of the mean shear is comparable or long compared to the Joule time (τ_{shear}/τ_m) and when the magnetic Reynolds number is relatively low. The most drastic modifications to passive scalar transport were observed when $\tau_{shear} \geq \tau_m$ and these are shown to be linked to changes in the structure of the velocity and scalar fields. It was attributed that the observed evolution of the scalar flux coefficients can be explained in terms of structural information provided by the one-point structure tensors, except for high magnetic Reynolds numbers flows, where the alignment of the velocity fluctuation field with the spatially varying local mean magnetic field can, under

certain conditions, lead to loss of coherence and suppression of the correlation between the velocity and scalar fields.

Based on the literature review, it appears that the effect of magnetic field of any other orientation except wall-normal orientation has never been addressed. The studies of the wall-normal field case were conducted in a wide range of Prandtl and Reynolds numbers, and at the strength of the magnetic field going up to the level of complete laminarization of the flow. It was found that the magnetic field invariably led to suppression of scalar transport across the channel. This was attributed to suppression of fluctuations of the wall-normal velocity component. The transformation of the scalar distribution was described, the main observed effects were the modification of the mean scalar profile characterized by thicker boundary layers and increase of variance of scalar fluctuations in the core flow [48] and enhanced correlation between scalar and velocity fluctuations.

In the proposed doctoral study, the question of the effect of the imposed magnetic field on turbulent scalar transport in a channel has been investigated rigorously. The approach of high resolution DNS is applied to conduct a systematic study. For the first time, the cases of spanwise and streamwise magnetic field are considered together with the classical case of the wall-normal field.

4.3 Results and Discussion

As already discussed in chapter 3, all of the flow properties are obtained for fully developed turbulent flows. For each case, the solution is calculated until the friction coefficient and the Nusselt number become statistically steady. After that, the flow is computed for not less than 1000 time units, which should be compared with the non-dimensional convective time scale $L/U = 1$. The data are collected at this stage. The mean scalar characteristics, mean-square fluctuations of scalar turbulent scalar fluxes, etc are obtained using averaging over time and wall-parallel (x-y) planes. This operation is denoted in the following text as $\langle \quad \rangle$. For example, the mean scalar is:

$$T(z) = \langle \theta(x,\ y,\ z,t) \rangle \tag{4.1}$$

The turbulent fluctuations of scalar is defined as differences between the instantaneous and mean fields:

$$\theta' = \theta - T \tag{4.2}$$

The values of Prandtl number (defined in Chapter 2, equation 2.18) and Schmidt number (dimensionless number defining the ration of momentum to the diffusion of mass in a fluid) in the technological applications vary from values much smaller than one (e.g., Prandtl numbers of liquid metals) to values much larger than one (Schmidt numbers for some admixtures in crystal growth). Since the focus of the study is on the basic features of the effect of the magnetic field rather than on a specific application, Pr = 1 has been used in all the computations.

4.3.1 Mean scalar perturbations and transport

The turbulent scalar flux in the wall direction is defined as $q_t(z)$ as:

$$q_t(z) = \langle w\theta' \rangle \tag{4.3}$$

The Scalar transport equation defined in Chapter 2 is:

$$\frac{\partial \theta}{\partial t} + \boldsymbol{u}.\nabla\theta = \frac{1}{PrRe}\nabla^2\theta \tag{4.4}$$

Applying the averaging $\langle \quad \rangle$ to (4.4), the expression depicting the connection between the turbulent and molecular transports and the Nusselt Number has been obtained as:

$$q_t - \frac{1}{Pr\ Re}\frac{dT}{dz} = \frac{1}{2PrRe}\ Nu \tag{4.5}$$

where Nusselt Number (Nu) is defined as,

$$Nu \equiv 2\frac{dT}{dz}\Big|_{wall} \tag{4.6}$$

In wall units, scaling z by Re_τ^{-1} , replacing T by

$$T^+(z) = \frac{T_w - T(z)}{T^*} \tag{4.7}$$

where the wall friction scalar is defined as

$$T^* \equiv \frac{u_\tau}{PrRe}\frac{dT}{dz}\Big|_{wall} \tag{4.8}$$

and scaling $q_t(z)$ by $u_\tau T^*$, the equation (4.5) is transformed as:

$$q_t^+ + \frac{1}{Pr}\frac{dT^+}{dz^+} = 1 \tag{4.9}$$

Distributions of the mean scalar T and the mean-square perturbations of the scalar $\langle\theta'^2\rangle$ across the channel are shown in figure 4.1.

Considering the curves of T(z), the effect of the magnetic field is observed to be the same qualitatively for all three orientations. The diffusion boundary layer becomes wider and the decrease of mean scalar within it becomes smaller. The effect was earlier reported for the wall-normal magnetic field [34, 45]. It is evident from the current study that it also exists in the cases of spanwise and, to a smaller degree at the same Ha, streamwise field.

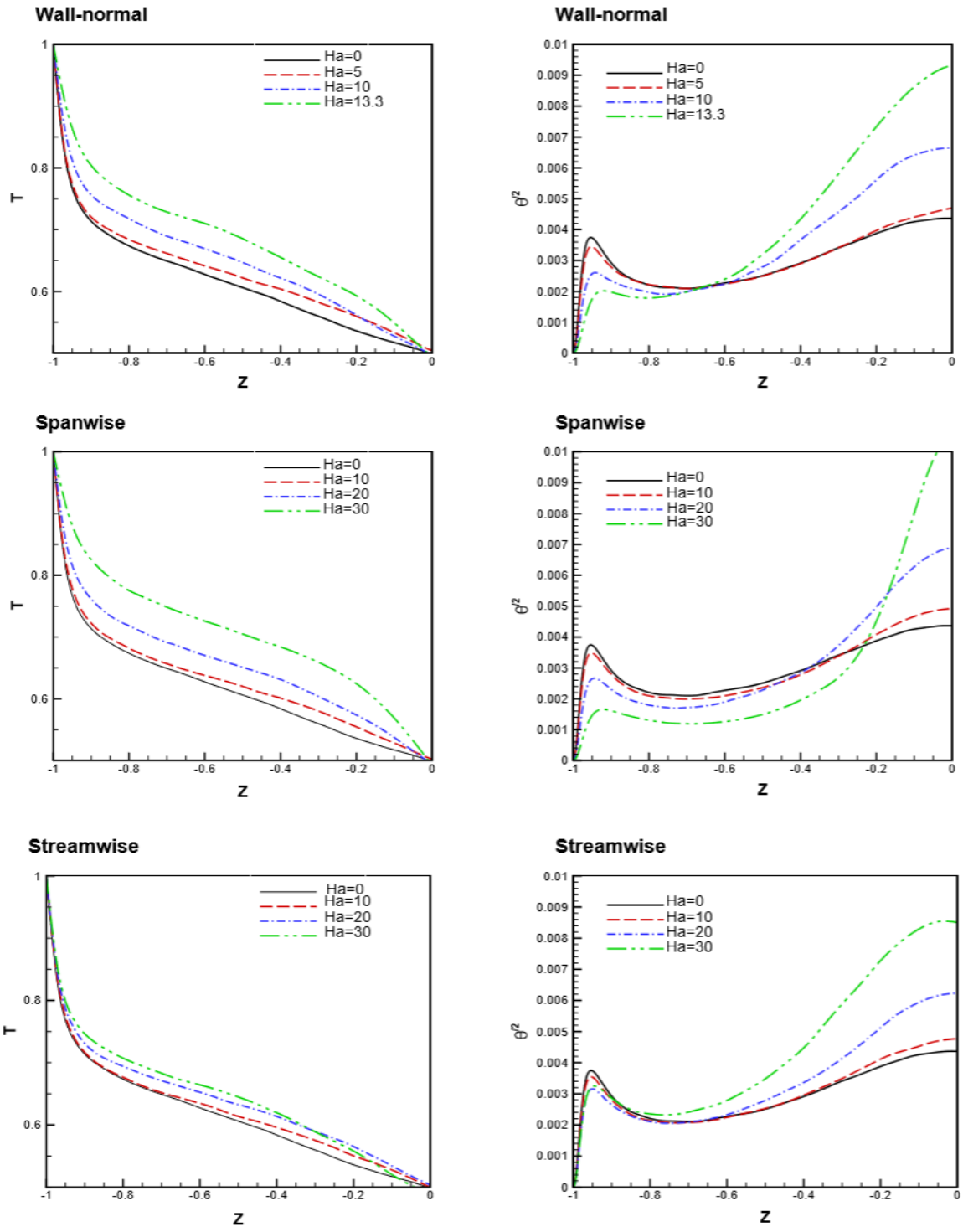

Figure 4.1: Profiles of mean scalar $T(z)$ (left) and of the mean-square perturbations of the scalar $\langle \theta'^2 \rangle$ (right). The orientations of the magnetic field are as indicated above each plot.

Analyzing the profiles of the mean-square perturbations, the perturbations are seen to be suppressed within the boundary layers. The effect is particularly strong in the cases of wall-normal and spanwise magnetic fields. Comparing with the mean-square velocity perturbations shown in figures 3.3 and 3.4 in chapter 3, the transformation of $\langle\theta'^2\rangle$ in this area is observed to be similar to the moderately strong transformation of $\langle u'^2\rangle$ rather than that of $\langle w'^2\rangle$. This will be confirmed by the further results from the current study that show strong correlation between the perturbations of scalar and streamwise velocity near the walls.

In the middle of the channel, the variance of the scalar increases in amplitude (figure 4.1). This has been reported in earlier studies for the case of the wall-normal magnetic field [50]. Similar transformation occurring in the cases of spanwise and streamwise fields has been observed. To explain the mechanism behind this observation, the balance equation determining the distribution of scalar variance across the channel is considered:

$$\frac{1}{PrRe}\frac{d^2\langle\theta'^2\rangle}{dz^2} = \frac{d\langle w\theta'^2\rangle}{dz} - \prod + 2\epsilon_\theta \tag{4.10}$$

The term in the left-hand side and the first term in the right-hand side represent the transport of the variance by molecular and turbulent diffusivities. The second term in the right-hand side is the variance production expressed as

$$\prod = -2\langle w\theta'\rangle\frac{dT}{dz} \tag{4.11}$$

and the last term ε_θ is the rate of scalar diffusion.

Directly evaluating the terms of (4.9) for the flow without magnetic field, (4.9) showed that the last two terms were dominant and nearly canceling each other outside the boundary

layers. The data obtained through the DNS of the proposed doctoral research enables evaluation of the production term (4.11). The results are shown in figure 4.2.

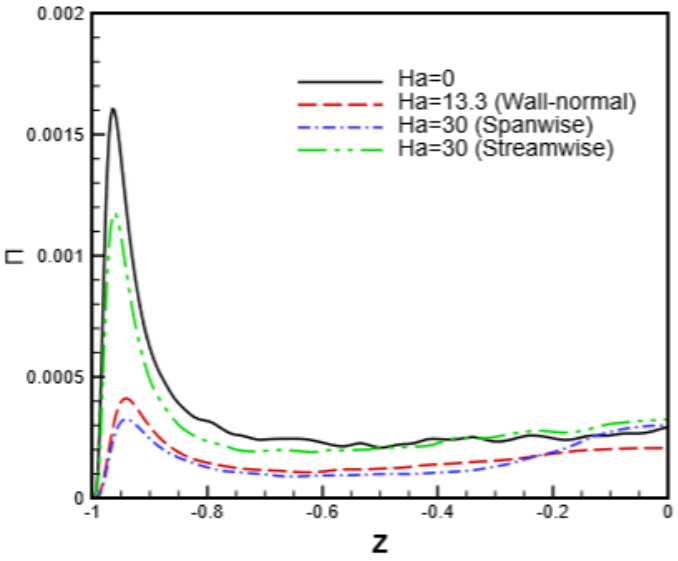

Figure 4.2: Production term (4.8) in the scalar variance equation (4.7)

It can be seen that the imposed magnetic fields of all three orientations suppress the production. According to (4.7), this may lead to larger positive curvature $d^2\langle\theta'^2\rangle/dz^2$ of the curve $\langle\theta'^2\rangle$ (z) . One can, therefore, expect faster growth of $\langle\theta'^2\rangle$ toward the middle of the channel which is observed in figure 4.1.

The mean scalar profiles have also been plotted in wall units, i.e. as $T^+(z^+)$. The plots for the highest Ha for each magnetic field orientation are shown in figure 4.3. Simulations of the scalar transport in a channel without magnetic field (see, e.g., [51, 52]) showed that, at sufficiently large Re, the profiles exhibited log-layer behavior, although not as well-defined as for the profiles of mean velocity. In order to evaluate the behavior in the cases with magnetic fields, we have computed the reciprocal von Karman constant.

$$\gamma = z^+ \frac{dT^+}{dz^+} \tag{4.12}$$

The coefficient is shown in figure 4.3. It is evident that, in agreement with earlier results, nearly log-layer behavior is observed in the hydrodynamic case at z^+ between approximately 40 and 150. The situation is changed by the magnetic fields of all three orientations. The intervals of z^+, where an approximately log-layer behavior can be claimed, become somewhat smaller. It is also observed that the reciprocal von Karman constant γ is substantially increased in the presence of wall-normal and spanwise, but not streamwise magnetic field.

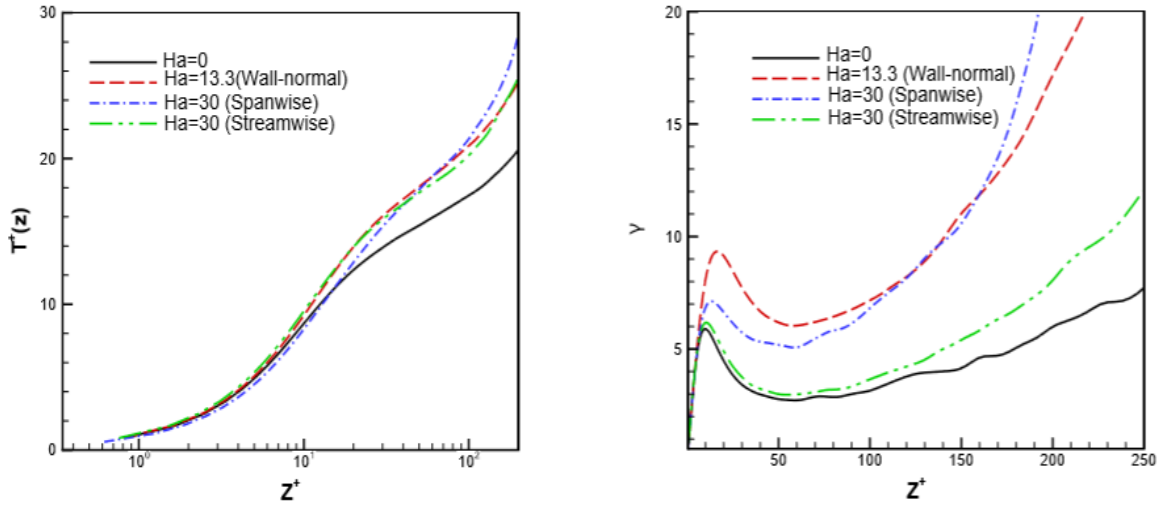

Figure 4.3: Mean scalar profiles in wall units (left) and the coefficient computed according to (4.12) (right).

One can also hypothesize that the increase of scalar variance in the middle of the channel is related to development of large-scale turbulent coherent structures in the presence of the magnetic field (see, e.g. [25, 35]). The phenomenon deserves further analysis, in which the physical nature of the effect is fully revealed. It would also be interesting to explore the evolution of the scalar variance at higher Hartman numbers when the flow approaches he laminarized state. These questions will be left for future studies and not considered in the dissertation.

4.3.2 Turbulent Scalar Flux

Profiles of the mean turbulent scalar flux in the wall-normal direction $q_t(z)$ are shown in the left-hand side column of figure 4.4. It is observed that the magnetic field invariably suppresses the transport. The effect is very strong in the cases of wall-normal and spanwise magnetic fields. It is, at the same Ha, weaker, but still noticeable in the case of the streamwise field. The possible mechanisms of reduction of q_t can be, in a formal way, categorized into three groups: those leading to reduction of w, those leading to reduction of θ', and those leading to reduced correlation between θ' and w. Figure 3.3 in Chapter 3 unambiguously demonstrates that the magnetic fields of all the three orientations are effective mechanisms of the first group. As shown in figure 4.1, they also act as mechanisms of the second group, although the effect is much weaker and, in the cases of wall-normal and streamwise magnetic fields, limited to the boundary layers. The amplitude of scalar perturbations in the middle of the channel is, in fact, increased by the magnetic fields. In order to determine, whether the loss of correlation plays a role, variation of correlation coefficients defined by equation (4.12) are shown in figure 4.4.

$$R_{w\theta}(z) = \frac{q_t}{\langle w^2 \rangle^{1/2} \langle \theta'^2 \rangle^{1/2}} \tag{4.13}$$

One can see that the correlation is affected only weakly by the wall-normal magnetic field. Observing this in combination with the distributions of figure 4.1, it is concluded that the suppression of the turbulent transport in this case is primarily due to the reduction of amplitude of velocity fluctuations. In the case of the spanwise field, loss of correlation is noticeable and increasing with Ha, but its magnitude is only so big as to account for a fraction of the observed (nearly three-fold at Ha = 30) reduction of q_t. The main factor remains the suppression of wall-normal velocity fluctuations shown in figure 3.3. In the case of the streamwise magnetic field, the role of the loss of correlation is more significant than in the other two cases. This conclusion is based on the observation that the reduction

of q_t is more modest, while the loss of correlation is comparable with that in the spanwise field case.

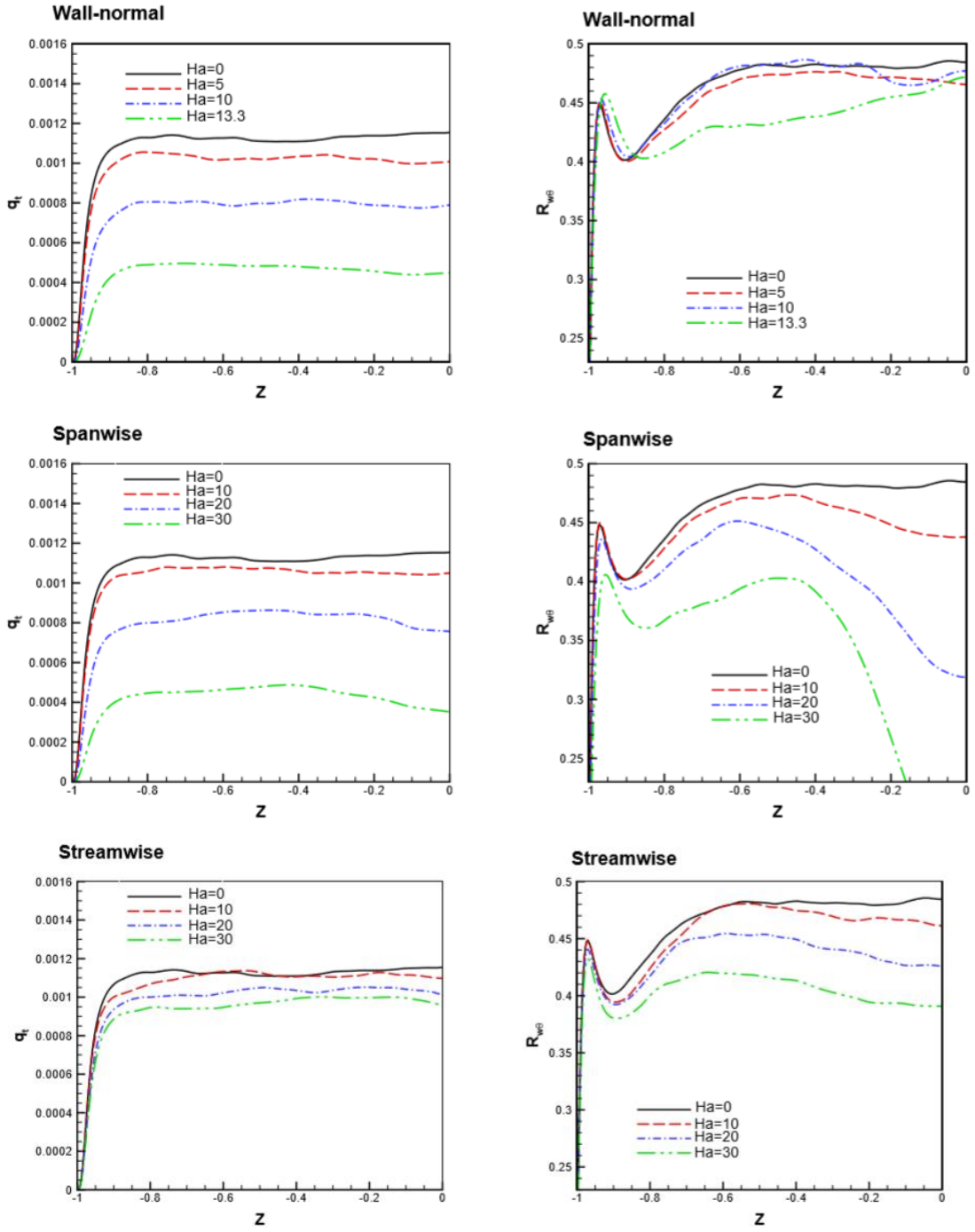

Figure 4.4: Profiles of turbulent scalar flux (4.3) (left) and of the correlation coefficient (4.12) (right). The orientations of the magnetic field are as indicated above each plot.

4.3.3 Integral scalar transport across the channel

The key contribution of the proposed doctoral study is highlighted in this section which outlines the integral scalar transport across the channel and develops a correlation for the scalar transport in terms of magnetic interaction parameter.

The reduction of $q_t(z)$ as presented in the preceding section by the magnetic field results in decreasing the integral scalar transport across the channel. This can be seen in the values of Nu listed in Table 4.1. As an additional illustration, figure 4.5 shows Nu − 1 as a function of N. It can be observed that in the case of the spanwise field, the function is nearly linear:

$$Nu - 1 = (Nu - 1)_{Ha=0} - CN \tag{4.14}$$

Table 4.2

Ha, N	**Nu**	**[α_t] x10^{-3}**	**[Pr_t]**
Ha = 0, 0	13.72	5.009	0.7392
Wall-normal			
5, 0.00417	12.85	4.341	0.7632
10, 0.0167	10.13	2.934	0.8118
13.3, 0.0295	6.83	1.475	0.9351
Spanwise			
10, 0.0167	12.97	4.501	0.714
20, 0.0667	10.26	3.112	0.680
30, 0.150	6.04	1.537	0.693
Streamwise			
10, 0.00417	13.45	4.702	0.792
20, 0.0667	12.52	4.049	0.931
30, 0.150	11.56	3.686	0.957

Table 4.2: Computed integral characteristics. *Nu* – Nusselt number (4.11), [α_t], and [Pr_t]– volume-averaged diffusivity (37), and Prandtl number (39)

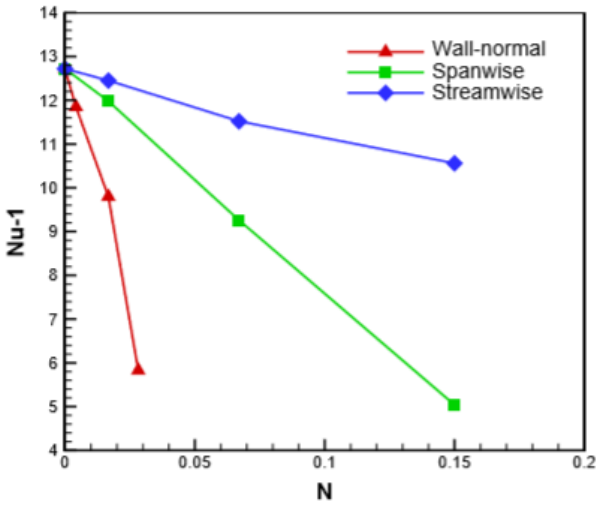

Figure 4.5: Nusselt number *Nu* in excess of 1 as a function of the magnetic interaction parameter *N* for different orientations of the magnetic field

Similar linear approximations can be applied, although with lower accuracy, to the cases of streamwise and wall-normal fields. It has been used to quantify the suppression of the scalar transport by a single coefficient - the slope C.

Using linear fitting, the slope C has been obtained as:

C = −236.4 in the case of the wall-normal field

C = −51.6 in the case of spanwise field

C = −14.5 in the case of streamwise field.

4.3.4 Correlation coefficient

Figure 4.6 shows the average scalar flux in the streamwise direction

$$q_{u\theta}(z) = \langle u'\theta \rangle \tag{4.15}$$

and the corresponding correlation coefficient

$$R_{u\theta}(z) = \frac{q_{u\theta}}{\langle u'^2 \rangle^{1/2} \langle \theta'^2 \rangle^{1/2}} \tag{4.16}$$

Although not contributing directly into the scalar transport between the channel walls in the conditions of a fully developed flow (see (25)), $q_{u\theta}$ is interesting in the general context of turbulent scalar transport in the presence of mean shear and magnetic field. It can be observed in figure that, locally, the streamwise flux is much stronger than the wall-normal flux q_t shown in figure 4.6, especially near the channel wall. This can be explained by the presence of strong negative correlation between θ' and u', which is seen in the right plot of figure 4.6, and the significant strength of perturbations in the form of high-speed and low-speed streaks. The sign of the correlation can be easily explained if we consider the role of the wall-normal velocity. For example, near the wall z = -1, positive $\boldsymbol{w}$ transports higher values of θ and lower values of u from the wall, resulting in formation of a zone with low-speed streak) and Similarly, negative w transports lower values of and higher values of from the channel core resulting in formation of a zone with $u' < 0$ (a low-speed streak) and $\theta' > 0$. Similarly, negative w transports lower values of θ and higher values of u from the channel core resulting in a zone with $u' > 0$ (a high-speed streak) and $\theta' < 0$. The result is the negative correlation between θ' and u', which is strong due to the dominance of u' in the flow field. At the opposite wall $z = 1$, similar reasoning requires profiles with positive $q_{u\theta}$ and $R_{u\theta}$, antisymmetric to those shown in figure 4.6.

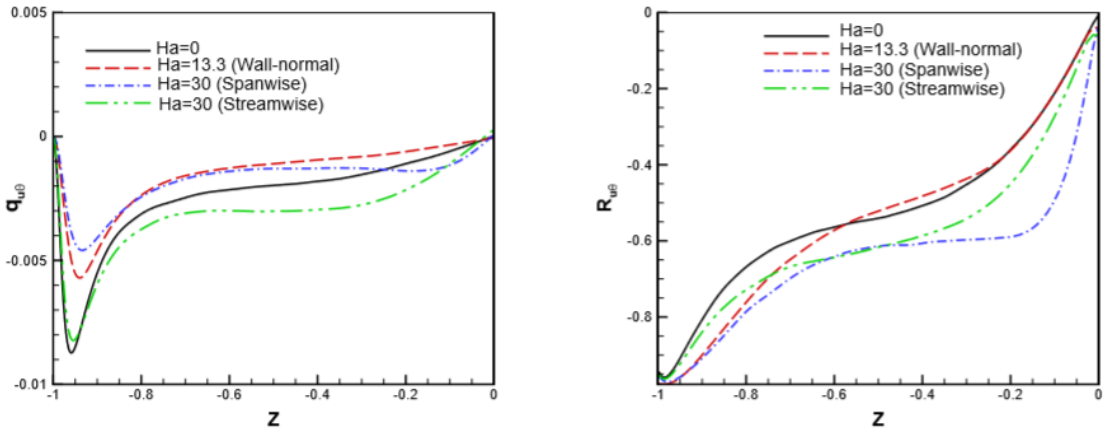

Figure 4.6: Profiles of turbulent scalar flux in the streamwise direction (4.13) (left) and correlations coefficients (4.14) (right).

4.3.5 Eddy Diffusivity

As similar to the eddy viscosity (3.6), the eddy diffusivity of the turbulent scalar transport in the wall-normal direction has been computed as:

$$\alpha_t(z) = -\frac{q_t}{dT/dz} \tag{4.17}$$

The results are presented in figure 4.7. The figure also shows the eddy diffusivity integrated over the volume of the core flow:

$$[\alpha_t] = \frac{1}{1.8}\int_{-0.9}^{0.9} \alpha_t(z)dz \tag{4.18}$$

The limits of integration are chosen as for the eddy viscosity in (3.6). i.e. excluding the . the contribution of boundary layers. The values of eddy diffusivity $[\alpha_t]$ are shown in Table 4.1.

It can be seen that the suppression of the turbulent scalar transport by the magnetic field consistently leads to reduction of eddy diffusivity. The general tendency is the same as for the eddy viscosity shown in figure 4.7, although there are differences. In order to quantify them and to provide information for future attempts of turbulence modeling, the turbulent Prandtl number as a function of the wall-normal coordinate has been computed as follows:

$$Pr_t(\mathrm{z}) = \frac{\nu_t(\mathrm{z})}{\alpha_t(\mathrm{z})} \tag{4.19}$$

and using the volume-averaged quantities

$$[Pr_t\,(z)] = \frac{[\nu_t(z)]}{[\alpha_t(z)]} \tag{4.20}$$

the values of which are listed in Table 4.1. The results are shown in figure 4.8. For the hydrodynamic case, in agreement with the results of earlier DNS [53], Pr_t is about one near the walls and decreases significantly towards the middle of the channel. For the flows with magnetic fields, the near-wall behavior is approximately the same, but the transformation of turbulence in the core flow acts differently on the eddy viscosity and eddy diffusivity. The effect varies depending on the orientation of the magnetic field. In the wall-normal case, it can be described as an increase of the Prandtl number, which is small at $Ha \leq 10$ but becomes significantly larger at Ha=13.3, i.e. close to the laminarization threshold. In the case of the spanwise field, we see a decrease of except in the very middle of the channel, where it increases. The suppression of turbulent fluctuations and growth of their typical length scale leads to a somewhat stronger reduction of eddy viscosity than of eddy diffusivity.

A comparably strong, but opposite tendency is observed when the magnetic field is in the streamwise direction. The turbulent Prandtl number increases with the strength of the magnetic field.

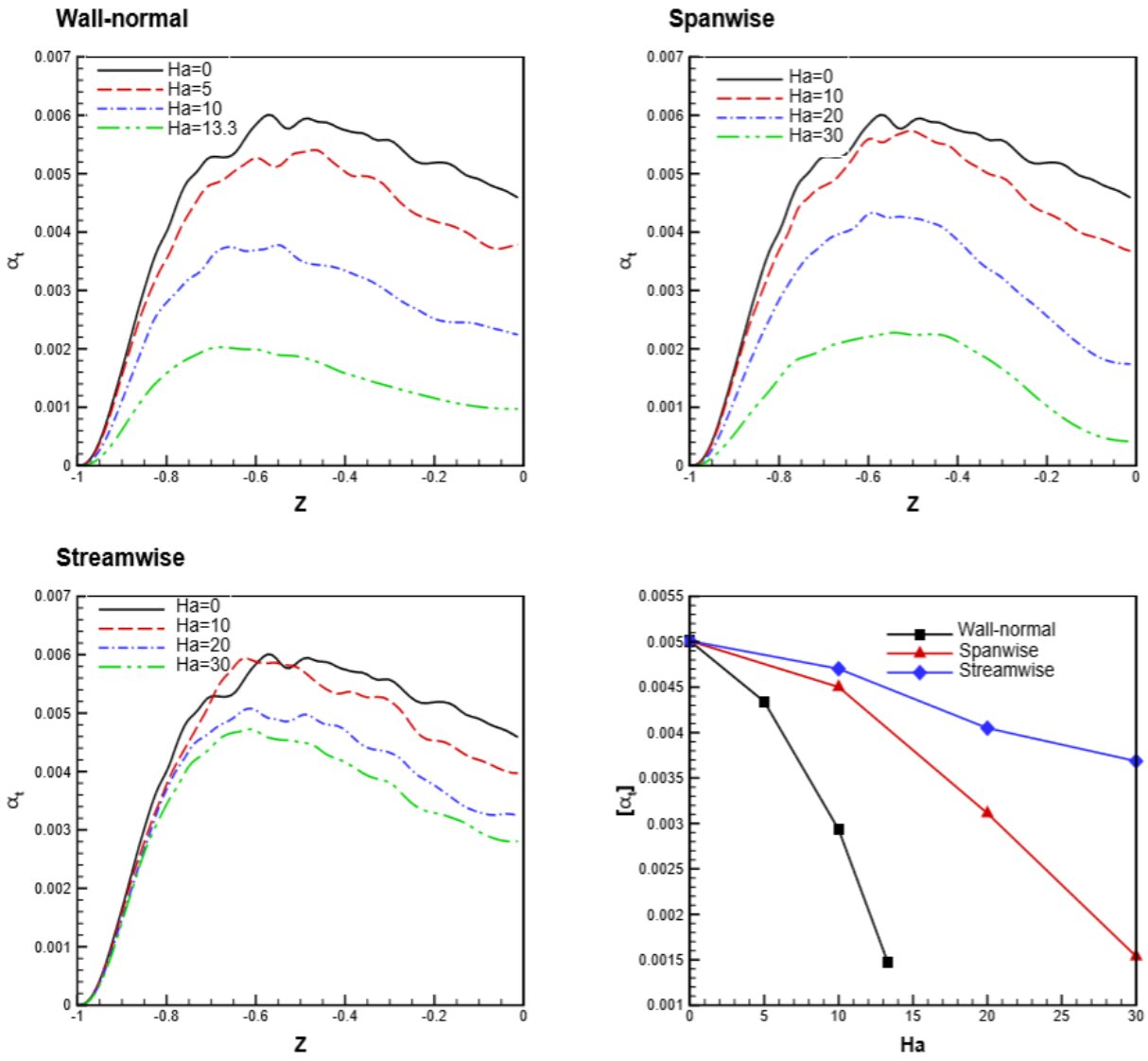

Figure 4.7: Turbulent eddy diffusivity as a function of wall-normal coordinate. The last plot shows the volume-averaged diffusivity (4.18).

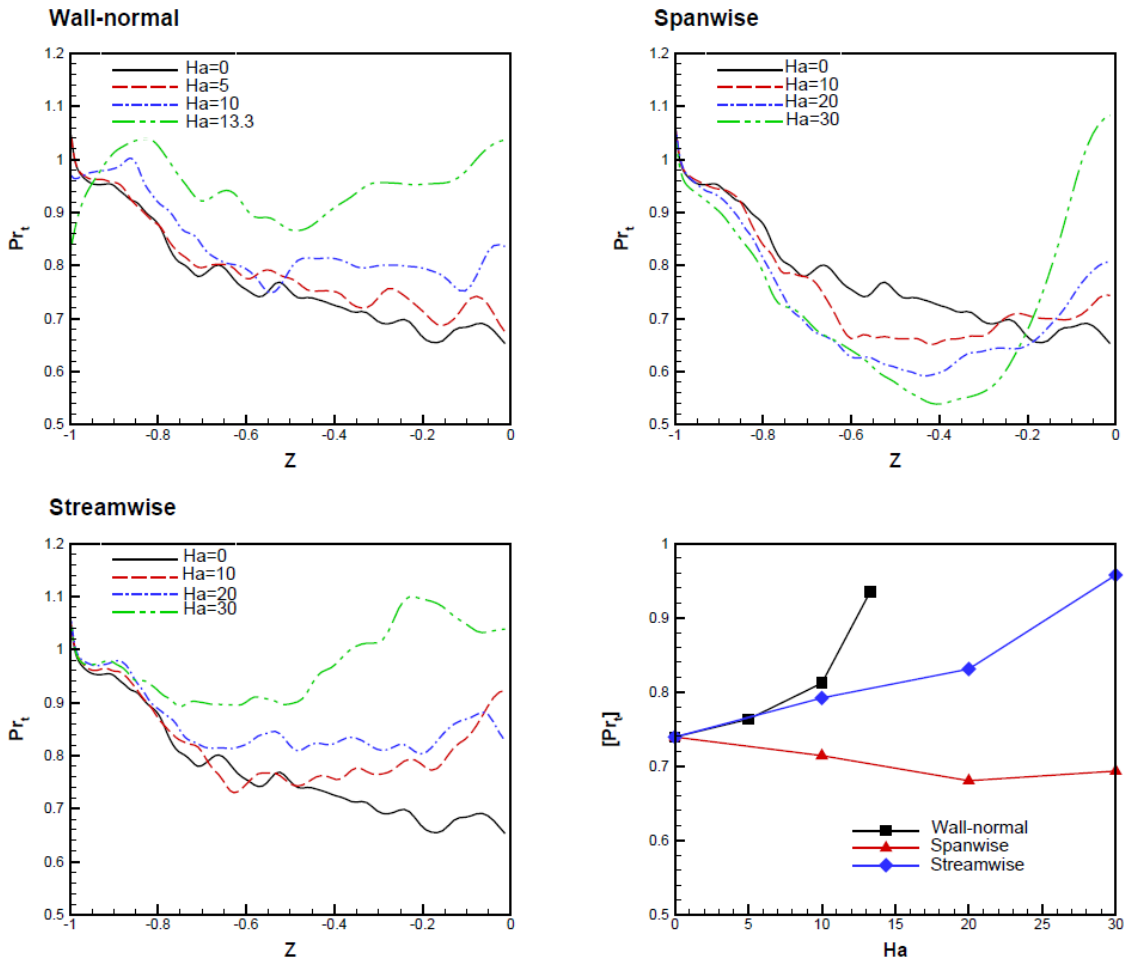

Figure 4.8: Turbulent Prandtl number as a function of wall-normal coordinate. The last plot shows the volume-averaged number (4.20).

4.3.6 Computed scalar structure

The structure of the computed scalar fields is illustrated in figures 4.9–4.11. Instantaneous distributions of θ are shown in three cross-sections: parallel to the wall within the boundary layer (figure 4.9) and perpendicular to the wall along the spanwise y-axis (figure 4.10) and along the streamwise x-axis (figure 4.11). For every cross-section, solutions at the highest Ha for each orientation of the magnetic field are presented.

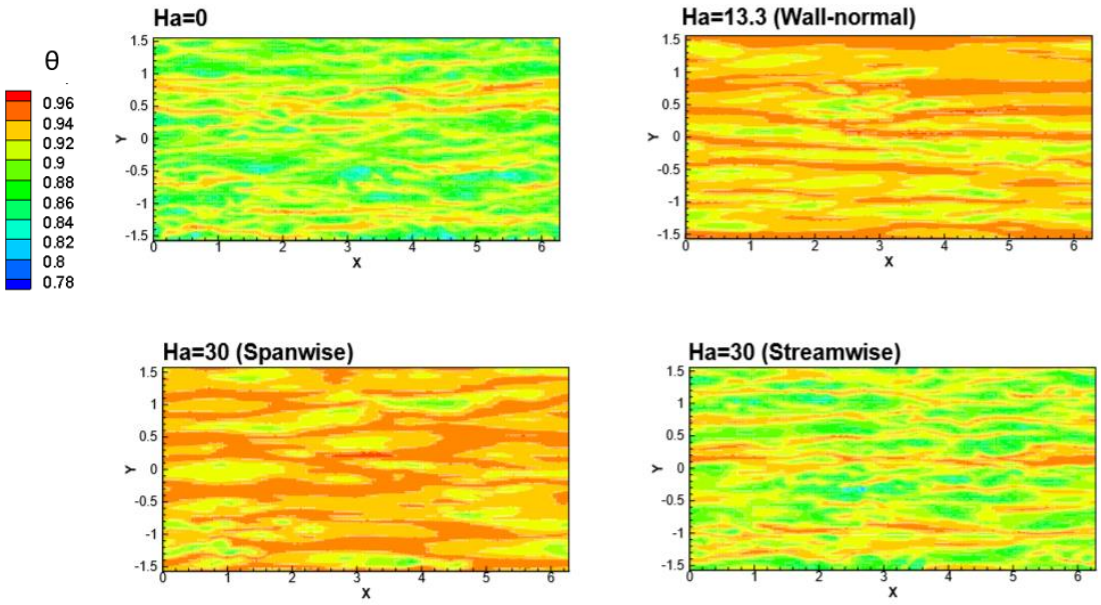

Figure 4.9: Instantaneous distribution of scalar at $z = 0{:}979$.

The scalar distribution within the boundary layers, which is illustrated in figure 4.8, can be interpreted on the basis of strong correlation between the scalar and the fluctuations of the streamwise velocity (see figure 4.6). At such a strong correlation, the scalar field closely follows the pattern of high-speed and low-speed streaks. The conclusions in regard of the effect of the magnetic field on the streamwise velocity made in the present study and in the earlier studies, such as [20, 21, 23, 25, 41], can be directly applied to the scalar. This is confirmed by our results shown in figure 4.8. The scalar 'streaks' increase in size and coherence in the presence of the wall-normal magnetic field at Ha=13.3 (close to the laminarization threshold). The spanwise field also increases the typical size of the 'streaks'. Both wall-normal and spanwise magnetic fields reduce the variance of θ', which is already shown in figure 4.1. The effect of the streamwise magnetic field is weaker. Figures 4.9 and 4.10 provide a view of the transformation of the scalar field in the core flow.

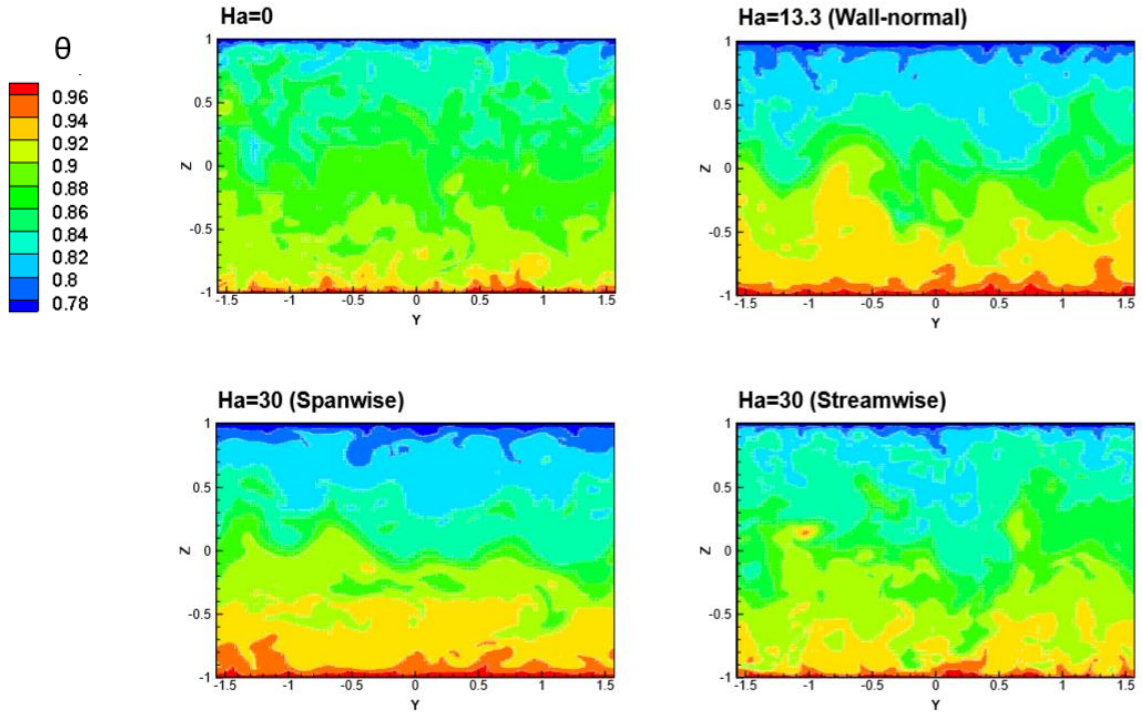

Figure 4.10: Instantaneous distribution of scalar at $x = 0$.

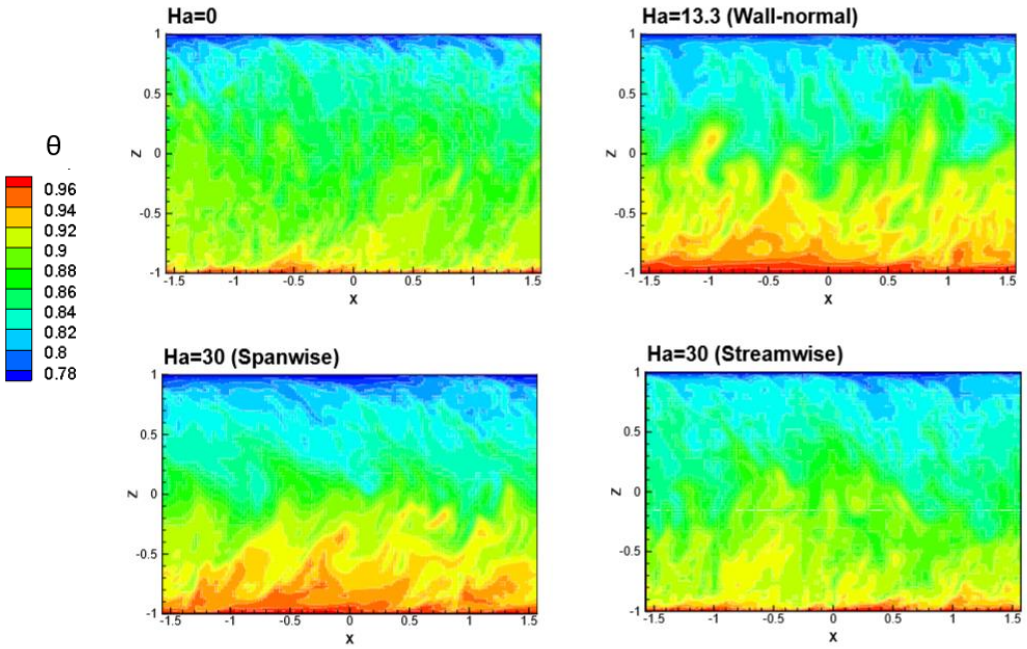

Figure 4.11: Instantaneous distribution of scalar at $y = 0$.

It has been observed that the transformation is only noticeable in the cases of wall-normal and spanwise magnetic fields. In both cases, the core flow area shrinks as the boundary layers become thicker (see figure 4.1). Furthermore, similarly to the velocity components, the scalar distribution is characterized by larger length scales than in the flow without magnetic field.

4.3.7 Scalar Structure Anisotropy

The last characteristic of the scalar field explored in the current study is the structure anisotropy. Similarly to velocity (eqn (3.8) in Chapter-3), the anisotropy is measured by the coefficient

$$F_{ij} \equiv \frac{\langle(\partial\theta/\partial x_i)^2\rangle}{\langle(\partial\theta/\partial x_j)^2\rangle}\,, i \neq j \tag{4.21}$$

F_{ij} = 1 corresponds to a perfectly isotropic scalar field, in which the integral length scales in the directions of are the same. F_{ij} = 0 means a perfectly two-dimensional distribution, in which does not vary along the coordinate. The results of the computations are shown in figure 4.11. Anisotropy in the (x-z)-plane (left plot) and (y-z)-plane (right plot) is presented. Comparing the scalar anisotropy coefficients with the velocity anisotropy coefficients shown in figure 3.9, strong similarities especially with the anisotropy of the streamwise velocity are found per figure 4.11.

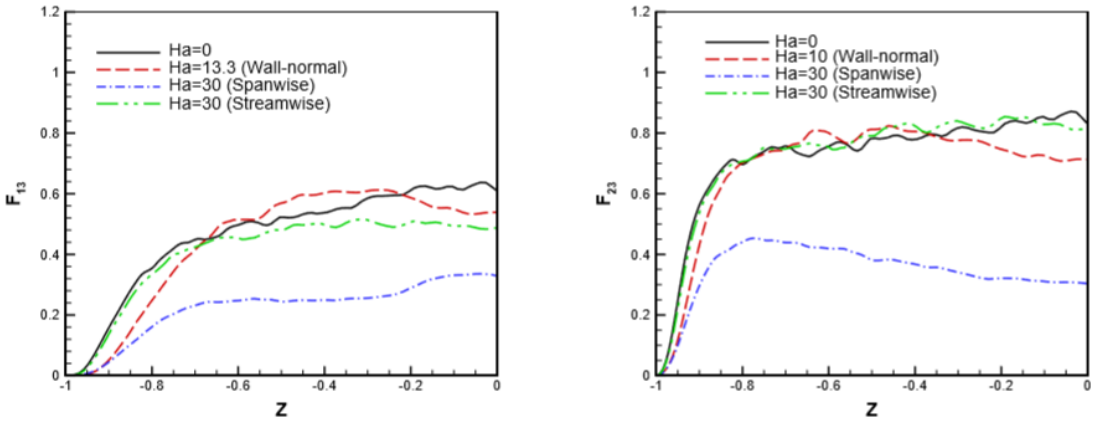

Figure 4.12: Scalar anisotropy coefficients *F*13 (left) and *F*23 (see (4.19)).

Near the walls, where θ' is in almost perfect anti-correlation with u', strong wall-normal derivatives results in very small F_{13} and F_{23}. In the core flow area, the scalar distribution becomes more isotropic, although the coefficients never reach 1.0, i.e., the integral length scales in the streamwise and spanwise directions remain larger than the wall-normal scale. The only significant effect of the magnetic field on the scalar anisotropy is in the case of the spanwise field (see figure 4.11). The spanwise field is known to increase the typical spanwise and streamwise length scales of velocity (ref [13] and figure 3.9 in Chapter 3). The same effect for the velocity and the corresponding decrease of the anisotropy coefficients for the scalar has been observed in the current study.

4.4 Conclusion

The main results of the presented work concern the effect of the magnetic field on the scalar distribution and the rate the turbulent scalar transport across the channel. In the range of the Hartmann numbers considered, the effect is found to be strong in the cases of wall-normal and spanwise magnetic field, but less so in the case of streamwise field. The turbulent scalar flux is substantially reduced (see figure 4.4) due to the suppression of wall-normal velocity fluctuations and some loss of correlation between the scalar and the wall-normal velocity. This results in reduction of the Nusselt number. As illustrated in figure 4.5, for all three orientations of the magnetic field, the decrease of $Nu - 1$ is rather accurately approximated by linear functions of the magnetic interaction parameter N.

It is interesting that the transformation of the mean scalar profiles in figure 4.1 is qualitatively similar to the transformation observed in the hydrodynamic case at decreasing Pr [49, 52]. Both the transformations are caused by suppression of the wall-normal turbulent transport of the scalar. The mechanisms of suppression are, however, different. In the low-Pr flows, high molecular diffusivity acts as a 'filter' preventing the formation of scalar fluctuations with short wavelengths, thus removing the short-wavelength component of the transport. In the MHD case, as it has been demonstrated through current

study, the mechanism is that of suppression of the wall-normal velocity fluctuations and reduction of velocity-scalar correlation by the magnetic field.

CHAPTER V

SCALAR TRANSPORT AND PERTURBATION DYNAMICS IN INTERMITTENT MHD FOW

5.0 Introduction

The influence of magnetic field on turbulent flow and scalar transport characteristics of electrically conducting fluid have been discussed in Chapter 3 and 4 which highlights main features of the flow such as, turbulence suppression, development of Hartmann Boundary Layer and anisotropy, degradation of scalar transport etc. Apart from the features discussed so far, there exists a unique flow regime in electrically conducting fluid especially liquid metal for the case of spanwise magnetic field which was first discussed in [15]. Similar regimes exist in all MHD systems without solid walls crossing the magnetic field line [13, 76]. It is characterized by long periods of nearly steady, two-dimensional (2D) flow interrupted by violent three-dimensional bursts. Contrary to the over-simplification that the magnetic field always dumps turbulence and helps to reduce undesired velocity fluctuations, the regime features novel characteristics of the flow where the flow repeats itself in violent transitioning between 2D state where turbulence is fully suppressed, and fully turbulent three-dimensional (3D) states. The new regime which is defined as Large-scale Intermittency [15] occurs in a wide range of parameters (e.g. Harmann number) and have implications for metallurgical and other low-Rm technological flow. A case example is continuous casting of steel described in Chapter 1. During the casting process, the mixing and transport can be increased primarily when the turbulent burst happens due to intermittency. However, when the flow transforms to quasi-2D state due to magnetic damping by the imposed magnetic field, the flow fluctuation and mixing reduced which

results in inhomogeneous casting of steel. Similar phenomena may happen in admixtures transport (e.g. Growth of Crystal described in Chapter [15]).

In the current study, the work in Ref [15] is further comprehended by conducting direct numerical simulation (DNS) to analyze features of the intermittent regime, such as transport of a passive scalar, distribution of perturbation energy between mean flow and fluctuations, and the effect of the strength of the magnetic field which provides sort of book-end on influence of imposed uniform magnetic field on turbulent and scalar transport characteristics in a channel. In this chapter, the results of the scalar transport and perturbation dynamics in intermittent MHD has been discussed. The outcome of the discussed results in this chapter is published in the research article [54].

5.1 Background and review on earlier work

The large-scale intermittency discovered in [15] occurs in a certain range of the magnetic field strength, where the flows experience cycles with long periods of nearly laminar, nearly two-dimensional behavior interrupted by relatively brief turbulent bursts. The key to understanding the large-scale intermittency is the direct effect of the Joule dissipation of induced electric currents on the flow. The dissipation rate is proportional to the square of the velocity derivative in the direction of the magnetic field [1]. The flow structures with large derivatives are suppressed, while the structures uniform along the magnetic field lines do not induce electric currents and, therefore, remain unaffected. The situation becomes more complex in systems with Hartmann walls (walls perpendicular to the magnetic field). In this case, the global distribution of electric potential causes currents and Joule dissipation within the Hartmann boundary layers even when the flow structures in the core are uniform along the magnetic field. In Ref. [15], the large-scale intermittency was demonstrated for the channel flow with spanwise magnetic field, i.e. for the case when the Hartmann walls are absent. The driving mechanism of the intermittency is the classical Tollmien-Schlichting (TS) instability of the laminar channel flow to two-dimensional spanwise rolls. Since these structures are uniform in the direction of the magnetic field, they do not experience suppression due to the Joule dissipation. However, when the rolls

develop to a finite amplitude and give rise to secondary three-dimensional instabilities and, then, to turbulence, strong Joule dissipation appears. It suppresses the turbulence and returns the flow into a state close to the laminar base flow. The process then repeats in cycles of transitions between two unstable attractors: the laminar base flow and the three-dimensional turbulence. Interestingly, the two-dimensional non-laminar solution obtained in the simulations with imposed two-dimensionality [55] or at stronger magnetic fields is never approached by the intermittent flow. The mechanism just described appears to be of general kind, not limited to the specific configuration of the channel flow with spanwise field. It can be hypothesized that the intermittency may develop if two necessary conditions are satisfied: (1) the flow may experience a hydrodynamic instability, whose development is not affected or only weakly affected by the magnetic field, and (2) the magnetic field is not strong enough to prevent development of three-dimensional secondary instabilities, but strong enough to suppress the resulting turbulence.

The validity of the hypothesis is demonstrated by two other examples, in which similar intermittent behaviors are observed: the periodic box turbulence with large-scale forcing [13, 56] and the ideal flow in a tri-axial ellipsoid [57]. In more realistic systems, the first of the two conditions listed above practically limits the possible configurations to those with either infinite or large dimension in the direction of the magnetic field. Still, one can think of numerous situations, including those with large magnetic Reynolds numbers, in which the intermittency is possible. It should be also noted that the scenario just described remains valid if the magnetic field is replaced by another physical mechanism that suppresses three-dimensional perturbations, but allows unimpeded development of a two-dimensional instability. An example is recently provided by simulations of a channel flow with rotation around the spanwise axis [58]. The spanwise rotation suppresses turbulence on one, so-called stable, side of the channel [59, 60]. It does not, however, affect the growth of purely spanwise TS rolls. The resulting flow dynamics obtained in Ref. [58] at the bulk Reynolds numbers between 5000 and 30,000 and sufficiently high rotation rates is remarkably similar to the large-scale intermittency in the MHD channel observed in Ref.

[15]. The flow evolves in cycles, each consisting of growth of TS rolls, their three-dimensional breakdown, and return to the base state. Depending on the magnitude of the rotation rate, the intermittency occurs only on the stable side of the channel, the other side remaining turbulent, or in the entire channel. The time of the process is about 1000 convective time units, which is close to the period observed in Ref. [15] for the MHD channel flow.

From the viewpoint of general hydrodynamics, the large-scale intermittency is a manifestation of transition between laminar and turbulent states. The situation, in which the transition leads to localized, either in space or time, turbulent zones (sometimes called patterned turbulence phenomena [61] is not uncommon. It can be mentioned the turbulent patches in pipe, channel, boundary layer, and other parallel shear flows [61-65] and the striped turbulence in Taylor and plane Couette flows [66-69] that typically takes the form of oblique turbulent stripes and requires large streamwise and spanwise dimensions of the computational domain to be detected in simulations. The common feature of all these flows, also present in our case, is the range of parameters, in which a linear or nonlinear instability mechanism is sufficiently strong to create turbulence, but the turbulence lacks ability of self-sustaining in the entire flow domain or over a long period of time.
In the current study, the intermittency in the case of the channel flow with spanwise magnetic field is further studied. Attention is given to the transport properties of the flow, distribution of the perturbation energy between mean flow and fluctuations, and the effect of the strength of the magnetic field.

5.2 Model for the intermittency study

A fully developed flow of an incompressible electrically conducting fluid in a plane channel is considered in the current study similar to configuration described in Chapter 3 and 4 (please refer to figure 2.1 in Chapter 2 for the channel configuration). The walls are perfectly electrically insulating. The flow is driven by an imposed streamwise pressure gradient maintained so that the total flow rate is constant. A uniform constant magnetic

field of strength $\boldsymbol{B}$ is applied in the spanwise (parallel to the walls and perpendicular to the mean flow) direction. A passive scalar field θ (e.g., temperature or concentration of an admixture) is present in the flow. The magnetic Reynolds and Prandtl numbers are assumed to be much smaller than one, which corresponds to a typical situation in technological or laboratory flows of liquid metals and other electrically conducting fluids. As a result, the induced magnetic field is much smaller than the imposed magnetic field and can be neglected in the Ohm's law and the Lorentz force. The quasistatic approximation described in chapter 2 [1] is valid. The equations in non-dimensional form are

$$\frac{\partial \boldsymbol{u}}{\partial t} + (\boldsymbol{u}.\nabla)\boldsymbol{u} = -\nabla p + \frac{1}{Re}\nabla^{\mathbf{2}}\boldsymbol{u} + \mathbf{N}(\mathbf{j} \times \boldsymbol{e_y}) \tag{5.1}$$

$$\nabla.\boldsymbol{u} = \mathbf{0} \tag{5.2}$$

$$\boldsymbol{j} = -\nabla\boldsymbol{\varphi} + \boldsymbol{u} \times \boldsymbol{e_y} \tag{5.3}$$

$$\nabla^2\varphi = \nabla.(\boldsymbol{u} \times \boldsymbol{e_y}) \tag{5.4}$$

$$\frac{\partial \theta}{\partial t} + \boldsymbol{u}.\nabla\theta = \frac{1}{PrRe}\nabla^2\theta \tag{5.5}$$

where $\boldsymbol{u}$ = (u, v,w), p, θ, $\boldsymbol{j}$, and φ are velocity, pressure, passive scalar, current density, and electric potential fields, respectively. The streamwise, spanwise, and wall-normal coordinates are, correspondingly, x, y, and z. The unit vector $\boldsymbol{e}_y$ represents the direction of the magnetic field.

The boundary conditions in the streamwise and spanwise directions are those of periodic velocity, pressure perturbations, scalar, and electric potential. The channel walls are subject to no slip velocity condition, perfectly electrically insulating, and maintained at constant values of the scalar:

$$u = 0 \; at \; z = \pm 1 \tag{5.6}$$

$$\frac{\partial \emptyset}{\partial n} = 0 \; at \; z = \pm 1 \tag{5.7}$$

$$\theta = 1 \; at \; z = -1, \theta = 0 \; at \; z = 1 \tag{5.8}$$

The typical scales used for non-dimensionalization are the channel half-width L as the length scale, mean velocity U as the velocity scale, L/U as the time scale, ρU^2 as the pressure scale, the strength of the imposed magnetic field B as the magnetic field scale, ULB as the scale of electric potential, σUB as the scale of current density, and the scalar difference between the walls as the scale for the scalar field.

The non-dimensional parameters of the model are the Reynolds number (2.17), Prandtl number (2.18) and either the Hartmann number (2.37) or the magnetic interaction parameter (2.38).

The equations and boundary conditions have the laminar, steady-state "base flow" solution with parabolic velocity profile and purely diffusive scalar transport

$$\boldsymbol{u}_{base} = (3/2)(1 - z^2)e_x, \theta_{base} = (1/2)(1 - z) \tag{5.9}$$

It can be noted that, in addition to being an exact solution for the channel flow with spanwise magnetic field, $\boldsymbol{u}_{\text{base}}$ is an asymptotic limit of the velocity distribution in the core (outside the Hartmann boundary layers) of the flow in a rectangular duct of large aspect ratio with the imposed magnetic field parallel to longer sides. This can be obtained from the expansion series solution [3] of the MHD duct flow or numerically, as in Ref. [70]. According to Ref. [70], in the range of Ha considered in this paper, $\boldsymbol{u}_{\text{base}}$ is a good approximation of the core flow velocity at aspect ratios above 10.

The problem is solved numerically following the DNS approach. The numerical method is based on the second-order finite difference scheme described as the scheme B in Ref. [74], the details of which has been discussed in chapter 2. The method has been extended in Ref. [35] to include the solution of the scalar transport equation (5.5). The scheme utilizes the explicit backward-difference/Adams-Bashfort scheme for time discretization and the standard projection technique to satisfy incompressibility. The spatial discretization is on a spatially non-uniform structured collocated grid. Velocity and current fluxes at half-integer grid points are obtained by interpolation and applied in evaluation of differential operators to ensure that the scheme is nearly fully conservative in regard of the mass, momentum, energy, scalar, and electric charge conservation principles [71, 75]. Further details can be found in Chapter 2 per Ref. [74] as well as in the recent works, where the scheme was applied [35, 72, 73].

The simulations are conducted at the Reynolds number of 5333, which is the same as the Reynolds number used by Ref. [15], where it was presented as 8000 based on the channel half-width and the centerline velocity of the laminar flow. The value is higher than the linear stability limit of the hydrodynamic channel flow Re = 3848. The explored range of the Hartmann number is $30 \leq Ha \leq 160$.

The Prandtl number $Pr = 1$ is chosen for all the computations. As a justification, the current study considers that the values of Prandtl and Schmidt numbers in the technological applications involving liquid metals vary from those much smaller than one (Prandtl number in heat transfer) to those much larger than one (Schmidt number in transport of certain admixtures). Since the current investigation is the first in nature, in which the scalar transport in the presence of large-scale intermittency is considered, the study considers $Pr = 1$ and limit the discussion of the effect of Pr (undoubtedly significant) to the qualitative arguments given in the conclusion of this chapter.

The computational domain has the dimensions of $2\pi \times 4\pi \times 2$ in the streamwise, spanwise, and wall-normal directions, respectively. The computational grid consists of $64 \times 64 \times 80$ points. The points are distributed uniformly in the streamwise and spanwise directions and clustered toward the walls using the coordinate transformation $z = \tanh(A\zeta)/\tanh(A)$ with $A = 1.5$. The grid is similar to the grid used in [15], the differences being that the current study uses finite difference rather than pseudo-spectral discretization and that the number of grid points in the wall-normal direction is slightly larger in the current study (Ref. [15] used 64 Chebyshev functions).

One may argue that the choice of the domain size and numerical resolution in current study is inadequate, because smaller grid steps are needed to fully resolve the small-scale motions during the turbulent bursts and because larger streamwise size of the domain is needed to capture the long-range interaction of the evolving TS rolls. The justification of the current study approach is two-fold. First, as discussed in Ref. [15], the mechanisms and major features of the process are not significantly affected by the small-scale resolution and the domain size. Second, the intermittency has a very large time scale, which requires simulations of flow evolution during tens of thousands of time units. Performing such simulations with a significantly finer grid and in a substantially larger domain would be either computationally unfeasible or feasible in the form of very large-scale massively parallel computations. It is considered unnecessary in the current study and a somewhat inaccurate numerical model is used as a compromise.

5.3 Results and Discussion

One simulation of a flow realization is conducted for every explored value of *Ha*. In each run, the computation started with the developed turbulent flow at $Ha = 30$ and conducted the computations until a pattern of regular cyclic transitions between laminar and turbulent states has been established. After that, the simulation is continued for not less than ten cycles. Flow properties are studied, and time-averaged statistics is accumulated during this period.

5.3.1 Flow evolution and perturbation energy

The current study differs from the procedures followed in Ref. [15] in the numerical method on how flow evolves in intermittency cycle. In the spectral method solution of Ref. [15], random noise of average amplitude 10^{-6} was constantly added to the velocity field thus setting the "floor" of the perturbation energy during the periods of nearly laminar behavior. Noise is not added in the current simulations. It is found that in the finite difference solution, presumably due to the discretization error, the floor has been repeatedly reproduced at some small energy (see figure 5.1). For the purpose of verification, the run at Ha =100 is repeated with the noise added. No significant differences in the results in comparison with the no-noise run has been detected.

The current numerical model has been verified comparing the results obtained at Ha = 80 with those published in [15]. Good agreement is found for the integral characteristics of the process, such as the peak magnitude of the perturbation energy. The lengths of the intermittency cycle are only slightly different. This shows that the addition of weak random noise and the numerical dissipation of the finite difference discretization do not significantly affect the intermittent behavior.

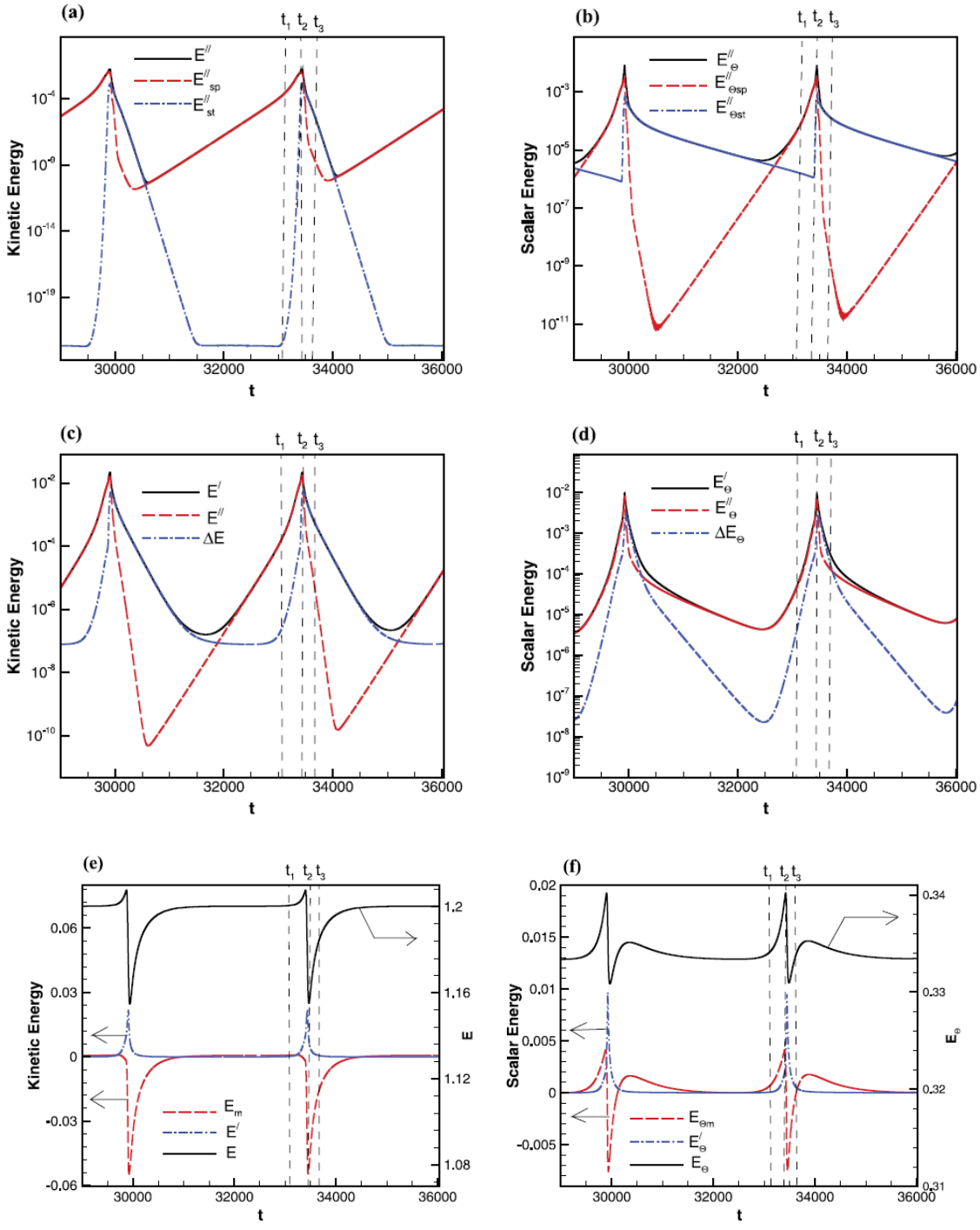

Figure 5.1: Evolution of the kinetic *(a, c, e)* and scalar *(b, d, f)* energies of the perturbations during two cycles of large-scale intermittency at *Ha* = 80.

The large-scale intermittency has been detected in the current study simulations at $40 \leq Ha \leq 140$. At smaller Hartmann numbers, as found from the computations at $Ha = 30$, the flow remained persistently turbulent, although the nature of the turbulence was significantly modified by the spanwise magnetic field in the manner described in earlier publications [35, 25]. At higher *Ha*, the flow becomes purely 2D channel flow [55]. This is found in the current study simulations with $Ha = 160$. For all the intermittent flow regimes, perfectly periodic behavior of the integral characteristics of the flow has been demonstrated from the simulation. In particular, the length of a cycle has been virtually constant, and the peak amplitudes of velocity and scalar perturbations has demonstrated only slight variations. Further in this section, the flow behavior during an intermittency cycle has been analyzed. The analysis is different from Ref. [15] in three aspects. One is that the present study investigates the transport properties of the flow by analyzing the behavior of a passive scalar field. Another is that in the current study the modification of the mean flow during the cycle has been considered. The current study also presents the data illustrating how the characteristics change with the Hartmann number. The flow evolution is described in terms of growth and decay of velocity and scalar perturbations. The perturbations are defined with respect to the base flow (5.9):

$$\boldsymbol{u}' = \boldsymbol{u} - \boldsymbol{u}_{\boldsymbol{base}},\ \theta' = \theta - \theta_{base} \tag{5.10}$$

and, as in Ref. [15], with respect to the instantaneous mean flow:

$$\boldsymbol{u}'' = \boldsymbol{u} - \langle \boldsymbol{u} \rangle,\ \theta'' = \theta - \langle \theta \rangle \tag{5.11}$$

where $\langle \quad \rangle$ is averaging in the $x - y$ plane, and the scalar perturbations θ'' analogous to the velocity perturbations $\boldsymbol{u}''$ computed in Ref. [15] has been introduced in the simulation. The need for the two types of perturbations stems from the intention to consider the evolution of their difference, which is, evidently, the distortion of the mean velocity and scalar:

$$\Delta \boldsymbol{u} \equiv \boldsymbol{u}' - \boldsymbol{u}'' = \langle \boldsymbol{u} \rangle - \boldsymbol{u}_{\boldsymbol{base}},\ \Delta\theta \equiv \theta' - \theta'' = \langle \theta \rangle - \theta_{base} \tag{5.12}$$

The distortion develops during the stages of the flow evolution when the perturbation amplitude is finite. As will be seen in the following, it plays a significant role in the energy balance during an intermittency cycle. In order to quantify the evolution of the flow, kinetic and scalar energies as volume averages of, respectively, square of velocity and scalar have been computed. For example, the total energies are

$$E = V^{-1} \int_V \boldsymbol{u}^2 dV\,, E_\theta = V^{-1} \int_V \theta^2 dV \tag{5.13}$$

In a similar way, the energies E', E'_θ of the perturbations (5.10), energies $E^{"}$, $E^{"}_\theta$ of the perturbations (5.11), and the energies ΔE, ΔE_θ of the distortion of mean velocity and scalar (5.12) have been computed.

It is straightforward to derive the following relations between the energies just introduced:

$$E' = E^{"} + \Delta E,\ E'_\theta = E^{"}_\theta + \Delta E_\theta, \tag{5.14}$$

$$E = E_{base} + E' + E_m,\ E_\theta = E_{\theta base} + E'_\theta + \mathrm{E_{\theta m}} \tag{5.15}$$

In the last formula, E_{base} and $E_{\theta base}$ are the energies of the base flow and scalar distribution (5.9) and

$$E_m = 2V^{-1} \int_V (\boldsymbol{u}_{base}.\Delta\boldsymbol{u}) dV\,,\ E_{\Theta m} = 2V^{-1} \int_V (\theta_{base}\Delta\theta) dV \tag{5.16}$$

are the terms that appear as a result of our decomposition of the mean fields into the base and distortion components. Further understanding of the flow behavior is provided by considering separately the evolution of the velocity and scalar components uniform in the spanwise (y) direction $\boldsymbol{u}_{sp}$, θ_{sp} and the components uniform in the streamwise (x) direction

$\boldsymbol{u}_{str}$, θ_{str}. The components are found by averaging the computed fields in the respective directions. Their energies will be referred to as E'_{sp}, $E'_{\theta sp}$, E'_{str}, $E'_{\theta str}$ if computed for perturbations (5.10) and as $E^{"}_{sp}$, $E^{"}_{\theta sp}$, $E^{"}_{str}$, $E^{"}_{\theta str}$ if computed for perturbations (5.11).

At last, with the purpose of separating the secondary instabilities leading to a turbulent burst from the growth of TS rolls and the mean flow distortion, the energies $\boldsymbol{E_{3D}}$, $\boldsymbol{E_{\theta 3D}}$ of the components of the perturbations (5.10) non-uniform in the spanwise direction and defined as $\boldsymbol{u'_{3D}} = \boldsymbol{u'} - \boldsymbol{u'_{sp}}, \theta'_{3D} = \theta' - \theta'_{sp}$

5.3.2 Velocity during an intermittency cycle

The typical intermittent behavior is illustrated in Fig. 5.1 that presents the results obtained at H*a* = 80. Only two of the ten cycles computed during the stage of a fully developed flow are shown. Figure 5.1(a) shows the kinetic energy of the velocity perturbations (5.15) defined, as in Ref. [15], with respect to the instantaneous mean flow. As it can be observed that a cycle can be divided into three stages indicated in Fig. 5.1 by the typical time moments t_1, t_2, t_3. The velocity perturbations $\boldsymbol{u}^{"}$ during each of these moments are illustrated in Fig. 5.2. During the first stage, to which can be referred to as the "growth stage", the velocity field is nearly perfectly spanwise-independent ($E' \approx E^{"}_{sp}$ as can be seen in Fig. 5.1(a)). Its energy grows due to the amplification of unstable Tollmien-Schlichting (TS) rolls (see Fig. 5.2(a)), which are uniform in the spanwise direction and, thus, not affected by the magnetic field.

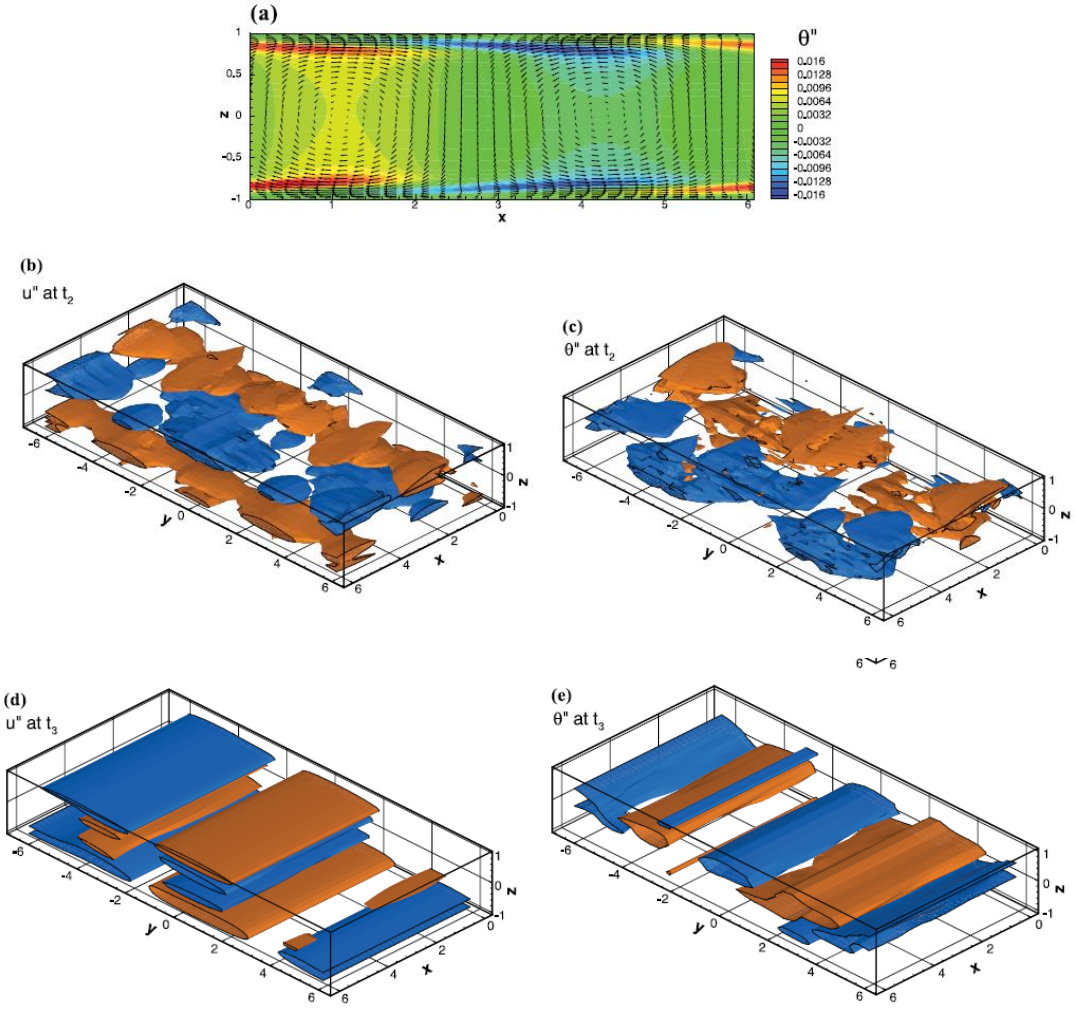

Figure 5.2: Evolution of perturbation velocity $\boldsymbol{u}$" and scalar θ" during one cycle at Ha = 80. (a) Velocity vectors and scalar distribution in a cross-section $y = const$ at $t = t_1$ during the growth stage (see Fig. 5.1) when velocity and scalar perturbations are nearly purely spanwise-independent. (b) and (c): Isosurfaces of u" and θ" at $t = t_2$ during the turbulent burst. For u", the range is [−0.47, 0.35], the isosurfaces at u" = − 0.15, and 0.15 are shown. For θ", the range is [−0.25, 0.26], the isosurfaces at θ" =−0.09, and 0.09 are shown. (d) and (e): Isosurfaces of u" and θ" at $t = t3$ during the decay stage. For u", the range is [−0.023, 0.038], the isosurfaces at u" =−0.01, and 0.01 are shown. For θ", the range is [−0.059, 0.059], the isosurfaces at θ" =−0.02, and 0.02 are shown.

The second stage, which can be called a "burst," starts when the TS rolls experience secondary instability leading to turbulence (see Fig. 5.2(b)). This transfers the energy into 3D velocity fluctuations. As demonstrated in [15], this causes Joule dissipation, which is

sufficiently strong to suppress the turbulence and initiate the third stage, namely the stage of "decay." As demonstrated in [15], the decay of 3D kinetic energy is primarily due to the direct suppression by the Joule dissipation, while the decay of $E_{sp}^{"}$ is, apparently, due to the viscous dissipation and transfer of energy into 3D perturbations. As can be seen in Fig. 5.1(a), the perturbation energy at this stage is almost entirely in streamwise-independent velocity. It is illustrated in Fig. 5.2(d) and discussed in Ref. [15] that, at this stage, the perturbations $\boldsymbol{u}^{"}$ are dominated by streamwise streaks.

Figure 5.1(c) shows the terms of the decomposition (5.14) of the perturbation kinetic energy. It can be observed that, during the growth stage, the perturbations $\boldsymbol{u}'$ measured with respect to the base state are nearly identical to the perturbations $\boldsymbol{u}^{"}$ with respect to the instantaneous mean flow. The mean flow distortion has the energy ΔE several orders of magnitude smaller than $E' \approx E^{"}$. ΔE starts to grow rapidly when the TS rolls reach high amplitude and becomes of the same order of magnitude as E' and $E^{"}$ during the turbulent burst. After the burst, $E^{"}$ decreases much faster than E' and ΔE and soon becomes negligibly small. During the decay stage, $E' \approx \Delta E$, i.e., the perturbations are almost entirely in the form of the distortion of mean flow. The streamwise streaks identified in [15] and illustrated in Fig. 5.2(d) dominate the velocity deviation from the instantaneous mean, but are, in fact, negligible in comparison with the simultaneous distortion of the mean velocity profile. The persistence of the mean flow distortion during the decay phase is easy to explain. Being spanwise-uniform, this component is not affected by the Joule dissipation, while its large typical length scale results in weak viscous dissipation.

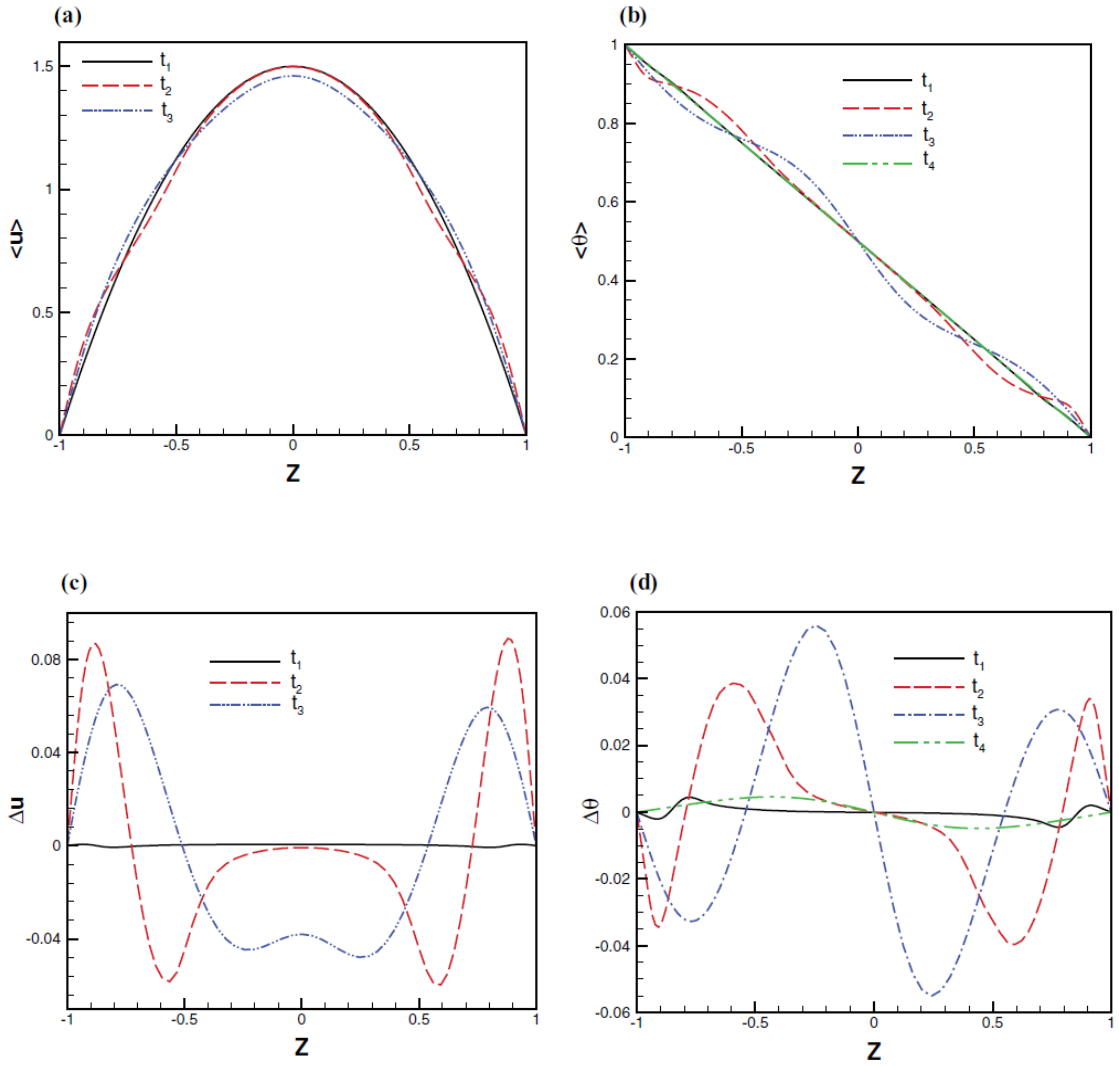

Figure 5.3: Profiles of mean velocity $\langle u \rangle$ and scalar $\langle \theta \rangle$ and their deviations Δu, $\Delta \theta$ from the base flow (5.9). The profiles are shown at Ha = 80 for the typical time moments during the stages of 2D growth (t_1), turbulent burst (t_2), and decay (t_3) (see Fig. 5.1). The scalar profiles are also shown for the time moment t_4 typifying the stage of "sub-diffusive" scalar transport (see Fig. 5.6).

The profiles of instantaneous mean velocity $\langle u \rangle(z, t)$ and its distortion Δu at the typical time moments t_1, t_2, and t_3 are shown in Fig. 5.3. Significant distortion has been observed during the turbulent burst at $t = t_2$ and almost as strong in the decay phase at $t = t_3$.

The global balance of kinetic energy has been obtained through the computations per (5.15). A peculiar feature of the balance is the behavior of the total kinetic energy E with respect to the base flow level E_{base} = 1.2. During the growth stage, increase of the perturbation energy E' leads to increase of E well above E_{base}. The relation changes during the turbulent stage. The total energy E drops rapidly and becomes noticeably smaller than E_{base}. It remains smaller well into the decay stage. This seemingly paradoxical behavior is related to the large negative value of E_m in (5.15) (see Fig. 1(e)). An explanation can be seen in Figs. 5.3(a) and 5.3(c). The mean flow distortion $\langle u \rangle$, while conserving the total flow rate, reduces $\langle u \rangle$ in the high-speed core, thus transforming the profile into one with lower energy.

The profiles of the $x-y$-averaged rms perturbations of the velocity components are shown in Figs. 4(a)–4(c). The perturbations are computed as in (5.14), i.e., with respect to the base flow. The profiles at $t = t_1$ show the effect of the TS rolls, which generate u' and w', but not v'. The profiles at $t = t_2$, when the flow is apparently turbulent, show significant differences with the profiles observed in the fully developed turbulent flows in a channel with a spanwise magnetic field [25]. In particular, the peaks of $((u'^2)^{1/2})$ are much farther from the wall in our case than in a developed turbulent flow. For $((w'^2)^{1/2})$, a distribution with the maximum in the middle instead of the distribution with two maxima not far from the wall typical for developed turbulence is observed. During the decay stage, at $t = t_3$, the perturbations are predominantly in the streamwise velocity component, which is in full agreement with the fact that the perturbations at this stage consist of the mean flow distortion and streak-dominated perturbations $\boldsymbol{u}''$ (see Figs. 5.1 and 5.2(d)).

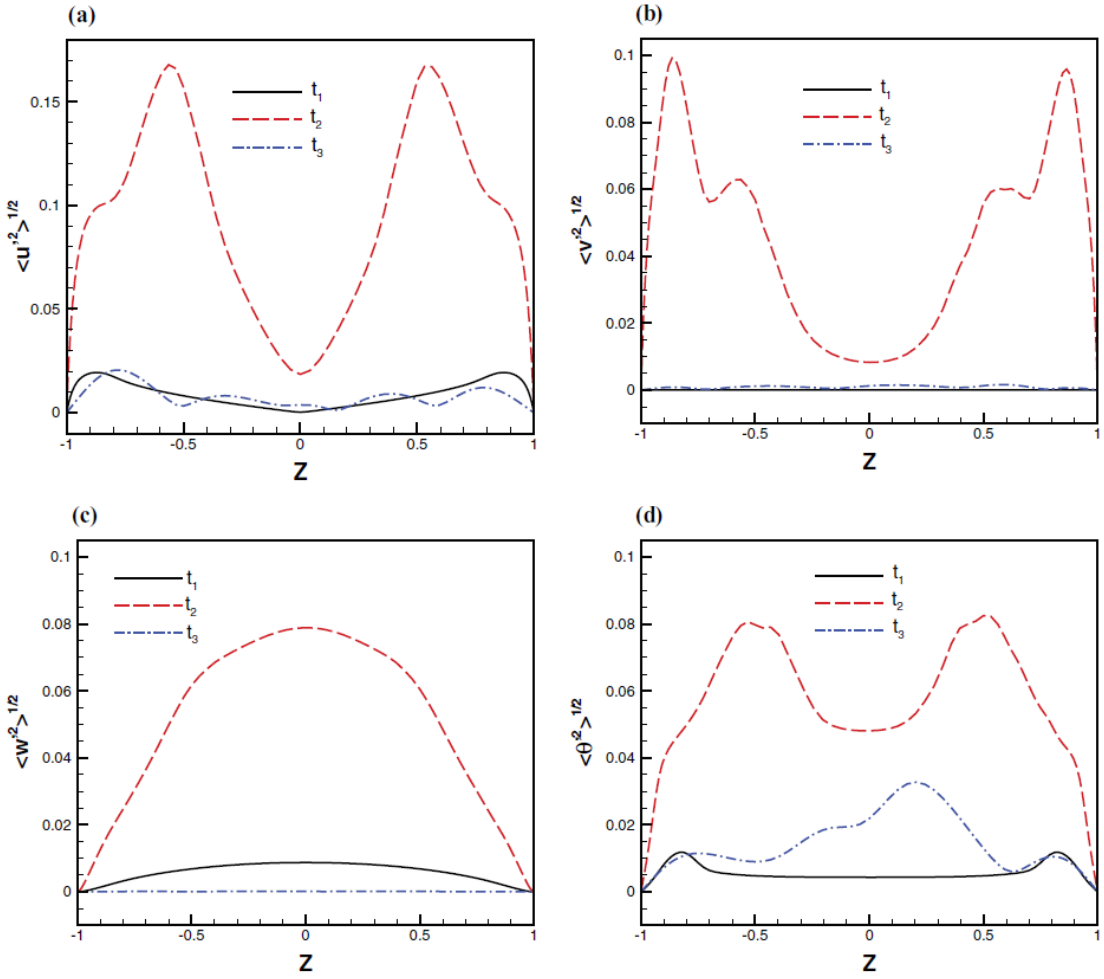

Figure 5.4: Profiles of *x*-*y*-averaged rms perturbations of velocity components and scalar at *Ha* = 80 at the stages of 2D growth (time t_1), turbulent burst (t_2), and decay (t_3) (see Fig. 5.1).

The wall-normal momentum transport by the velocity fluctuations is illustrated in Fig. 5.5(a) by the profiles of the Reynolds stress component $\tau_{13} \equiv \langle u'w' \rangle$. The transport is only noticeably strong during the turbulent burst. The computations of the correlation coefficient $\tau_{13}/((u'^2)^{1/2}(w'^2)^{1/2})$ have shown that, in addition to much larger amplitude of fluctuations, this is caused by stronger correlation between u' and w'.

The discussion of the evolution of velocity field during an intermittency cycle is concluded by the data in Fig. 5.6(a) presenting the skin friction coefficient C_f. In non-dimensional units, C_f is defined as the imposed pressure gradient needed to drive the flow. In agreement

with [15], C_f grows nearly twice the base flow level during the turbulent burst, when strong wall-normal momentum transfer is generated by velocity fluctuations, but remains very close to the base flow level during the rest of the cycle.

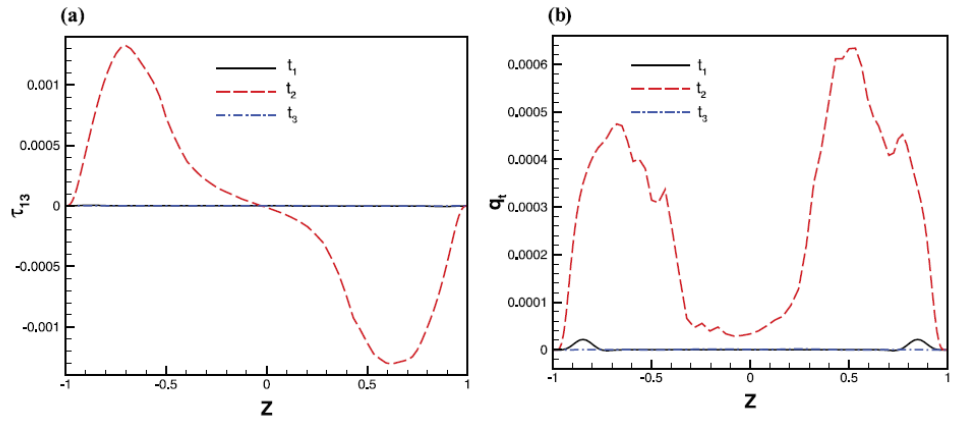

Figure 5.5: Profiles of *x*-*y*-averaged wall normal transport rates of momentum and scalar at Ha = 80 at the stages of 2D growth (time t_1), turbulent burst (t_2), and decay (t_3) (see Fig. 5.1).

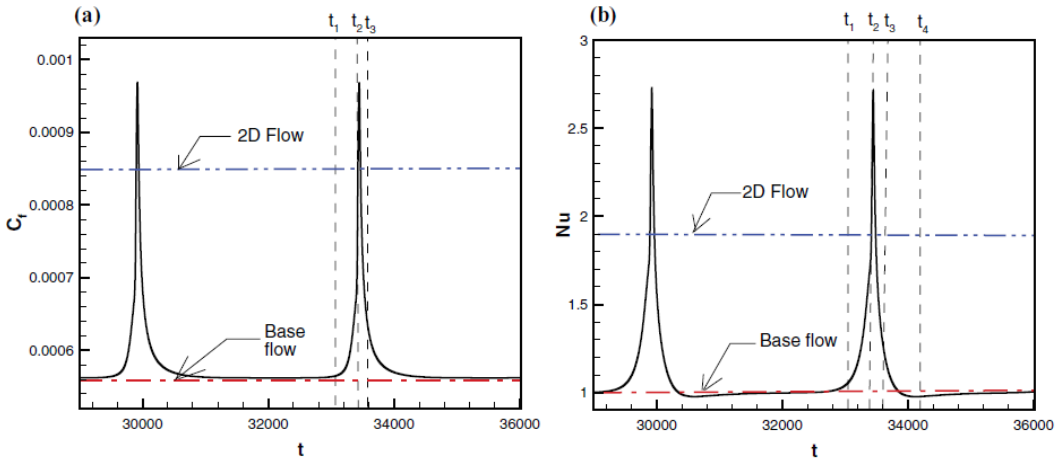

Figure 5.6: Evolution of the skin friction coefficient (a) and Nusselt number (b) at Ha = 80 during the same two cycles as in Fig. 1. Two horizontal lines show the values for the base flow state (5.13) and the perfectly 2D flow [55] obtained in our case at Ha = 160 and higher.

5.3.3 Passive scalar during an intermittency cycle

The evolution of the scalar field during an intermittency cycle at Ha = 80 is presented in Figs. 5.1–5.6. Various characteristics are shown in parallel with the respective characteristics of velocity. Considering the energy curves of the scalar perturbations θ'' with respect to the instantaneous mean distribution (see Fig. 5.1(b)) and the spatial structure of θ'' at the typical time moments (see Figs. 5.2(a), 5.2(c), and 5.2(e)), It can concluded that the scalar field goes through the same three stages as the velocity field.

In the growth stage, the scalar energy E_θ'' is practically identical to the energy of the spanwise uniform instability modes $E_{\theta sp}''$. A prominent feature of the scalar distribution at this stage is the sheet-like zones of large positive and negative θ'' extending along the walls (see Fig. 5.2(a)). The absence of strong correlation between $\boldsymbol{u}''$ and θ'' visible in Fig. 5.2(a) is because of the difference between the speeds of streamwise transport of the scalar (the local speed of the mean flow) and the phase speed of the moving TS rolls.

During the turbulent burst, the quasi-2D structure of the scalar perturbations breaks down into a three-dimensional distribution that has the typical spanwise length scale similar to the scale of velocity distribution (see Fig. 5.2(c)). In the decay stage, the scalar perturbations are nearly streamwise independent ($E_\theta'' \approx E_{\theta sp}''$ in Fig. 5.1(b)) and are dominated by streak-like structures (see Fig. 5.2(e)).

Considering the decomposition of the scalar perturbations θ' into the deformation of the mean scalar profile $\Delta\theta$ and the perturbations with respect to the instantaneous mean θ'' (see Fig. 5.1(d)), it is found that, similarly to velocity, $\Delta\theta$ is negligibly weak during the growth stage, but is much stronger than θ'' during the decay stage, when it constitutes practically entire θ'. Similarity to velocity field in the behavior of the total energy of the scalar E_θ (see Fig. 5.1(f)) is also seen. It increases above the base flow level $E_{\theta base} = 1/3$ during the late growth and early turbulent stages. After the peak of the turbulent burst, E_θ

drops sharply below $E_{\theta base}$ as a result of the mean flow transformation causing negative $E_{\theta m}$ in (5.15).

The qualitative similarity between the evolutions of scalar and velocity is not surprising, since the second largely determines the first. At the same time, certain differences are observed. One is that the energy of scalar perturbations decays much slower after the burst than the kinetic energy. This is true for the perturbations with respect to instantaneous mean (cf. Figs. 5.1(a) and 5.1(b)) and with respect to the base state (cf. Figs. 5.1(c) and 5.1(d)). As a result, the minimum levels reached by the scalar perturbation energies are several orders of magnitude higher than the minima of kinetic energies. The slower decay of the scalar can be explained by the fact that the scalar is not directly affected by the Joule dissipation. Its decay is caused solely by diffusion.

Yet another difference between the dynamics of the scalar and velocity fields can be observed in Fig. 5.1. The visible switch from decay to growth occurs significantly (hundreds of time units) later for the scalar than for velocity. This cannot be attributed to the delayed correlation buildup between velocity and scalar, since the time needed for the buildup is ∼1 in our variables. The correct explanation is that the "switch" indicates the time moment when the energy associated with the growing TS rolls exceeds the energy of the decaying components. Since the decay is slower for the scalar than for velocity, the "switch" occurs at a higher amplitude of growing perturbations and, thus, at a later time.
The transformation of the mean scalar $\langle\theta\rangle(z, t)$ and its deviation $\Delta\theta$ from the base flow distribution (5.13) is illustrated in Figs. 5.3(b) and 5.3(d). It is evident that strong transformation develops during the turbulent burst and persists during the decay stage (see profiles at $t = t_2$ and $t = t_3$). The transformation is rather peculiar in its dissimilarity to the transformation observed in the fully developed turbulent flows (see, e.g., Ref. 35). Boundary layers similar to those in a turbulent flow develop near the walls. The shape of the profile between the boundary layers is, however, quite different from the nearly straight line typical for turbulent flows. As the middle of the channel is considered, the slope

becomes nearly zero just outside the boundary layer and then increases rising above the slope of a laminar profile.

The rms scalar perturbations $(\theta'^2)^{1/2}$ and the wall-normal scalar transport by velocity fluctuations $q_t = \langle w'\theta' \rangle$ are shown, respectively, in Figs. 5.4(d) and 5.5(b) illustrate two interesting features of the scalar evolution. One is that the spatial distribution of $(\theta'^2)^{1/2}$ tends to be more similar to the distribution of $(u'^2)^{1/2}$ than $(w'^2)^{1/2}$. The correlation coefficients $R_{u\theta} = \langle u'\theta' \rangle / ((u'^2)^{1/2}(\theta'^2)^{1/2}$ has been computed (not shown) and found that $R_{u\theta}$ is consistently larger than $R_{w\theta}$. This dominance of the streamwise velocity component in determining the passive scalar distribution is known from the studies of turbulent scalar transport in shear flows. The main explanation is that $\boldsymbol{u}'$ is simply stronger than $\boldsymbol{w}'$.

Another interesting feature is the distribution of scalar flux q_t during the turbulent burst ($t = t_2$ in Fig. 5.5(b)). q_t has two "bulges" near the walls, but is small in the middle of the channel. It has been found that the suppression of the scalar transport is primarily due to almost zero correlation between w' and θ' in the middle. The "bulges" of q_t provide an explanation of the peculiar shape of $\langle \theta \rangle$ at t_2 and t_3 observed in Fig. 5.3. Applying, as an approximation, the steady-state balance of the $x-y$-averaged wall-normal scalar transport (see, e.g., Ref. 35 or other works on turbulent scalar transport in channels), it is found that local increase of q_t must be accompanied by corresponding decrease of diffusive transport and, thus, of the slope of $\langle \theta \rangle$.

The transformation of the scalar distribution affects the global wall-to-wall scalar transport, which we define as the Nusselt number:

$$Nu \equiv 2 \frac{dT}{dz}\Big|_{wall} \tag{5.17}$$

The wall-normal derivative in (5.17) can be taken at $z = -1$ or $z = 1$. The choice may have a slight effect on the instantaneous values, but the shapes of the curves $Nu(t)$ and the values obtained by time integration over the intermittency cycle are, of course, the same.

The Nusselt number computed at $Ha = 80$ is shown as a function of time in Fig. 5.6(b). Strong (nearly three-fold) increase during the turbulent burst is observed. During the rest of the cycle, Nu is much smaller, close to the value $Nu = 1$ of the base flow. Interestingly, during the significant time period of the late decay and early growth stages, when the flow is close to its base state, Nu is smaller than 1. The scalar transport can be called "sub-diffusive." The effect is found in the present computations in the intermittent regimes at $Ha = 60$, 80, 100, 120, and 140. It becomes stronger at higher Ha. The minimum value of Nu is 0.883 at $Ha = 120$ and 0.718 at $Ha = 140$. The phenomenon has been investigated and it is found that it is caused by a modification of the mean scalar profile. An illustration is provided in Figs. 5.3(b) and 5.3(d), which shows $\langle\theta\rangle$ and $\Delta\theta$ at the moment t_4 corresponding, as shown in Fig. 5.6(b), to $Nu < 1$. The profile deviates from the base state (5.9) so that the slope $|d\theta/dz|$ at the wall is slightly smaller than the base state value 1/2. The reasons for formation of such a profile become clear if the distribution of the mean scalar forming in the result of a turbulent burst (see, e.g., curves of $\langle\theta\rangle$ and $\Delta\theta$ for $t = t_3$ in Figs. 5.3(b) and 5.3(d)) is considered. As a result of non-uniform turbulent scalar flux q_t (see Fig. 5.5(b)), the distribution of $\Delta\theta$ has two stronger peaks in the middle of the channel and two weaker peaks near the walls. The transformation of the profile after the burst is predominantly controlled by diffusion. It is virtually evident, but has also been confirmed by the current solution of the one-dimensional diffusion equation, that this transformation leads to the profiles of $\langle\theta\rangle$ and $\Delta\theta$ illustrated by the curves at $t = t_4$ in Figs. 5.3(b) and 5.3(d).

The analogous "sub-viscous" wall-normal momentum transport with C_f below the base flow value $3Re^{-1} = 0.00056253$ during the late decay and early growth stages is also detected in the present simulation, but the effect is much weaker and only observed at Ha

= 120 and 140. The minimum value of C_f is 0.0005619 at *Ha* = 120 and 0.000539 at *Ha* = 140.

5.3.4. Effect of Hartmann number

This section reports the results of our study of the influence of the magnetic field strength, as defined by the Hartmann number, on the intermittency. At each *Ha*, integral characteristics, such as the cycle duration and the maximum and cycle-averaged energies, are obtained by time-averaging over ten consecutive intermittency cycles. As it has been already mentioned, variations among the cycles are small, so the data can be considered as characteristics of an individual cycle. The data for the fully turbulent flow at *Ha* = 30 and for the purely 2D (spanwise-uniform) flow at *Ha* = 160 are included for comparison, where appropriate.

Considering the nature of the direct (via the Joule dissipation) effect of the magnetic field on the flow, conjectures can be made concerning the influence of field strength on the intermittency cycle. As illustrated later in this section, the real behavior is largely in accordance with the reasoning, although more subtle in some aspects.

The strength of the magnetic field does not affect the growth of the TS rolls, which are spanwise uniform. On the contrary, the turbulent burst is sensitive to the field strength. A stronger magnetic field should slow down the development of secondary instabilities, thus extending the 2D growth phase and allowing the TS rolls to grow longer and to a higher amplitude before they break down. A stronger magnetic field should also result in stronger suppression of 3D velocity perturbations and, thus, lower amplitude and smaller duration of the burst. During the decay phase, a stronger magnetic field should lead to faster decay of perturbations $\boldsymbol{u}''$ with respect to the instantaneous mean, but cannot directly affect the mean flow distortion Δu . The effect of the magnetic field on the scalar is, of course, indirect, via the velocity field. Taking into account the correlation between the velocity and

scalar intermittency cycles demonstrated earlier in this section, similar changes in the evolution of scalar field are expected.

The time characteristics of the intermittency cycle are presented in Fig. 5.7. The curves of the kinetic perturbation energy E' (see Fig. 5.1(c)) are used to evaluate the growth and decay times measured, respectively, as the intervals, during which E' grows from a minimum to a maximum at the peak of a turbulent burst and from a maximum to the next minimum. As it is predicted, the decay time decreases strongly with *Ha*. The projected increase of the growth time, however, does not occur. The tendency is that the growth time decreases with *Ha*, albeit significantly slower than the decay time and with some growth between *Ha* = 60 and 80 and between *Ha* = 100 and 120.

To explain this behavior, it can be recalled that the perturbation energy E' consists of the energy E'' of the perturbations $\boldsymbol{u}''$ with respect to the instantaneous mean and the energy ΔE of the mean flow distortion. During the decay stage, ΔE dominates and the time moment $t_{\min}$ of minimum E' is, in fact, the moment when the energy E' of the growing TS rolls first exceeds the decaying ΔE (see Fig. 5.1(c)). Stronger suppression of turbulent burst fluctuations by a stronger magnetic field inhibits the energy transfer from the mean flow to fluctuations and, as it is found, leads to slower decay of ΔE. As a result, the cross-over moment $t_{\min}$ occurs at higher values of ΔE and E''. The effect is not very strong, but sufficient to somewhat lengthen the decay stage and, correspondingly, shorten the growth stage.

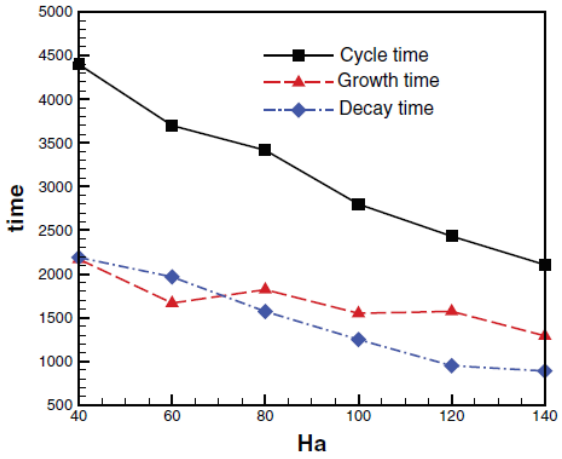

Figure 5.7: Growth time, decay time (see text for definitions), and total intermittency cycle time as functions of *Ha*. The results are obtained by averaging over ten consecutive cycles of fully developed intermittent flows.

The cumulative effect is that the total cycle length is reduced significantly at higher *Ha*. The data illustrating the effect of the Hartmann number on the energy characteristics are presented in Fig. 5.8. It is shown that the kinetic and scalar energies of the perturbations $\boldsymbol{u}'$ and θ' with respect to the base flow (see (5.9)) split into the spanwise-uniform (2D) and non-uniform (3D) components. The energy curves marked as 2D thus show the characteristics of 2D TS rolls and mean flow distortion, while the curves marked as 3D show the energies of 3D fluctuations resulting from the secondary instabilities of the TS rolls. For the kinetic (Figs. 5.8(a) and 5.8(b)) and scalar (Figs. 5.8(c) and 5.8(d)) energies, the maximum and average values during a cycle are shown, both obtained by averaging over ten consecutive cycles of a fully developed flow.

It can be observed that a stronger magnetic field means reduction of the maximum and average values of the kinetic energy of 3D modes. This is an effect of stronger Joule suppression of turbulence during the burst. At the same time, the maximum value of the 2D energy has the tendency to increase. Similar tendencies are observed for the energy of the scalar.

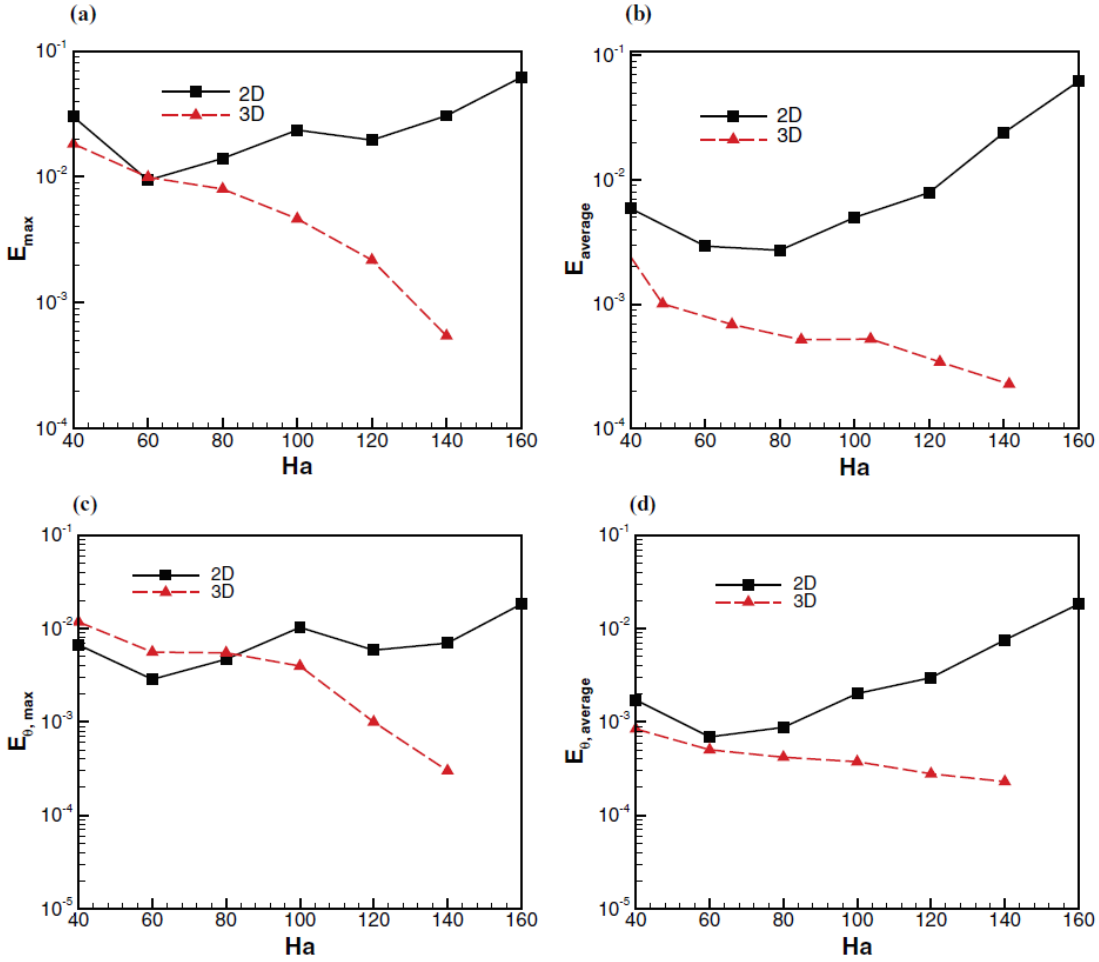

Figure 5.8: Maximum and cycle-averaged kinetic and scalar energies of the perturbations $\boldsymbol{u}'$ and θ' with respect to the base flow (5.9). The energies of perturbations uniform (2D) and non-uniform (3D) in the spanwise direction are shown separately as functions of *Ha*. The data are obtained as in Fig. 5.7. The 2D energy points at *Ha* = 160 correspond to the purely 2D non-intermittent flow regime obtained at this *Ha*.

The behavior of the cycle-averaged energies shown in Figs. 5.8(b) and 5.8(d) is a cumulative result of the change of the time and energy characteristics of the cycle. One can identify the main tendencies: a stronger magnetic field leading to increase of the energy of 2D spanwise-independent components of velocity and scalar fields (except at small *Ha*) and decrease of the energy of 3D components. The just concluded discussion of the effect of magnetic field strength on the dynamics of an intermittency cycle helps to understand

the behavior of the maximum and cycle-averaged friction coefficient and Nusselt number shown in Fig. 5.9.

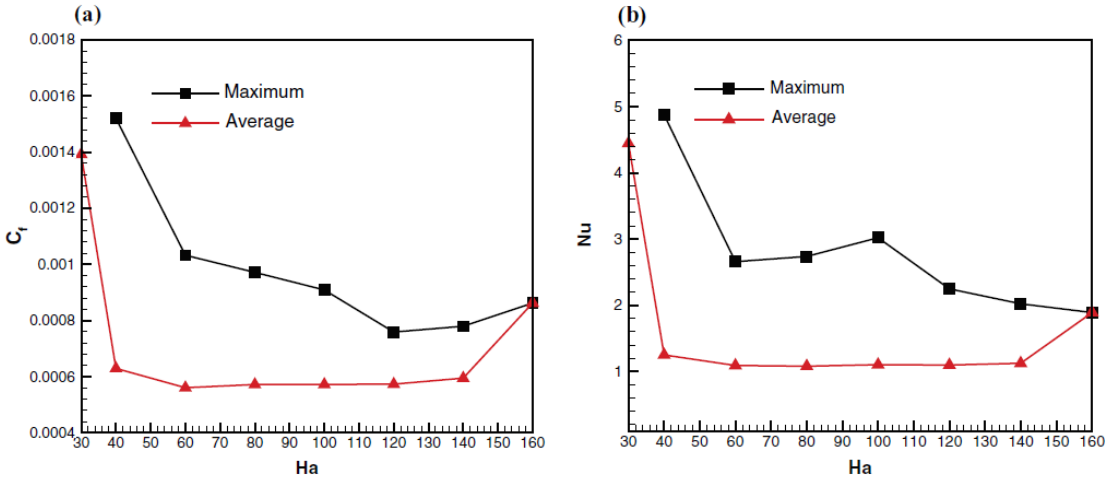

Figure 5.9: Friction coefficient C_f and Nusselt number Nu as functions of Ha. Maximum and cycle-averaged values obtained as in Figs.7 and 8 are shown. The points at Ha = 160 correspond to the purely 2D non-intermittent flow regime. The points at Ha = 30 are for the sustained turbulent flow obtained at this Ha.

One can think of three limiting values of C_f and Nu: the lowest values corresponding to the base flow, the significantly higher values corresponding to the fully developed 2D flow, in which the momentum and scalar transport are provided by finite-amplitude deformed TS rolls (see Fig. 5.6 and the points at Ha = 160 in Fig. 5.9), and the even higher values of a turbulent flow. An intermittency cycle is a solution trajectory between the unstable attractors of the base flow and turbulence. The time spent by the solution near the turbulence attractor is much smaller than the time spent near the base flow state. Accordingly, C_f and Nu of intermittent regimes show the cycle-averaged values only slightly higher than the base flow limits. The effect of the strength of the magnetic field on the average values is very weak. The maximum values of C_f and Nu are significantly higher than the base flow and 2D flow limits, but, except at Ha = 40, lower than the values obtained in a truly turbulent flow at Ha = 30. The effect of Ha on the maximum values of

C_f and Nu is to reduce them, which can be attributed to suppression of 3D turbulent fluctuations by the magnetic field.

5.4 Conclusion

A detailed parametric study of the phenomenon of large-scale intermittency in the MHD channel flow with spanwise magnetic field has been presented in this section. The current study expands the understanding on intermittency with complete picture on perturbation dynamics and energy spectrum during intermittency phenomena. In particular, the proposed doctoral study on intermittency describes the dynamics of a passive scalar field and quantify the effect of the intermittency on the transport rate. It is found that the scalar perturbations and the Nusselt number follow the cyclic evolution correlated with the cycles of velocity, albeit with some differences and unexpected effects, such as the sub-diffusive scalar transport during a significant segment of the cycle. Strong deformations of mean velocity and scalar that dominate velocity and scalar perturbations during the decay stage have been observed. The effect of the strength of the magnetic field on an intermittent flow is found to be complex, although the main features can be identified as the stabilization of the growing TS rolls and suppression of their secondary instabilities and the resulting turbulence.

A few comments are in order concerning the effect of the parameters of the numerical model on the results. The spanwise and streamwise sizes of the computational domain are particularly important in the current study. The streamwise size affects the growth rate and secondary instabilities of the TS rolls [74, 75]. Increasing this size in the current model could lead to some change in the duration of the growth phase and the strength of turbulent bursts, but is not expected to have a substantial effect on the nature of the cycling.
Increasing the spanwise size of the computational domain would activate modes of larger spanwise wavelengths, which are less susceptible to the suppression by the magnetic field. The test studies reported in [15] indicate that the result would be the shift of the upper boundary of the range of Ha, in which the intermittency is observed, to higher values. At

the same time, the principal mechanisms of growth and decay causing the intermittency would not change, so the cycling would remain largely the same. Furthermore, it should be considered that in any real system the spanwise size is limited by the Hartmann walls. It would be interesting to conduct the simulations at the same time scale as in the present study, but in a much larger computational domain. This could, among other possible results, clarify the relation between the time intermittency and the spatial intermittency in the form of turbulent stripes observed, among other systems, in the channel flow with imposed magnetic field [76]. The study has to be left for the future, when it becomes computationally more feasible. Yet another feature of the numerical model with possible implications for the intermittency effect, namely the constant flux formulation used in the present model. To verify the effect, a test run with constant imposed pressure gradient is conducted, which has been taken equal to the gradient in the laminar base flow at the same *Re*. Intermittency cycling with period about 4000 convective time units has been found. During the bursts, the perturbation energy grows to amplitudes comparable to the amplitudes reported earlier in this section. The increase of flow resistance during each burst cause approximately 5% drop of mean flow velocity. This implies reduction of the effective Reynolds number that assists the magnetic field in suppression of perturbations. After the suppression, the mean velocity increases back to nearly the base flow value and the next cycle begins. In order to evaluate the practical implications of the intermittency for the scalar transport and dispersion, the effect of the Prandtl (Schmidt) number has to be considered. In liquid metals, the Prandtl number is typically small ($\sim 10^{-2}$–10^{-1}). This means that the heat transfer is dominated by conduction and, probably, affected only slightly by the turbulent bursts. On the contrary, the Schmidt number tends to be larger than one. The effect of the intermittency on the admixture transport and dispersion is, therefore, significant, probably stronger than present study. The possibility of the existence of a flow cannot be excluded, in which periodic turbulent velocity bursts lead to sustained turbulent fluctuations of a scalar. This can be a subject of future investigations.

CHAPTER VI

1D MODEL FOR FLOW FIELD AND PASSIVE SCALAR TRANSPORT

6.1 Introduction

One of the desired outcomes of a direct numerical simulation (DNS) is the detection of possible simple relationships between the mean flow characteristics and the problem parameters. Especially sought for are such relationships for the coefficients of eddy viscosity and diffusivity, since they may provide a basis for development of simple low-dimensional models of the mean flow. For example, in present study, a highly desired outcome would be a set of simple approximate formulas modeling the behavior of eddy viscosity ($\nu_t(z)$), eddy diffusivity ($\alpha_t(z)$) and turbulent Prandtl number ($Pr_t(z)$). Such simple formulas derived from DNS are not unheard of in MHD. For example, the LES Smagorinski constant in homogeneous turbulence was shown in [77] to be well approximated by a linear function of the anisotropy coefficient (equation 3.8 in Chapter 3).

Accurate empirical relations that would express the effect of magnetic field via parameters of the problem, such as the Hartmann number *Ha*, magnetic interaction parameter *N*, or the anisotropy coefficients (equation 3.8 in Chapter 3) and (equation 4.21 in chapter 4) are difficult to formulate. As illustrated in figures 3.5, 4.7, and 4.8, the profiles of eddy viscosity, diffusivity, and Prandtl number change with the strength and orientation of the magnetic field in a complex way that does not allow a universal desired interpretation. However, models can be developed for each specific orientation of the magnetic field. In this section, this is done for the case of wall-normal magnetic field.

6.2 Background

In connection to the approach used in the current study to propose 1D models of mean flow and scalar for the case of a one-component fully developed flow of an electrically conducting fluid in a channel with imposed magnetic field, a review is conducted on the earlier work pertaining to mean flow and turbulence closure models. The review also provides a background of prior works done in the area where turbulence closure and transport models are proposed in general framework of DNS apart from the mean flow. Special attention is given on the eddy diffusivity and eddy viscosity modeling approach in describing the mean flow characteristics.

Due to the low computational cost, Reynolds-averaged Navier-Stokes (RANS) simulations are widely used for industrial flow simulations. However, RANS method has limitation in modeling complex turbulence interactions for the mean flow variables. There exists a scarcity of available literature on the application of RANS models for MHD flows. In general, RANS method is applied for MHD flow computations using RANS equations with standard turbulence models and wall functions. The current effort in regard to RANS simulation includes improvement on the standard approach through the development of MHD-specific turbulence models [78, 79] and wall functions.

An electromagnetically extended Reynolds stress transport model is developed by Widlund et al. [79] by transporting an additional scalar parameter which contained information on the dimensionality and anisotropy of the turbulence that is induced specifically by electromagnetic effects. Application of the model to a case of decaying turbulence in the presence of a magnetic field showed good agreement with DNS data.

Kenjeres er al [78] developed a model of magnetohydrodynamic (MHD) interactions within the framework of the second-moment closure based on direct numerical simulation (DNS). The MHD effects are taken care in the transport equations for the turbulent stress tensor and energy dissipation rate. The validation of the model is conducted in plane

channel flows with different orientation of magnetic field against the available DNS (*Re* = 4600, *Ha* = 6), large eddy simulation (*Re*=2.9 × 10^4, *Ha* = 52.5, 125) and experimental data (*Re* = 5.05 × 10^4 and *Re* = 9 ×10^4, 0≤ Ha ≤ 400) show good agreement for all considered cases.

Wilson et al. [80] performs study on capability of a linear eddy-viscosity type model (a low-Re k—ε model, with electromagnetic modifications as proposed by Kenjereš [78]), in successful capturing of the effects of the different force fields over two test cases; a simple 2D fully-developed channel flow with an imposed wall-normal magnetic field, and a 3D time-dependent case of Rayleigh–Bénard convection. In the channel flows (Re_τ = 150, 1150), the primary effect of the Lorentz force is found as a deformation in mean shear and a reduction in turbulent shear stress levels throughout the channel; something which the k—ε model is known to respond well to. As such, the additional electromagnetic modifications to the k and ε equations led to an overprediction of the reduction in shear stress, leading to the prediction of a laminar core region, in disagreement with DNS data.

Yamamoto et al. [81] propose a new RANS model for turbulent channel flows imposed wall-normal magnetic fields with heat transfer. This proposal model can be ensured adequate MHD effects on model functions and parameters in the turbulent eddy viscosity and the production minus destruction term of the epsilon-transport equation. With this new proposal model, the Nusselt number of several Prandtl number fluids (Pr = 0.025, 5.25 and 25) under the magnetic fields can be predicted in the range of less than 5% errors compared with the DNS database.

A detailed RANS based modeling approach with model for turbulent closure and scalar transport is beyond the scope of the current study. However, model equations are developed for mean flow and scalar for the case of a simplified one-component fully developed flow using the RANS approach for mean flow and scalar equation when the flow is statistically

steady. In developing the model equation, linear approximation of eddy diffusivity and eddy viscosity is used.

6.3 Model equation formulations for mean flow and scalar

In this section, the model equations for mean flow and scalar are derived by applying time averaging on the momentum and scalar transport equation. In RANS simulations, only the mean flow is computed. The non-dimensional MHD equations described in Chapter 2 (Equation 2.30-2.33) can be expressed in terms of the mean velocity, $\bar{\boldsymbol{u}}$, pressure $\boldsymbol{P}$ and electric current $\bar{\boldsymbol{J}}$, as,

$$\frac{\partial \bar{\boldsymbol{u}}}{\partial t} + (\bar{\boldsymbol{u}}.\nabla)\bar{\boldsymbol{u}} = -\nabla \boldsymbol{P} + \frac{1}{Re}\nabla^2 \bar{\boldsymbol{u}} + N(\bar{\boldsymbol{J}} \times \overline{\boldsymbol{e_B}}) + \frac{\partial \tau_{ij}}{\partial x_j} \tag{6.1}$$

$$\nabla.\bar{\boldsymbol{u}} = \boldsymbol{0} \tag{6.2}$$

$$\bar{\boldsymbol{J}} = -\nabla\varphi + \bar{\boldsymbol{u}} \times \overline{\boldsymbol{e_B}} \tag{6.3}$$

$$\nabla^2\varphi = \nabla.(\bar{\boldsymbol{u}} \times \overline{\boldsymbol{e_B}}) \tag{6.4}$$

Where, τ_{ij} represents turbulent stresses.

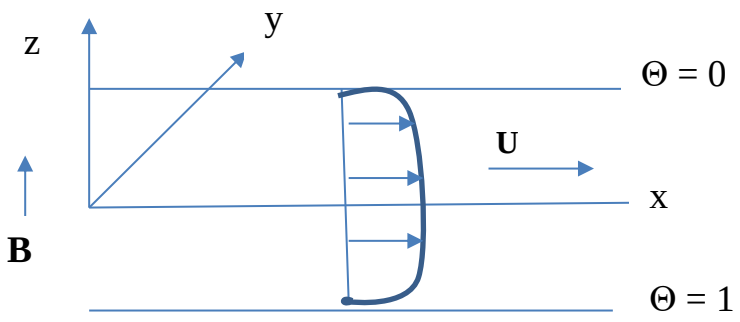

Figure 6.1: Schematic of fully developed streamwise flow in a channel with wall-normal orientation of magnetic field

If a fully developed, 1-compnent streamwise flow is considered (figure 6.1), equation (6.1) is simplified to the form in equation (6.5) below due to the achievement of statistical steady state by time averaging.

$$0 = -\nabla \boldsymbol{P} + \frac{1}{Re}\nabla^2 \overline{\boldsymbol{u}}_{\boldsymbol{x}} + N(\bar{\boldsymbol{J}} \times \overline{\boldsymbol{e}_{\boldsymbol{B}}}) + \frac{\partial \boldsymbol{\tau}_{\boldsymbol{13}}}{\partial \boldsymbol{z}} \tag{6.5}$$

Where mean velocity $\overline{\boldsymbol{u}}_{\boldsymbol{x}}$, is defined as,

$$\overline{\boldsymbol{u}}_{\boldsymbol{x}} = \boldsymbol{u}_{\boldsymbol{x}}(\boldsymbol{z})\, \bar{\boldsymbol{\imath}} \tag{6.6}$$

Equation (6.2) to (6.4) can be written with $\overline{\boldsymbol{u}}_{\boldsymbol{x}}$ as,

$$\nabla . \overline{\boldsymbol{u}}_{\boldsymbol{x}} = \boldsymbol{0} \tag{6.7}$$

$$\bar{\boldsymbol{J}} = -\boldsymbol{\nabla}\varphi + \overline{\boldsymbol{u}}_{\boldsymbol{x}} \times \overline{\boldsymbol{e}_{\boldsymbol{B}}} \tag{6.8}$$

$$\nabla^2 \varphi = \nabla . (\overline{\boldsymbol{u}}_{\boldsymbol{x}} \times \overline{\boldsymbol{e}_{\boldsymbol{B}}}) \tag{6.9}$$

The non-dimensional scalar transport equation presented in chapter 2 (equation 2.34) can be expressed in terms of mean mean passive scalar $T(z)$ as,

$$\frac{\partial T}{\partial t} + \overline{\boldsymbol{u}} . \nabla \theta = \frac{1}{PrRe}\nabla^2 T \tag{6.10}$$

For the case of fully developed streamwise 1D flow, the time averaging, eliminates the first term, $\frac{\partial T}{\partial t}$ in equation (6.10) as the passive scalar transport becomes statistically steady or time invariant. Equation (6.10) then can be written in terms of mean scalar $T(z)$ and turbulent scalar flux $q_t(z)$ as,

$$\frac{1}{PrRe}\frac{d^2T}{dz^2} - \frac{dq_t}{dz} = 0 \tag{6.11}$$

In chapter 4, the eddy diffusivity is defined as,

$$\alpha_t(z) = -\frac{q_t}{dT/dz} \tag{6.12}$$

The Peclet number (*Pe*) is defined as a ration of advective transport rate to diffusive transport and expressed as,

$$Pe = \frac{LU}{\alpha} = Pr\ Re \tag{6.13}$$

Substituting the relation (6.12), (6.13) into (6.11), the scalar transport equation can be written as follow,

$$\frac{d}{dz}\left[\left(\frac{1}{Pe} + \alpha_t\right)\frac{dT}{\partial z}\right] = 0 \tag{6.14}$$

The mean flow and mean passive scalar for the fully developed streamwise flow presented by equation (6.5) and (6.14) respectively will be considered for each orientation of magnetic field in the following section below.

6.3.1 Wall-normal magnetic field

The imposed wall-normal magnetic field are expressed as,

$$\text{Imposed magnetic field, } \overline{\boldsymbol{e_B}} = \overline{\boldsymbol{e_z}} \tag{6.15}$$

$$\overline{\boldsymbol{u}}_{\boldsymbol{x}} \times \overline{\boldsymbol{e_B}} = \begin{bmatrix} \bar{\imath} & \bar{J} & \bar{k} \\ \bar{u}_x & 0 & 0 \\ 0 & 0 & 1 \end{bmatrix} = (-\bar{u}_x)\,\bar{\boldsymbol{J}} \tag{6.16}$$

Substituting (6.16) to (6.9),

$$\nabla^2\varphi = \nabla.(\overline{\boldsymbol{u_x}} \times \overline{\boldsymbol{e_B}}) = \nabla.[(-\bar{u}_x)\bar{\boldsymbol{j}}] = -\frac{\partial \bar{u}_x}{\partial y} = 0 \tag{6.17}$$

which yields, $$\varphi = \text{constant} \tag{6.18}$$

Substituting (6.18) to (6.8),

$$\bar{\boldsymbol{J}} = -\boldsymbol{\nabla}\varphi + \overline{\boldsymbol{u_x}} \times \overline{\boldsymbol{e_B}} = (-\bar{u}_x)\,\overline{e_y} \tag{6.19}$$

Lorentz force is computed as,

$$\boldsymbol{F_L} = \bar{\boldsymbol{j}} \times \overline{\boldsymbol{B}} = \begin{bmatrix} \bar{\imath} & \bar{j} & \bar{k} \\ 0 & -\bar{u}_x & 0 \\ 0 & 0 & 1 \end{bmatrix} = -(\bar{u}_x)\bar{\boldsymbol{\imath}} \tag{6.20}$$

Substituting (6.20) in (6.5),

$$0 = -\nabla P + \frac{1}{Re}\nabla^2\bar{u}_x - N\bar{u}_x + \frac{\partial \boldsymbol{\tau_{13}}}{\partial \boldsymbol{z}} \tag{6.21}$$

Equation (6.21) represents the equation for mean flow for the case of imposed wall-normal magnetic field.

The pressure gradient for the case of the fully developed 1D flow is constant. As such ∇P can be expressed as,

$$\nabla P = \frac{dp}{dx} = \text{constant} = c \tag{6.22}$$

The turbulent stress tensor, τ_{13} is expressed as,

$$\tau_{13} = \nu_t \frac{d\bar{u}_x}{dz} \tag{6.23}$$

Substituting (6.22) and (6.23) in (6.21) and re-arranging, equation (6.21) becomes as follow,

$$\frac{d}{dz}\left[\left(\frac{1}{Re} + \nu_t\right)\frac{d\bar{u}_x}{dz}\right] - N\bar{u}_x = c \tag{6.24}$$

Equation (6.24) represents the general form of mean flow equation for the case of fully developed streamwise flow with imposed wall-normal magnetic field, the solution of which is presented in section 6.5.

6.3.2 Streamwise magnetic field

Considering the streamwise orientation of magnetic field,

$$\overline{\boldsymbol{e_B}} = \overline{\boldsymbol{e_x}} \tag{6.25}$$

Therebefore,

$$\overline{\boldsymbol{u}}_{\boldsymbol{x}} \times \overline{\boldsymbol{e_B}} = \begin{bmatrix} \bar{\imath} & \bar{j} & \bar{k} \\ \bar{u} & 0 & 0 \\ 1 & 0 & 0 \end{bmatrix} = 0 \tag{6.26}$$

Substituting (6.26) in (6.9),

$$\nabla^2\varphi = 0 \tag{6.27}$$

Or

$$\varphi = c_1 z + c_2 \tag{6.28}$$

The insulating boundary conditions in walls described in Chapter 2 (Equation 2.40),

$$\frac{\partial \varphi}{\partial n} = 0 \; at \; z = \pm 1 \tag{6.29}$$

Using (6.15) into (6.14),

$$\varphi = \text{ constant} \tag{6.30}$$

Substituting (6.26) and (6.30) in (6.8),

$$\bar{\boldsymbol{J}} = \mathbf{0} \tag{6.31}$$

Considering equation (6.31), it can be attributed that there is no direct effect of Lorentz force term for the case of streamwise magnetic field. The effect of magnetic field is solely in modification of turbulence.

6.3.3 Spanwise magnetic field

Considering the spanwise orientation of magnetic field,

$$\overline{\boldsymbol{e_B}} = \overline{\boldsymbol{e_y}} \tag{6.32}$$

$$\overline{\boldsymbol{u_x}} \times \overline{\boldsymbol{e_B}} = \begin{bmatrix} \bar{\imath} & \bar{\jmath} & \bar{k} \\ \bar{u} & 0 & 0 \\ 0 & 1 & 0 \end{bmatrix} = \bar{u}_x \bar{\jmath} \tag{6.33}$$

Substituting (6.33) in (6.9),

$$\nabla^2 \varphi = \nabla . (\overline{\boldsymbol{u_x}} \times \overline{\boldsymbol{e_B}}) = \frac{\partial \bar{u}_x}{\partial z} \tag{6.34}$$

The insulating boundary conditions in walls described in Chapter 2 (Equation 2.40),

$$\frac{\partial \varphi}{\partial n} = 0 \; at \; z = \pm 1 \tag{6.35}$$

Solving (6.34) and using the boundary conditions in (6.35).

$$\frac{\partial \varphi}{\partial z} = \bar{u}_x \tag{6.36}$$

Using (6.20) and (6.36) in (6.8),

$$\bar{\boldsymbol{J}} = -\bar{u}_x + \bar{u}_x = 0 \tag{6.37}$$

Considering equation (6.37), it can be concluded that there is no direct effect of Lorentz force at least in the zone of fully developed flow for the case of spanwise magnetic field.

6.4 Solution of Mean scalar with eddy diffusivity approximation

In this section, the solution of mean scalar equation (6.14) is presented through the linear approximation of eddy diffusivity for all magnetic field orientations.

Considering the linear approximation, the eddy diffusivity can be expressed as,

$$\alpha_t = a \; + bz \tag{6.38}$$

Substituting (6.38) in (6.14) yields,

$$\frac{d}{dz}\left[\left(\frac{1}{Pe} + a \; + bz\right)\frac{dT}{\partial z}\right] = 0 \tag{6.39}$$

Considering $k = \frac{1}{Pe} + a$, equation (6.39) can be re-written as,

$$\frac{d}{dz}\left[(k+bz)\frac{dT}{\partial z}\right]=0 \tag{6.40}$$

Solving the second order differential equation of (6.40), the scalar solution can be expressed as,

$$T(z)=\frac{c_1}{b}ln(k+bz)\ +\ c_2 \tag{6.41}$$

Where, c_1 and c_2 are constants, the value of which will be computed from the boundary conditions.

The mean scalar solution per equation (6.41) can be expressed per equation (6.42) and (6.43) considering piecewise linear profile of eddy diffusivity (see figure 6.1 for example) from the DNS result of eddy diffusivity profile (figure 4.8 in chapter 4 for wall-normal case).

For $-1\ \leq\ z\ \leq\ z^*,\ \ T^-(z)=\frac{c_1}{b}ln(k+bz)\ +\ c_2$ (6.42)

For $z^*\ \leq\ z\ \leq\ 0,\ \ T^+(z)=\frac{d_1}{b'}ln(k'+b'z)\ +\ d_2$ (6.43)

While considering the DNS profile of eddy diffusivity, only channel half-width is considered because of the symmetry of variation. As such figure 6.2 is showing the general scheme of piecewise linear profile approximation up to mid-channel width.

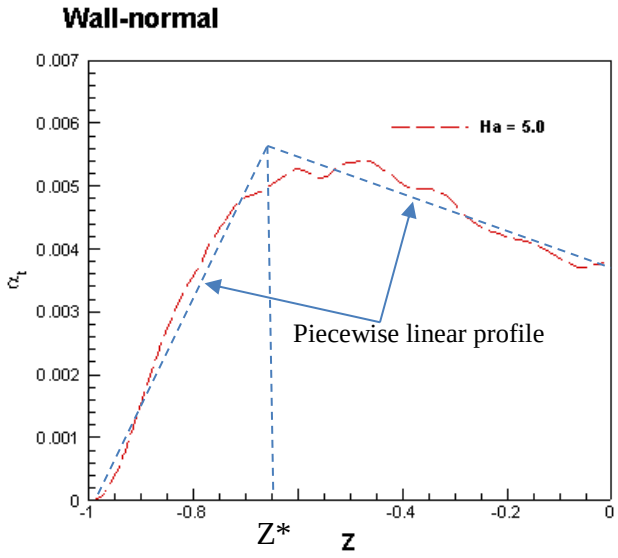

Figure 6.2: Piecewise linear approximation of eddy diffusivity for Ha=5 in imposed wall-normal magnetic field orientation

The imposed boundary condition for scalar in channel-walls are:

$$\theta = 1 \; at \; z = -1, \; \theta = 1/2 \; \; at \; z = 0 \tag{6.44}$$

Another boundary condition can be attributed considering the general piecewise profile of eddy diffusivity across the channel in wall-normal (z) direction.

Considering scalar profile for $-1 \leq z \leq z^*$, as $T = T^-$ and for $z^* \leq z \leq 0$, as $T = T^+$, the boundary condition at transition coordinate z^* is expressed as,

$$\frac{dT^-}{dz}(z^*) = \frac{dT^+}{dz}(z^*) \tag{6.45}$$

6.4.1 Mean scalar for wall-normal magnetic field orientation

As an illustration of the derived mean scalar per equation (6.42) and (6.43), the wall-normal case of Ha = 5 is presented here.

The piecewise linear profile for eddy diffusivity from the DNS profile of Ha =5.0 (figure 6.2) is estimated as:

For $-1 \leq z \leq z^* = -0.7, \ \alpha_t = 0.01933\ (1+z)$ (6.46)

For $z^* = -0.7 \leq z \leq 0, \ \alpha_t = 0.0036 - 0.00314z$ (6.47)

The transition co-ordinate z^* is estimated through optimization of fitting in OriginLab software where the regression error of goodness of fitting is minimized by chi-square statistical method [82].

Considering (6.46) and (6.47), the constants in the piecewise linear profiles are,

a=b=0.01933($for\ -1 \leq z \leq z^* = -0.7$) (6.48)

a=0.0036 and b=-0.00314 ($for\ z^* = -0.7 \leq z \leq 0$) (6.49)

Substituting the constants, a and b from (6.48) & (6.49) to (6.42) & (6.43) and using the BC's in (6.44) and (6.45), the solution for mean scalar is obtained for Ha = 5,

$$T^-(z) = -0.0776\ ln(0.019497 + 0.019333z) + 0.3194 \quad (6.50)$$

$$T^+(z) = 0.478\ ln(0.0038 - 0.00314z) + 2.5206 \quad (6.51)$$

The final solution for Ha =5 can be expressed as,

$$T(z) = \begin{cases} -0.0776ln(0.019497 + 0.019333z) + 0.3194, & -1 \leq z \leq z^* = -0.7 \\ 0.478\ ln(0.0038 - 0.00314z) + 2.5206, & z^* = -0.7 \leq z \leq 0 \end{cases} \quad (6.52)$$

Figure 6.3, shows the mean scalar distribution in the channel for *Ha* = 5.0 with imposed wall-normal magnetic field which is computed from the 1D model in (6.52) and compared with the DNS result. The 1D model, which is based on the approximation of eddy diffusivity, predicts the mean scalar distribution within reasonable accuracy compared to the DNS result.

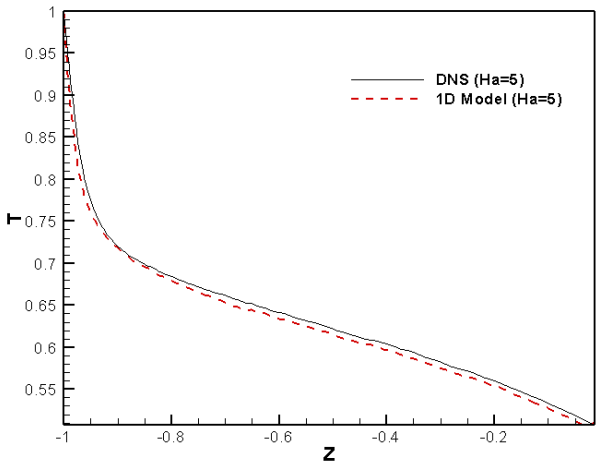

Figure 6.3: Distribution of Mean Scalar T(z) for Ha=5 for wall-normal case

The 1D models of scalar distribution for Ha = 0, 10.0 and 13.3 are obtained in similar way as described above for Ha =5. The model equations are as follow.

For Ha = 0,

$$T(z) = \begin{cases} -0.0276ln(0.03121 + 0.01837z) + 0.2125, & -1 \leq z \leq z^* = -0.68 \\ 0.256\, ln(0.0026 - 0.00414z) + 1.234, & z^* = -0.68 \leq z \leq 0 \end{cases} \quad (6.53)$$

For Ha = 10,

$$T(z) = \begin{cases} -0.072\, ln(0.031 + 0.0124z) + 0.3499, & -1 \leq z \leq z^* = -0.81 \\ 0.412\, ln(0.0045 - 0.00523z) + 2.6901, & z^* = -0.81 \leq z \leq 0 \end{cases} \quad (6.54)$$

For Ha = 13.3,

$$T(z) = \begin{cases} -0.068\, ln(0.027 + 0.0136z) + 0.4258, & -1 \leq z \leq z^* = -0.831 \\ 0.536\, ln(0.0065 - 0.0043z) + 2.7343, & z^* = -0.831 \leq z \leq 0 \end{cases} \quad (6.55)$$

Figure 6.4 shows the mean scalar distribution for Ha=0, 10 and 13.3 computed through the 1D models in (6.53-6.55) and compared with DNS results. Similar to Ha=5.0, the 1D models predict the distribution with reasonable accuracy. Figure 6.5, shows the mean scalar profile for all computed cases of Ha=0, 5, 10 and 13.3 through the 1D model solutions.

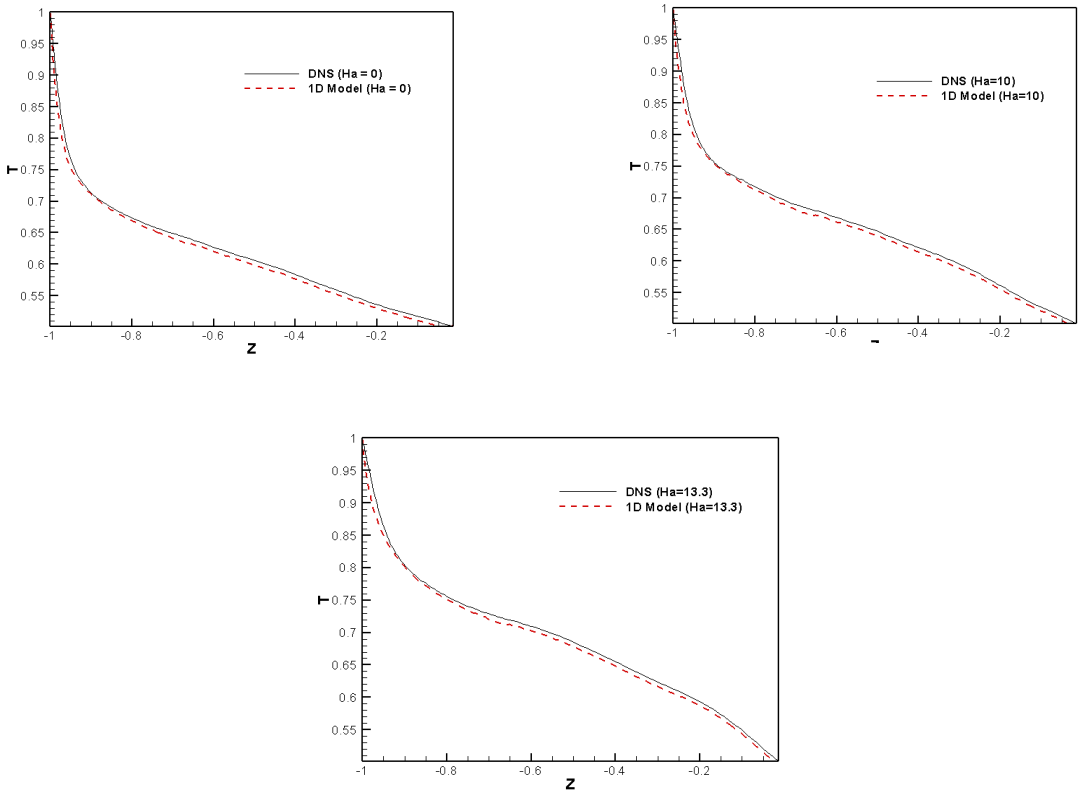

Figure 6.4: Distribution of Mean Scalar T(z) for Ha=0, 10 and 13.3 for wall-normal case

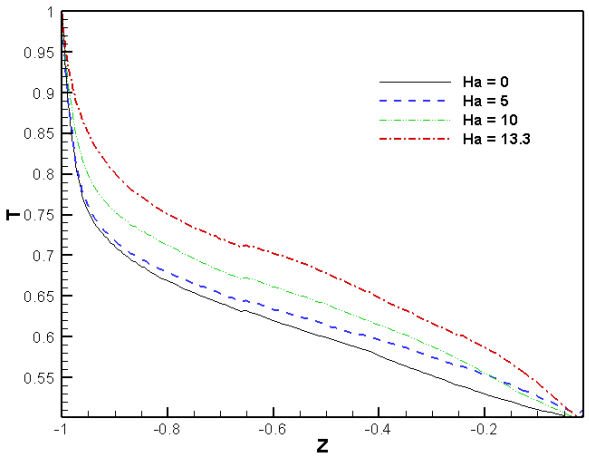

Figure 6.5: Profiles of mean scalar computed through the 1D model for wall-normal case

6.4.2 Mean scalar for spanwise magnetic field orientation

The 1D models of scalar distribution for Ha = 0, 10, 20 and 30 for spanwise orientation of magnetic field are obtained from the method outlined before in section 6.3.1. They are,

For Ha = 0,

$$T(z) = \begin{cases} -0.0362ln(0.0411 + 0.01236z) + 0.463, & -1 \leq z \leq z^* = -0.741 \\ 0.256\, ln(0.0026 - 0.00414z) + 3.63, & z^* = -0.741 \leq z \leq 0 \end{cases} \quad (6.56)$$

For Ha = 10,

$$T(z) = \begin{cases} -0.0289\, ln(0.0362 + 0.0258z) + 0.2621, & -1 \leq z \leq z^* = -0.744 \\ 0.377\, ln(0.0042 - 0.00364z) + 3.882, & z^* = -0.744 \leq z \leq 0 \end{cases} \quad (6.57)$$

For Ha = 20.0,

$$T(z) = \begin{cases} -0.068\, ln(0.027 + 0.0136z) + 0.4258, & -1 \leq z \leq z^* = -0.746 \\ 0.536\, ln(0.0065 - 0.0043z) + 2.2643, & z^* = -0.746 \leq z \leq 0 \end{cases} \quad (6.61)$$

For Ha = 30.0,

$$T(z) = \begin{cases} -0.068\, ln(0.027 + 0.0136z) + 0.4258, & -1 \leq z \leq z^* = -0.0.748 \\ 0.712\, ln(0.0312 - 0.013z) + 3.5167, & z^* = -0.748 \leq z \leq 0 \end{cases} \quad (6.58)$$

Figure 6.6 shows the mean scalar distribution for Ha=0, 10, 20 and 30 computed through

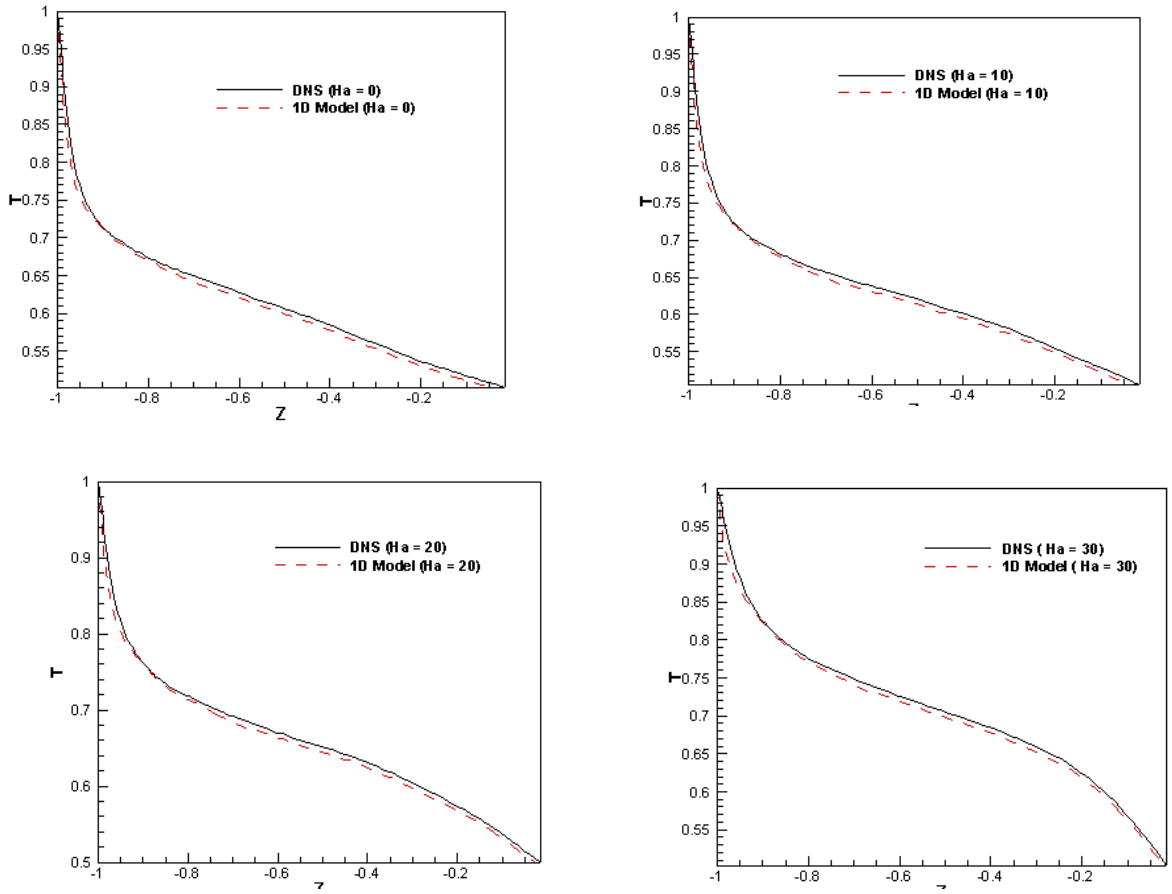

Figure 6.6: Distribution of Mean Scalar T(z) for Ha=0, 10, 20 and 30 for spanwise case

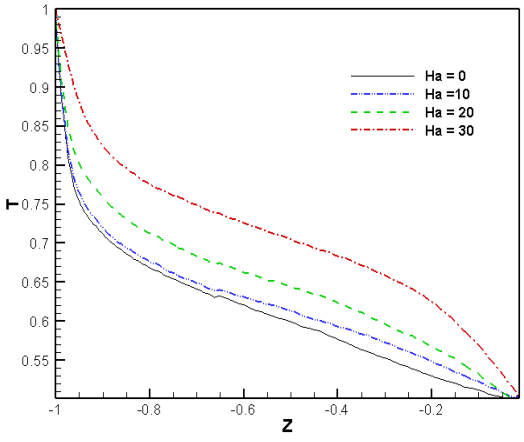

Figure 6.7: Profiles of mean scalar computed through the 1D model for spanwise case

the 1D models in (6.56-6.58) and compared with DNS results. Similar to Ha=5.0 in wall-normal case, the 1D models predict the distribution with reasonable accuracy. Figure 6.7, shows the mean scalar profile for all computed cases of Ha=0, 10, 20 and 30 through the 1D model solutions.

6.4.3 Mean scalar for streamwise magnetic field orientation

The 1D models of scalar distribution for Ha = 0, 10, 20 and 30 for streamwise orientation of magnetic field are obtained from the method outlined before. They are,

For Ha = 0,

$$T(z) = \begin{cases} -0.0332ln(0.0411 + 0.01236z) + 0.463, & -1 \leq z \leq z^* = -0.64 \\ 0.247\, ln(0.0028 - 0.00294z) + 1.1945, & z^* = -0.64 \leq z \leq 0 \end{cases} \quad (6.59)$$

For Ha = 10,

$$T(z) = \begin{cases} -0.042\, ln(0.0362 + 0.0258z) + 0.1946, & -1 \leq z \leq z^* = -0.642 \\ 0.258\, ln(0.0032 - 0.00314z) + 1.232, & z^* = -0.642 \leq z \leq 0 \end{cases} \quad (6.60)$$

For Ha = 20.0,

$$T(z) = \begin{cases} -0.049\, ln(0.027 + 0.0136z) + 0.2165, & -1 \leq z \leq z^* = -0.653 \\ 0.276\, ln(0.0039 - 0.0034z) + 1.2621, & z^* = -0.653 \leq z \leq 0 \end{cases} \quad (6.61)$$

For Ha = 30.0,

$$T(z) = \begin{cases} -0.053\, ln(0.018 + 0.0113z) + 0.2253, & -1 \leq z \leq z^* = -0.654 \\ 0.289\, ln(0.0043 - 0.0023z) + 1.1852, & z^* = -0.654 \leq z \leq 0 \end{cases} \quad (6.62)$$

Figure 6.8 shows the mean scalar distribution for Ha=0, 10, 20 and 30 computed through the 1D models in (6.56-6.58) and compared with DNS results. Figure 6.9, shows the mean scalar profile for all computed through the 1D model solutions.

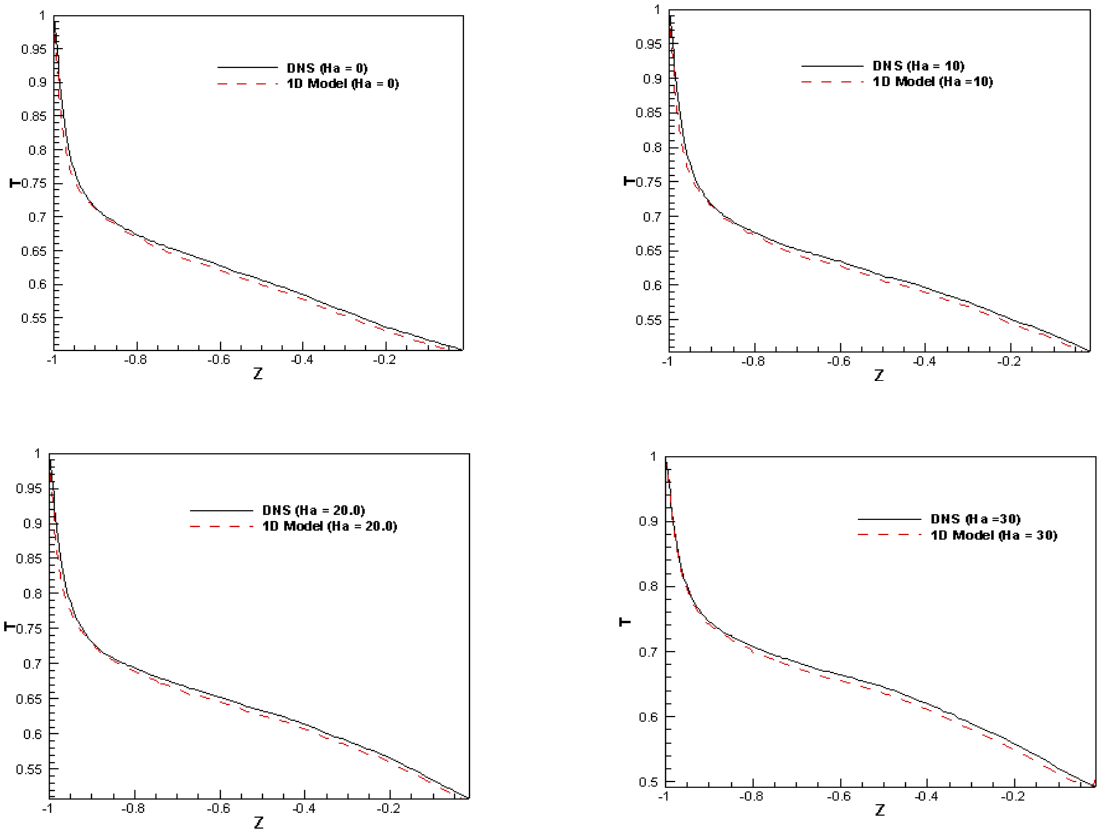

Figure 6.8: Distribution of Mean Scalar T(z) for Ha=0,10,20 and 30 for streamwise case

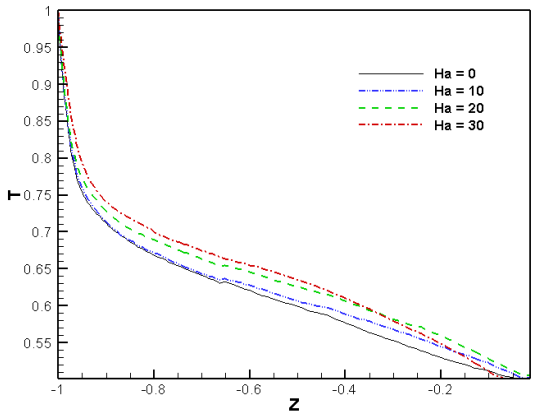

Figure 6.9: Profiles of mean scalar computed through the 1D model for streamwise case

6.5 Solution of mean flow with eddy viscosity approximation

In this section, the solution of mean flow equation (6.24) is presented considering linear approximation of eddy viscosity.

Considering linear approximation of eddy viscosity, ν_t

$$\nu_t = a + bz \tag{6.63}$$

Where a and b are constants of linear function.

Substituting (6.67) into (6.33) and by re-arranging it with definitions of constants, equation (6.33) is expressed as,

$$(az + k)\frac{d^2\bar{u}_x}{dz^2} + a\frac{d\bar{u}_x}{dz} - N\bar{u}_x = c \tag{6.64}$$

Where, $k = b + \frac{1}{Re}$.

Equation (6.64) can be also written as,

$$\bar{u}_x{}'' + \frac{a}{az+k}\bar{u}_x{}' - \frac{N}{az+k}\bar{u}_x = \frac{c}{az+k} \tag{6.65}$$

Which is similar to general form of non-homogenous second order linear differential equation with variable co-efficient expressed by,

$$u'' + p(z)u' + q(z)y = g(z) \tag{6.66}$$

Solution of equation (6.66) provides the mean flow, $\bar{u}_x(z)$

The linear approximation of the eddy viscosity is obtained using the DNS data illustrated in figure 3.5 of chapter 3. As illustrated in figure 6.10, the computed profile is approximated by a piecewise-linear function. The wall-normal coordinate z^* represents the transition coordinate for the piecewise linear profile of eddy viscosity in figure (3.5). The transition coordinate z^* is determined by optimization of fitting in OriginLab software where the regression error of goodness of fitting is minimized by chi-square statistical method [82].

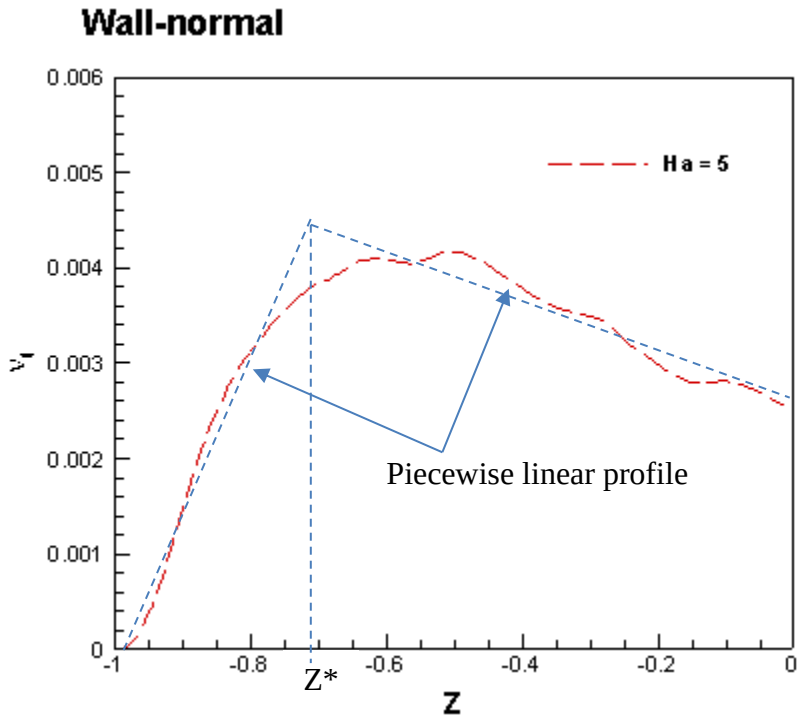

Figure 6.10: Piecewise linear approximation of eddy viscosity

As an example of determining the piecewise linear profile, the DNS data of eddy viscosity profile for Ha =5 is presented in figure 6.10.

For $-1 \leq z \leq z^* = -0.72, \ \nu_t = 0.02312(1+z)$ (6.67)

For $z^* = -0.72 \leq z \leq 0, \ \nu_t = 0.0052 - 0.00394z$ (6.68)

Considering (6.67) and (6.68), the constants in the piecewise linear profiles are,

$$\text{a=b=}0.02312(for\ -1 \leq\ z\ \leq\ z^* = -0.72) \tag{6.69}$$

$$\text{a=}0.0052 \text{ and b=-}0.00394\ (for\ z^* = -0.72 \leq\ z\ \leq\ 0) \tag{6.70}$$

The mean velocity profile is divided into two parts:

$$\bar{u}_x(z) = \bar{u}_x{}^-(z) \qquad \text{for } -1 \leq z \leq z^* \tag{6.71}$$

$$\bar{u}_x(z) = \bar{u}_x{}^+(z) \qquad \text{for } z^* \leq z \leq 0 \tag{6.72}$$

With the matching conditions,

$$\bar{u}_x{}^-(z^*) = \bar{u}_x{}^+(z) \tag{6.73}$$

Or,
$$\frac{d\bar{u}_x{}^-(z^*)}{dz} = \frac{d\bar{u}_x{}^+(z)}{dz} \tag{6.74}$$

The no slip boundary conditions at the walls are:

$$\bar{u}_x(-1) = 0 \tag{6.75}$$

The symmetry condition at $z = 0$ is expressed as,

$$\frac{d\bar{u}_x{}^+(0)}{dz} = 0 \tag{6.76}$$

The integral solution of constant volumetric rate is expressed as,

$$\int_{-1}^{z^*} \bar{u}_x{}^-(z)dz + \int_{z^*}^{0} \bar{u}_x{}^+(z)\, dz = 1 \tag{6.77}$$

The solution equation (6.77) for mean flow using the boundary conditions (6.73) to (6.77) and constants from (6.69) and (6.70) involves complex analytical solution expressed in terms of Bessel functions which is left as a scope for future studies. As an alternative, numerical shooting method can be attempted to solve the mean flow.

CHAPTER VII

CONCLUSIONS

The current study presents the results of the direct numerical simulations of turbulence and scalar transport in the channel flow with imposed magnetic field. The effect of different orientations and strength of the magnetic field is considered. The main conclusion is that *the imposed magnetic fields, especially those in the wall-normal and spanwise directions, significantly reduce the turbulent scalar transport and modify the properties of the scalar distribution.*

For the case of the wall-normal magnetic field, the study confirms findings reported in earlier works, which includes formation of a flattened core and Hartmann boundary layers in the mean velocity profile, noticeable reductions of the amplitude of perturbations of all three velocity components, etc. The current study shows that the reduction of the velocity fluctuations and eddy viscosity are significant in the case of the spanwise magnetic field and less so in the case of the streamwise magnetic field. The mean velocity is observed to be decreased with increase in magnetic field for the case of the wall-normal and spanwise magnetic field and observed to be largely unaffected by the streamwise magnetic field. The spatial structure analysis of flow transformation reveals that streamwise streaks develop near the channel walls at the magnetic field strength close to the laminarization threshold for the cases of the spanwise and wall-normal magnetic fields.

The flow transformation due to the influence of the magnetic fields also affects the scalar transport across the channel. Considering the distribution of mean scalar, the effect of the magnetic field appears to be qualitatively same for all three orientations. This includes widening of diffusion boundary layers and smaller decrease of mean scalar within it. The reduction of turbulent scalar flux is observed with the increase of the magnetic field

strength for all three orientations. The effect is more noticeable for the wall-normal and spanwise than for the streamwise magnetic field. The reduction of the scalar flux results in decrease of integral scalar transport across the channel which is presented as Nusselt number reduction in the current study. A linear approximation of the variations of the Nusselt number with magnetic interaction parameters is presented. This is a major outcome of the current study as one can utilize the correlations to evaluate the scalar transport across the channel. In broader sense, the correlations can be used for a more general situation of a turbulent flow with magnetic field. They indicate the trends in the change of the rate of turbulent transport in the directions parallel and perpendicular to the field. Instantaneous distributions of scalar near the boundary layer appears to follow the same pattern as those of velocity which is characterized by the development of high-speed and low-speed streaks in the streamwise direction. The effect is noticeable significantly for the case of wall-normal and spanwise magnetic fields due to the strong correlation between instantaneous velocity and scalar component. Development of strong scalar anisotropy is observed for the case of spanwise magnetic field.

The current study expands the understanding of large-scale intermittency and complements the analysis with detailed parametric studies with emphasis on scalar transport and perturbations dynamics. The effect of intermittency on the scalar transport rate is quantified in the present study. Generally, the scalar perturbations and Nusselt number are found to follow the cyclic evolutions correlated to cycles of velocity with some differences and unexpected effects such as sub-diffusive scalar transport rate during a significant segment of the cycle. The main features of the effect of the magnetic field on intermittent flow can be identified from the current study as the stabilization of the growing TS rolls and suppression of their secondary instabilities and the resulting turbulence.

Simple one-dimensional models for flow field and scalar transport are presented in the current study based on the linear approximations of eddy viscosity and eddy diffusivity using DNS results. Due to the complexity of analytical solution, only model equations are

presented for the case of flow field with associated boundary conditions. The solutions of derived 1D model concerning the mean scalar transport are presented for all of the Hartmann numbers considered in current study. The 1D model appears to provide reasonably accurate distribution of mean scalar which can be utilized for the case of channel flow with imposed magnetic field.

BIBLIOGRAPHY

[1] P. A. Davidson. An Introduction to Magnetohydrodynamics. Cambridge University Press, 2001.

[2] R.Moreau. Magnetohydrodynamics. Springer, 1990.

[3] U. Muller and L. Buhler. Magnetohydrodynamics in Channels and Containers. Springer, 2001.

[4] Kenneth R. Cramer and Shih-I Pai. Magnetofluiddynamics for engineers and applied physicists. McGraw-Hill book, 1978.

[5] W.E. Langlois. Buoyancy-driven flows in crystal-growth melts. Annu. Rev. Fluid Mech. 17, 191–215, 1985.

[6] Ola Widlund. Modeling of magnetohydrodynamic turbulence. Technical Report, Royal Institute of Technology, 2000.

[7] A.F. Lehman, G.R. Tallback and H.R. Hackl. Fluid flow control in continuous casting using various configurations of static magnetic fields. Processing of International Symposium on Electromagnetic Processing of Materials, 372-377, 1994.

[8] K. Takatani, Y. Tanizawa and M.Kawamoto. Mathematical model for fluid flow in a continuous casting mold with electromagnetic brake, Proceedings of the 3rd Int. Symposium on Electromagnetic Processing of Materials, EPM2000, 91-96, 2000.

[9] H.A. Wouters, R.P.J. Duursma, A.A.Kamperman and W.F.M. Damen. Modification of a turbulent two-phase flow by a magnetic field as applied to the continuous casting of steel. Proceedings of the 3rd Int. Symposium on Electromagnetic Processing of Materials, EPM2000, 182-187, 2000.

[10] Fundamental and Applied MHD. Proc. of 7th PAMIR conf. Giens, France, 2008.

[11] Aluminum Industry Technology Roadmap. Aluminum Association Inc., 1997.

[12] K. Moffatt. On the suppression of turbulence by a uniform magnetic field. J. Fluid Mech. 23, 571–592, 1967.

[13] O. Zikanov and A. Thess. Direct numerical simulation of forced MHD turbulence at low magnetic Reynolds number. J. Fluid Mech. 358, 299–333, 1998.

[14] A. Thess and O. Zikanov. Transition from two-dimensional to three-dimensional magnetohydrodynamic turbulence. J. Fluid Mech. 579, 383–412, 2007.

[15] T. Boeck, D. Krasnov A. Thess, and O. Zikanov. Large-scale intermittency of liquid-metal channel flow in a magnetic field. Phys. Rev. Lett. 101, 2008.

[16] J. Hartmann, J. and F. Lazarus. Hg-Dynamics {II}: Experimental investigations on the flow of mercury in a homogenous magnetic field. K. Dan. Vidensk. Selsk., Mat. Fys. Medd 15, 1-45, 1937.

[17] H. Branover. Magnetohydrodynamic flow in ducts. Wiley, 1978.

[18] J. Hartmann, J., Hg-Dynamics I: Theory of the Laminar Flow of an Electrically Conductive Liquid in a Homogeneous Magnetic Field. K. Dan. Vidensk. Selsk., Mat.-Fys. Medd.15(6), 1–28, 1937.

[19] O. Zikanov, D. Krasnov, T. Boeck, A.Thess, M. Rossi. Laminar-Turbulent Transition in Magnetohydrodynamic Duct, Pipe, and Channel Flows. Applied Mechanics Review.66, 2014.

[20] D. Lee and H. Choi. Magnetohydrodynamic turbulent flow in a channel at low magnetic Reynolds number. J. Fluid Mechanics 429, 367-394, 2001.

[21] H. Kobayashi. Large eddy simulation of magnetohydrodynamic turbulent channel flows with local subgrid-scale model based on coherent structures. Phys. Fluids 18, 1-11, 2006.

[22] S. Satake, T. Kunugi, T. Kazuyuki and O. Yasuo. Direct numerical simulation of turbulent channel flow under a uniform magnetic field for large-scale structures at high Reynolds number. Phys. Fluids 18, 2006.

[23] T. Boeck, D. Krasnov and E. Zienicke. Numerical study of turbulent magnetohydrodynamic channel flow. J. Fluid Mech., 572, 179-188, 2007.

[24] H. Noguchi, and N. Kasagi. Direct Numerical Simulation of Liquid Metal MHD Turbulent Channel Flows, (in Japanese), Preprint of JSME, 365-366, 1994.

[25] D. Krasnov, O. Zikanov, O., J. Schumacher. and T. Boeck. Magnetohydrodynamic Turbulence in a Channel with Spanwise Magnetic Field, Phys. Fluids 20, 2008.

[26] Y. Yoshinobu, T.Kunugi. Discussion on heat transfer correlation in turbulent channel flow imposed wall-normal magnetic field. Fusion Engineering and Design. 86, 2011.

[27] R. P. Feynman, R. B. Leighton, and M. Sands. The Feynman lectures on physics, vol. 2: Mainly electromagnetism and matter. Addison-Wesley, 1979.

[28] D. Krasnov, O. Zikanov, and T. Boeck. Comparative study of finite difference approaches to simulation of magnetohydrodynamic turbulence at low magnetic Reynolds number. Comp. Fluids 50, 46–59, 2011.

[29] Y.Morinishi, T.S.Lund, O.V.Vasilyev, and P.Moin. Fully conservative higher order finite difference schemes for incompressible flow. J.Comp.Phys.143, 90–124,1998.

[30] J. C. Adams, P. Swarztrauber, and R. Sweet. Efficient fortran subprograms for the solution of separable elliptic partial differential equations. http://www.cisl.ucar.edu/css/software/fishpack/, 1999.

[31] Zhong X. High-order finite-difference schemes for numerical simulation of hypersonic boundary-layer transition. J Comp. Phys. 144, 662–709, 1998.

[32] Leboucher L. Monotone scheme and boundary conditions for finite volume simulation of magnetohydrodynamic internal flows at high Hartmann number. J Comp. Phys. 150, 181–98, 1999.

[33] M.Pillar, E.Nobile and E.Hanaratty. DNS study of turbulent transport at low Prandtl numbers in a channel flow. J. Fluid mech.458, 419-441, 2002.

[34] Y.Yamamoto, T.Kunugi, T.Satake and S.Smolentsev. DNS and k–ε model simulation of MHD turbulent channel flows with heat transfer. Fusion Eng. 83, 1309-1312, Dec. 2008.

[35] P. Dey and O. Zikanov. Turbulent flow and transport of passive scalar in magnetohydrodynamic channel flows with different orientations of magnetic field. Int. J. Heat Fluid Flow. 36, 101–117, 2012.

[36] A. Alemany, R. Moreau, P. L. Sulem, and U. Frisch. Influence of an external magnetic-field on homogeneous MHD turbulence. J. Méc. 18, 277–313,1979.

[37] A. Vorobev, O. Zikanov, P. A. Davidson, B. Knaepen. Anisotropy of magnetohydrodynamic turbulence at low magnetic Reynolds number. Phys. Fluids.17, 125105, 2005.

[38] P. Burattini, O. Zikanov, B. Knaepen, J. Fluid Mech. 657, 502–538, 2010.

[39] P. A. Davidson. The role of angular momentum in the magnetic damping of turbulence. J. Fluid Mech. 336, 123–150, 1997.

[40] S. C. Kassinos, B. Knaepen, A. Wray. The structure of MHD turbulence subjected to mean shear and frame rotation. J. Turbulence 7, 2006.

[41] I. E. Sarris, S. C. Kassinos, D. Carati. Large-eddy simulations of the turbulent Hartmann flow close to the transitional regime. Phys. Fluids 19, 085109, 2007.

[42] D. S. Krasnov, E. Zienicke, O. Zikanov, T. Boeck, A. Thess, Numerical study of the instability of the Hartmann layer. J. Fluid Mech. 504 (2004) 183–211.

[43] P. Moresco, T. Alboussiere. Experimental study of the instability of the Hartmann layer J. Fluid Mech. 504, 167–181, 2004.

[44] S. C. Kassinos, W. C. Reynolds, M. M. Rogers. One-point turbulence structure tensors. J. Fluid Mech. 428, 213–248, 2001.

[45] Dritselis, C.D and Vlachos, N.S. Effect of magnetic field on near-wall coherent structures and heat transfer in magnetohydrodynamic turbulent channel flow of low Prandtl number fluids. Int. Journal of Heat and Mass Transfer 54, 3594-3604, 2011.

[46] Kassinos, S.C., Knaepen, B., Carati, D. The transport of a passive scalar in magnetohydrodynamic turbulence subjected to mean shear and frame rotation. Physics of Fluids 19, 015105, 2007.

[47] U. Schumann. Numerical simulation of the transition from three- to two-dimensional turbulence under a uniform magnetic field. J. Fluid Mech. 74, 31–58, 1976.

[48] Satake, Shin-ichi, Yoshida, N., Kunugi, T., Takase, K., Ose, Y., Kano,T. DNS of turbulent heat transfer under a uniform magnetic field at high Reynolds number. Fusion Engineering and Design 83, 1092-1096, 2008.

[49] Piller, M., Nobile, E., Hanratty,T.J. DNS study of turbulent transport at low Prandtl numbers in a channel flow. J. Fluid Mech. 458, 419-441, 2002.

[50] S. Satake, N. Yoshida, T. Kunugi, K. Takase, Y. Ose, T. Kano. DNS of turbulent heat transfer under a uniform magnetic field at high Reynolds number. Fusion Eng. Design 83, 1092–1096, 2008.

[51] A. V. Johansson, Petra M. Wikström. DNS and Modelling of Passive Scalar Transport in Turbulent Channel Flow with a Focus on Scalar Dissipation Rate Modelling. Flow, Turb. and Comb. 63, 223–245, 1999.

[52] Y. Na, D. V. Papavassiliou, T. J. Hanratty. Transport of a passive scalar in a turbulent channel flow. Int. J. Heat and Fluid Flow. 20, 187–195, 1999.

[53] J. Kim, P. Moin. Transport of passive scalars in a turbulent channel flow. Turb. Shear Flow 6, 85-96, 1989.

[54] P.K. Dey and O. Zikanov. Scalar transport and perturbation dynamics in intermittent magnetohydrodynamic flow. Phys. Fluids 24, 084104, 2012.

[55] J. Jimenez. Transition to turbulence in two-dimensional Poiseuille flow. J. Fluid Mech. 218, 265, 1990.

[56] O. Zikanov and A. Thess. Direct numerical simulation as a tool for understanding MHD liquid metal turbulence. Appl.Math. Model. 28, 1-13, 2004.

[57] A. Thess and O. Zikanov. Transition from two-dimensional to three-dimensional magnetohydrodynamic turbulence. J.Fluid Mech. 579, 383, 2007.

[58] G. Brethouwer, P. Schlatter, and A. V. Johansson. Turbulence, instabilities and passive scalars in rotating channel flow. J. Phys. Conf. Ser. 318, 032025, 2011.

[59] J. P. Johnston, R. M. Halleen, and D. K. Lezius. Effects of spanwise rotation on the structure of two-dimensional fully developed turbulent channel flow. J. Fluid Mech. 56, 533–557, 1972.

[60] R. Kristoffersen and H. I. Andersson. Direct simulations of low-Reynolds-number turbulent flow in a rotating channel. J. Fluid Mech. 256, 163–197, 1993.

[61] B. Eckhardt, T. M. Schneider, B. Hof, and J. Westerweel. Turbulence transition in pipe flow. Annu. Rev. Fluid Mech. 39, 447, 2007.

[62] M. Gad-el Hak and A. K. M. F. Hussein. Coherent structures in a turbulent boundary layers. Phys. Fluids 29, 2124, 1986.

[63] J. Schumacher and B. Eckhardt. Evolution of turbulent spots in a parallel shear flow. Phys. Rev. E. 63, 046307, 2001.

[64] I. J. Wygnanski and F. H. Champagne. On transition in a pipe. Part 1: The origin of puffs and slugs and the flow in a turbulent slug. J. Fluid Mech. 59, 281, 1973.

[65] Y. Duguet, P. Schlatter, D. Henningson, and B. Eckhardt. Self-sustained localized structures in a boundary-layer flow. Phys Rev Lett. 108, 044501, 2012.

[66] A. Prigent, G. Gregoire, H. Chate, O. Dauchot, and W. van Saarloos. Large-scale finite-wavelength modulation within turbulent shear flows. Phys. Rev. Lett. 89, 014501, 2002.

[67] D. Barkley and L. S. Tuckerman. Computational study of turbulent laminar patterns in Couette flow. Phys. Rev. Lett. 94, 014502, 2005.

[68] Y. Duguet, P. Schlatter, and D. Henningson. Formation of turbulent patterns near the onset of transition in plane Couette flow. J. Fluid Mech. 650, 119, 2010.

[69] S. Dong and X. Zheng. Direct numerical simulation of spiral turbulence. J. Fluid Mech. 668, 150, 2011.

[70] D. Krasnov, O. Zikanov, M. Rossi, and T. Boeck. Optimal linear growth in magnetohydrodynamic duct flow. J. Fluid Mech. 653, 273, 2010.

[71] M.-J. Ni, R. Munipalli, P. Huang, N. B. Morley, and M. A. Abdou. A current density conservative scheme for incompressible MHD flows at a low magnetic Reynolds number. Part I: On a rectangular collocated grid system. J. Comput. Phys. 227, 174, 2007.

[72] Y. Zhao, O. Zikanov, and D. Krasnov. Instability of magnetohydrodynamic flow in an annular channel at high Hartmann number. Phys. Fluids 23, 084103, 2011.
[73] Y. Zhao and O. Zikanov. Instabilities and turbulence in magnetohydrodynamic flow in a toroidal duct prior to transition in Hartmann layers. J. Fluid Mech. 692, 288, 2012.

[74] R. W. Metcalfe, S. A. Orszag, M. E. Brachet, S. Menon, and J. J. Riley. Secondary instability of a temporally growing mixing layer. J. Fluid Mech. 184, 207, 1987.

[75] M. M. Rogers and R. D. Moser. Spanwise scale selection in plane mixing layers. J. Fluid Mech. 247, 321–337, 1993.

[76] G. Brethouwer, Y. Duguet, and P. Schlatter. Turbulent-laminar coexistence in wall flows with Coriolis, buoyancy or Lorentz forces. J. Fluid Mech. 704, 137–172, 2012.

[77] A. Vorobev, O. Zikanov. Smagorinsky constant in LES modeling of anisotropic MHD turbulence. Theor. Comp. Fluid Dyn. 22, 317–325, 2007.

[78] S. Kenjeres, K.Hanjalic and D. Bal. A direct-numerical-simulation-based second-moment closure for turbulent magnetohydrodynamic flows. Phys. Fluids., 16, 2004.

[79] O.Widlund, S.Zahal and F.Bark. Development of a Reynold-stress closure modeling of homogenous MHD Turbulence. Phys.Fluids, 10, 1998.

[80] D.R.Wilson, T.J. Craft, H.Iacovides. Application of RANS turbulence closure models to flows subjected to electromagnetic and buoyancy forces. Int. J. Heat Fluid Flow, 49, 80–90, 2014.

[81] Y. Yamamoto, N. Osawa, T. Kunugi. A New RANS Model in Turbulent Channel Flow Imposed Wall-Normal Magnetic Field with Heat Transfer. Fusion. Sc.Tech., 72, 2017.

[82] Origin Lab: https://www.originlab.com/doc/Tutorials/Fitting-Piecewise-Linear